Role of Ion Redistribution at Selected Halide Perovskite Interfaces

Mina Jung

Role of Ion Redistribution at Selected Halide Perovskite Interfaces

Von der Fakultät Chemie der Universität Stuttgart
zur Erlangung der Würde eines Doktors der
Naturwissenschaften (Dr. rer. nat.)
genehmigte Abhandlung

Vorgelegt von

Mina Jung

aus Anseong, Republic of Korea

Hauptberichter:	Prof. Dr. Joachim Maier
Mitberichter:	Prof. Dr. Oliver Clemens
Prüfungsvorsitzender:	Prof. Dr. Rainer Niewa
Tag der mündlichen Prüfung:	26.07.2023

Max-Planck-Institut für Festkörperforschung

2023

Erklärung über die Eigenständigkeit der Dissertation

Ich versichere, dass ich die vorliegende Arbeit mit dem Titel *Role of Ion Redistribution at Selected Halide Perovskite Interfaces* selbständig verfasst und keine anderen als die angegebenen Quellen und Hilfsmittel benutzt habe, aus fremden Quellen entnommene Passagen und Gedanken sind als solche kenntlich gemacht.

Declaration of Authorship

I hereby certify that the dissertation entitled *Role of Ion Redistribution at Selected Halide Perovskite Interfaces* is entirely my own work except where otherwise indicated. Passages and ideas from other sources have been clearly indicated.

Stuttgart, 26.06.2023 Mina Jung

Abstract

The properties of interfaces between halide perovskites and contacting layers are key to the charge carrier dynamics in optoelectronic devices based on these materials. In particular, the space charge situation at such interfaces influences processes such as electronic charge carrier recombination, collection and injection, which determine the performance of perovskite solar cells. Space charges are commonly investigated only according to electronic equilibrium at junctions. Because halide perovskites are mixed ionic-electronic conductors, in which mobile point defects are the majority carriers, the ionic interactions at their interfaces are expected to have a critical impact on the determination of the space charge equilibrium. However, such influence has been largely overlooked since the rise of the perovskite solar cell field. This thesis discusses the experimental investigation of ionic effects on the space charge formation at selected interfaces of $CH_3NH_3PbI_3$ (MAPI) and examines how these effects can be modulated.

The first part of the results chapter focuses on strategies to control ionic effects at the interface between alumina and MAPI, through surface modification of the oxide surface by using organic molecules. Based on a combination of surface chemistry and electrochemical techniques, the results provide insights into the sign and magnitude of the space charge potential in MAPI when it comes into contact with alumina with or without surface modification. While embedding alumina nanoparticles within MAPI results in enhancement of electronic conductivity due to the presence of an ionically-generated space charge region, such effect is reduced by the organic molecules on the surface of the oxide. The observation is attributed to Pb^{2+}

cation adsorption on the surface of alumina, which occurs to a different extent when a molecular barrier is present. The results also emphasize that smaller molecules may be more effective at forming ion-blocking monolayers.

Next, the interfacial behavior of MAPI infiltrated in mesoporous-TiO_2 layers, commonly used as electron transporting material in solar cells, is investigated. The electrical response of the infiltrated perovskite points towards electrons dominating the conductivity in MAPI within the pores at low iodine partial pressures, as opposed to the p-type conduction recorded for the bulk of MAPI. This highlights the presence of a significant space charge in the pores of the oxide. The response indicates that nanoionics effects occur within at least part of such mesoscopic system. Because of the relatively unvaried electrical behavior of samples where surface modification is used, the space charge behavior in such system may have a dominant electronic component.

The investigation of the influence of space charges in solar cell devices with vertical configuration is presented. Conductivity measurement and the evaluation of power conversion efficiencies for solar cells with bare and surface-modified alumina:MAPI composites reveal that the presence of a distributed space charge within the active layer has a detrimental effect on the performance of devices. On the other hand, based on a mesoporous-TiO_2 thickness dependent experiment, the space charge region forming in MAPI within the pores of the oxide may be an essential factor to achieve high performance devices. This is possibly because of the reduction in the concentration of hole minority carriers in the region where electrons are extracted to the negative contact of the solar cell.

Lastly, the present study explores a generalized picture of the ionically-generated space charge at the interface between MAPI and other insulators, namely SiO_2 and MgO. The effect previously recorded for Al_2O_3 is demonstrated for the case of SiO_2, while negligible ionic adsorption is inferred for the MgO:MAPI composite. Importantly, the ionic interaction does not follow the trend predicted by the point of zero charge of these oxides, emphasizing the importance of studying specific interactions,

such as anion and cation adsorption effects involving the relevant perovskite precursors. The study is also extended to include an electronic hole-conducting oxide, NiO, using a composite device configuration. For this material, opposite results in space charge behavior are expected in MAPI based on either ionic or electronic equilibration arguments. Interestingly, no significant space charge on the MAPI side is extracted from the analysis of the composites electrical response. This is possibly accompanied by a significant space charge forming within the NiO phase, which could be consistent with a relatively low doping concentration in the oxide.

The thesis emphasizes that a comprehensive model describing the space charge situation at halide perovskite interfaces should consider not only the electronic equilibrium but also ionic effects. Overall, this study has the potential to assist the design of perovskite devices with improved interfacial properties and aid the interpretation of experimental data, accounting for the mixed conducting nature of halide perovskites.

Zusammenfassung

Die Eigenschaften der Grenzflächen zwischen Halogenid-Perowskiten und Kontaktschichten sind entscheidend für die Ladungsträgerdynamik in optoelektronischen Bauelementen, die auf diesen Materialien basieren. Insbesondere die Raumladungssituation an solchen Grenzflächen beeinflusst Prozesse wie die Rekombination, Sammlung und Injektion elektronischer Ladungsträger, die die Leistung von Perowskit-Solarzellen bestimmen. Raumladungen werden üblicherweise nur anhand des elektronischen Gleichgewichts an Übergängen untersucht. Da es sich bei Halogenidperowskiten um gemischte ionisch-elektronische Leiter handelt, bei denen mobile Punktdefekte die Hauptträger sind, wird erwartet, dass die ionischen Wechselwirkungen an ihren Grenzflächen einen entscheidenden Einfluss auf die Bestimmung des Raumladungsgleichgewichts haben. Dieser Einfluss wurde jedoch seit dem Aufkommen der Perowskit-Solarzellen weitgehend übersehen. Diese Arbeit diskutiert die experimentelle Untersuchung ionischer Effekte auf die Raumladungsbildung an ausgewählten Grenzflächen von $CH_3NH_3PbI_3$ (MAPI) und untersucht, wie diese Effekte moduliert werden können.

Der erste Teil des Ergebniskapitels konzentriert sich auf Strategien zur Kontrolle ionischer Effekte an der Grenzfläche zwischen Aluminiumoxid und MAPI durch Oberflächenmodifikation der Oxidoberfläche durch den Einsatz organischer Moleküle. Basierend auf einer Kombination aus Oberflächenchemie und elektrochemischen Techniken liefern die Ergebnisse Einblicke in das Vorzeichen und die Grösse des Raumladungspotentials in MAPI, wenn es mit Aluminiumoxid mit oder ohne Oberflächenmodifikation in Kontakt kommt. Während die Einbettung von Aluminiumoxid-

Nanopartikeln in MAPI aufgrund des Vorhandenseins einer ionisch erzeugten Raumladungszone zu einer Verbesserung der elektronischen Leitfähigkeit führt, wird dieser Effekt durch die organischen Moleküle auf der Oberfläche des Oxids verringert. Die Beobachtung wird auf die Kationenadsorption von Pb^{2+} auf der Oberfläche von Aluminiumoxid zurückgeführt, die in unterschiedlichem Ausmass auftritt, wenn eine molekulare Barriere vorhanden ist. Die Ergebnisse unterstreichen auch, dass kleinere Moleküle möglicherweise wirksamer bei der Bildung ionenblockierender Monoschichten sind.

Als nächstes wird das Grenzflächenverhalten von MAPI untersucht, das in mesoporöse TiO_2-Schichten infiltriert ist, die üblicherweise als Elektronentransportmaterial in Solarzellen verwendet werden. Die elektrische Reaktion des infiltrierten Perowskits deutet darauf hin, dass Elektronen die Leitfähigkeit in MAPI innerhalb der Poren bei niedrigen Jodpartialdrücken dominieren, im Gegensatz zur p-Typ-Leitung, die für den GroSSteil von MAPI aufgezeichnet wurde. Dies verdeutlicht das Vorhandensein einer erheblichen Raumladung in den Poren des Oxids. Die Antwort deutet darauf hin, dass nanoionische Effekte zumindest in einem Teil eines solchen mesoskopischen Systems auftreten. Aufgrund des relativ unveränderten elektrischen Verhaltens von Proben, bei denen Oberflächenmodifikationen verwendet werden, kann das Raumladungsverhalten in einem solchen System eine dominante elektronische Komponente haben.

Die Untersuchung des Einflusses von Raumladungen in Solarzellengeräten mit vertikaler Konfiguration wird vorgestellt. Leitfähigkeitsmessungen und die Bewertung der Leistungsumwandlungseffizienz von Solarzellen mit blanken und oberflächenmodifizierten Aluminiumoxid:MAPI-Verbundwerkstoffen zeigen, dass sich das Vorhandensein einer verteilten Raumladung innerhalb der aktiven Schicht nachteilig auf die Leistung von Geräten auswirkt. Basierend auf einem Experiment mit mesoporöse TiO_2, das von der Dicke abhängt, kann andererseits die Raumladungsregion, die sich in MAPI innerhalb der Poren des Oxids bildet, ein wesentlicher Faktor für die Erzielung leistungsstarker Geräte sein. Dies ist möglicherweise auf die Verringerung

der Konzentration von Lochminoritätsträgern in dem Bereich zurückzuführen, in dem Elektronen zum negativen Kontakt der Solarzelle extrahiert werden.

Abschliessend untersucht die vorliegende Studie ein allgemeines Bild der ionisch erzeugten Raumladung an der Grenzfläche zwischen MAPI und anderen Isolatoren, nämlich SiO_2 und MgO. Der zuvor für Al_2O_3 aufgezeichnete Effekt wird für den Fall von SiO_2 demonstriert, während für den MgO:MAPI-Verbundstoff eine vernachlässigbare Ionenadsorption abgeleitet wird. Wichtig ist, dass die ionische Wechselwirkung nicht dem Trend folgt, der durch den Ladungsnullpunkt dieser Oxide vorhergesagt wird, was die Bedeutung der Untersuchung spezifischer Wechselwirkungen, wie Anionen- und Kationenadsorptionseffekte, die an den relevanten Perowskit-Vorläufern beteiligt sind, unterstreicht. Die Studie wird auch auf ein elektronisches lochleitendes Oxid, NiO, unter Verwendung einer Verbundbauelementkonfiguration ausgeweitet. Für dieses Material werden in MAPI entgegengesetzte Ergebnisse im Raumladungsverhalten erwartet, basierend entweder auf ionischen oder elektronischen Gleichgewichtsargumenten. Interessanterweise wird aus der Analyse der elektrischen Reaktion des Verbundwerkstoffs keine signifikante Raumladung auf der MAPI-Seite extrahiert. Dies geht möglicherweise mit der Bildung einer erheblichen Raumladung innerhalb der NiO-Phase einher, was mit einer relativ geringen Dotierungskonzentration im Oxid vereinbar sein könnte.

Die Arbeit betont, dass ein umfassendes Modell, das die Raumladungssituation an Halogenid-Perowskit-Grenzflächen beschreibt, nicht nur das elektronische Gleichgewicht, sondern auch ionische Effekte berücksichtigen sollte. Insgesamt hat diese Studie das Potenzial, das Design von Perowskit-Geräten mit verbesserten Grenzflächeneigenschaften zu unterstützen und die Interpretation experimenteller Daten zu unterstützen, indem sie die gemischte Leitfähigkeit von Halogenid-Perowskiten erklärt.

Contents

1 Introduction

In recent years, the field of halide perovskite solar cells (PSCs) has made remarkable advances, demonstrating device performance comparable with traditional photovoltaic technologies. Such advances have been possible due to the exceptional optoelectronic properties of hybrid organic inorganic perovskites (HOIPs), such as high absorption coefficients [1–3], long carrier lifetimes and high charge carrier mobility [4–9]. Despite the potential of PSCs as efficient solar cells, their poor long-term stability and reliability remain significant challenges [10–12]. During operation, PSCs often exhibit hysteresis in their electrical response [13, 14], phase segregation [15, 16], and degradation [17, 18]. It is now established that some, if not all, of these challenges can be attributed to the complex behavior of mobile ions in the bulk of HOIPs, as well as at the interfaces with the contact materials within the device. Beyond issues related to unstable power output, the impact of mobile ions in the perovskite layer affects charge recombination through ion-induced electric field screening at the interfaces, also modulating the electrical response of devices at a fundamental level [19–21]. It is evident that, in order to improve the performance and reliability of PSCs, it is crucial to gain a better understanding of the role of mobile ions in HOIPs and their interfaces.

This thesis aims to address the complex behavior of mobile ions at selected interfaces in HOIPs. Before presenting the main findings (Chapter 3), this introduction chapter provides a comprehensive overview of HOIPs, with special focus on their mixed ionic-electronic conductivity. The topic of ion redistribution and the role of ion transport in space charges forming at interfaces are discussed in detail and with

reference to previous studies on this subject within the PSC and other fields. Lastly, the use of HOIPs in solar cell structures, the investigation of interfaces in PSCs is presented, followed by an outline of the other chapters in this thesis.

1.1 Halide perovskites

1.1.1 Crystal structure

The crystal structure of HOIPs is denoted as ABX_3, where A is a cation such as methylammonium (MA), formamidinium (FA), or cesium, B is a metal cation, typically lead or tin, and X is a halogen anion such as chloride, bromide, or iodide (Figure 1.1). The versatility of the perovskite crystal allows for the incorporation of different elements into the framework. This flexibility has led to the development of a wide range of compounds with unique optical and electronic properties [22–26]. Among the various compositions of HOIPs, methylammonium lead triiodide (MAPI) was first reported in 1978 [27] and was also the first material investigated within solar cell architectures, initially as part of dye-sensitized solar cell structures and later as the active layer of PSCs [3, 28]. While refinement of optimal hybrid perovskite compositions to maximize solar cell efficiencies is ongoing, with mixed-cation-mixed-halide compounds showing promising performance, MAPI remains one of the most extensively researched materials in this photovoltaic field.

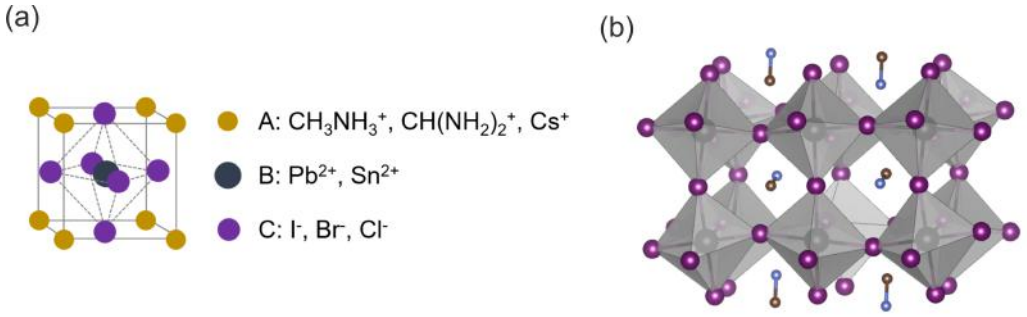

Figure 1.1: Structure of (a) halide perovskites with general formula of ABX_3 and (b) MAPI in tetragonal phase.

1.1.2 Mixed conducting properties and defect chemistry of halide perovskites

Mixed ionic-electronic conduction is an important feature of halide perovskites, having significant implications for the behavior, performance and lifetime of PSCs [29–31]. Mixed conductivity in halide perovskites refers to the transport of electronic charge carriers (conduction band electrons (e') and valence band holes ($h^{\bullet}$)) and of ionic defects, such as ion vacancies and interstitials [32–34].

The electronic response of halide perovskites, *i.e.* due to free electrons and holes, can be controlled by exposure to light with above bandgap photon energy, as it is the case for all semiconductors (see Section 1.3.1). These carriers can move through the perovskite lattice and contribute to the (photo)conductivity of the material. The presence of mobile ions contributes to the total conductivity of the perovskite. Besides carrying electrical current, mobile ions can also change the local electric potential landscape, affecting various electronic processes such as injection, recombination *etc.*

In 1983, Mizusaki *et al.* reported on the ionic conduction of halide perovskites using $CsPbCl_3$ and $CsPbBr_3$ pellets [35]. They obtained a conductivity of approximately 10^{-3} S/cm for both samples at 673 K, which they attributed to ionic conduction. This conclusion was based on an electrochemical experiment performed on a pellet sandwiched between Pb and AgX|Ag pellets (Figure 1.2 (a)). The researchers confirmed the mobility of the halide ions by observing an increase in weight in the Pb|$CsPbX_3$ and a decrease in weight in the AgX|Ag blocks corresponding to an equivalent amount of ions transfered according to the applied current.

Yang *et al.* measured the galvanostatic direct current (DC) polarization curve for a C|MAPI|C pellet at room temperature in Ar [32]. When the current was switched on, a voltage step followed by a gradual increase in voltage over long time scales (10^4 seconds) was observed (Figure 1.2 (b)). By assuming ion blocking properties for the carbon contacts, this result was interpreted in terms of stoichiometric polarization

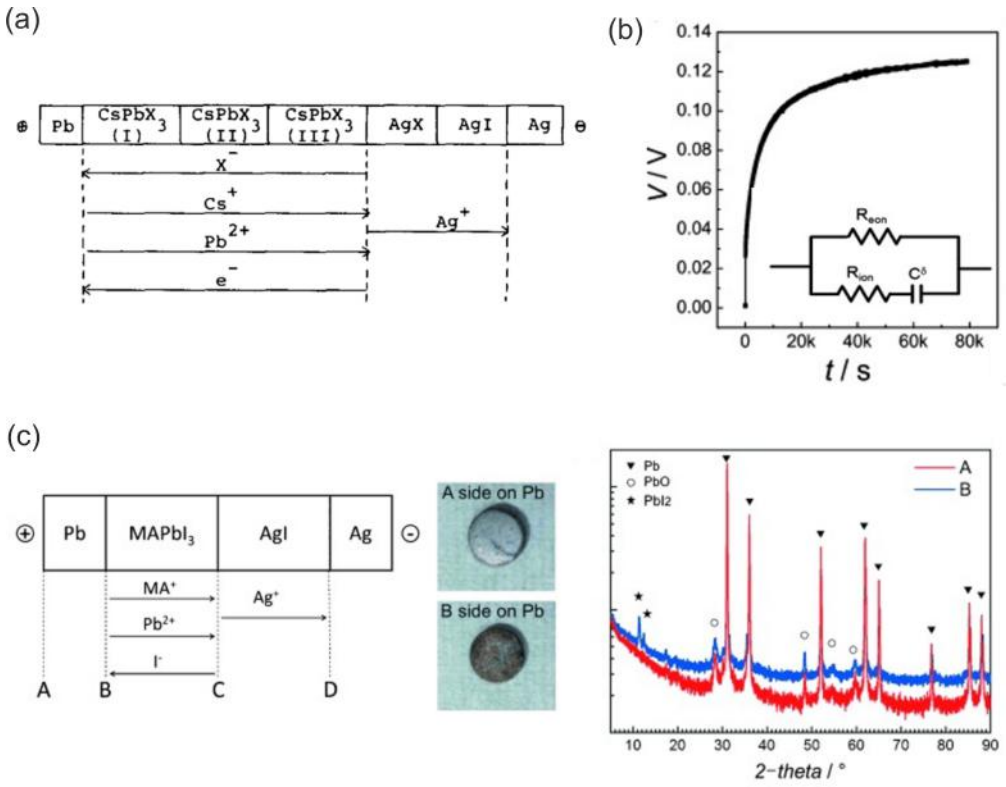

Figure 1.2: (a) The measurement cell structure used by Mizusaki *et al.* (reproduced with permission from reference [35]). (b) A galvanostatic DC polarization curve of MAPI pellet between carbon electrode, which showed a gradual increase in voltage due to slow ion transport. (c) Left: the cell structure, middle: images to show surface morphology changes of the Pb pellet, right: XRD pattern confirming iodide ion transport in this cell (reproduced with permission from reference [32]).

occurring within the MAPI layer, whereby ion redistribution leads to a composition gradient build-up within the cell, while at long times, only electronic current is flowing. The majority mobile ion was identified to be iodide, based on experiments carried out on a similar cell structure to that used by Mizusaki *et al.*: using X-ray diffraction (XRD) spectroscopy, they observed the formation of PbI_2 on the surface of Pb, indicating transport of iodide ions (Figure 1.2 (c)).

While early studies suggested that iodide vacancies ($V_I^\bullet$) are the key mobile ionic defects in halide perovskites experimentally [36, 37] and theoretically [38–40], an important proof of this hypothesis came with the work by Senocrate *et al.* [33] who showed that iodide vacancies are majority mobile ionic charge carriers in MAPI

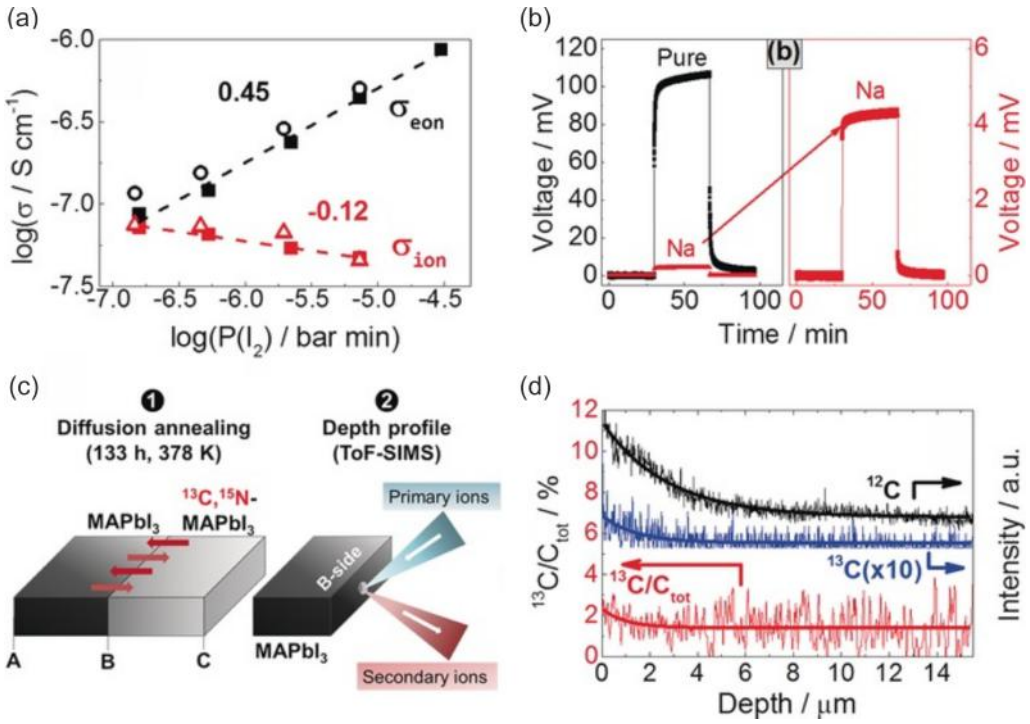

Figure 1.3: (a) Ionic (red) and electronic (black) conductivities of a MAPI pellet in different iodine partial pressure at 373 K. (b) Comparison of galvanostatic polarization curves betweend pure MAPI and Na doped MAPI at 378 K. (c) Scheme of the tracer diffusion experiment. (d) Time-of-flight secondary ion mass spectroscopy depth profile of a pure MAPI pellet after diffusion annealing in contact with a pellet (reproduced with permission from reference [33]).

based on doping experiments. Na ion leads to substitutional doping of Pb cation and a significant enhancement of both ionic and electronic conductivity, consistent with an increase in the concentration of iodide vacancies and electron holes (Figure 1.3 (b)). For the lead and MA defects no significant long range diffusion was detected at room temperature, based on tracer diffusion (Figure 1.3 (c-d)) and nuclear magnetic resonance experiments.

The ionic and electronic charge carrier concentration in mixed ionic-electronic conductor (MIEC) depends on temperature, and on the partial pressure of every exchangeable component. Its charge carrier chemistry is also crucially influenced by impurities or dopants. The impact of these parameters is critical for a detailed understanding of the materials electrochemical behavior, and reveals suitable adjusting

screws to tune the electrical transport properties. In Figure 1.3 (a), the electronic and ionic conductivities measured for a MAPI pellet between carbon contacts are shown as functions of the iodine partial pressure ($p(\mathrm{I}_2)$) in the measuring cell.

To understand how such trends can be useful in the determination of the material transport properties, defect diagrams (Kröger-Vink diagrams), where the expected concentration of each defect with respect to a component partial pressure, are commonly used. For MAPI, one can consider Schottky disorder to be dominant, based on calculation of the formation energy associated with the Schottky reaction [41]

$$I_I^{\times} + MA_{MA}^{\times} \rightleftarrows V_I^{\bullet} + V_{MA}^{'} + MAI \tag{1.1}$$

The electronic disorder reaction at equilibrium can be written as:

$$h^{\bullet} + e^{'} \rightleftarrows nil \tag{1.2}$$

Finally, one can write the iodine exchange reaction at the solid-gas interface based on

$$\frac{1}{2}I_2 + V_I^{\bullet} \rightleftarrows I_I^{\times} + h^{\bullet} \tag{1.3}$$

By considering the mass-action laws deriving from these reactions, along with the condition of electroneutrality, one obtains a solution for the charge carrier equilibrium, where the iodine partial pressure is the only free parameter. This is displayed in Figure 1.4.

At low $p(\mathrm{I}_2)$, MAPI exhibits n-type behavior, where electrons (Pb^{2+} excess electrons in Pb orbitals) are compensated by iodide vacancies. At high $p(\mathrm{I}_2)$, MAPI is p-type, with holes (formation of I^0 by holes predominantly in I orbitals) being compensated by MA vacancies. The data in Figure 1.3 (a) show that MAPI, prepared under common synthesis procedures, is intrinsic. Indeed the slope of the electronic conductivity vs. $p(\mathrm{I}_2)$ is approximately 0.5, reflecting the dependence of the hole concentration on such parameter in Figure 1.4.

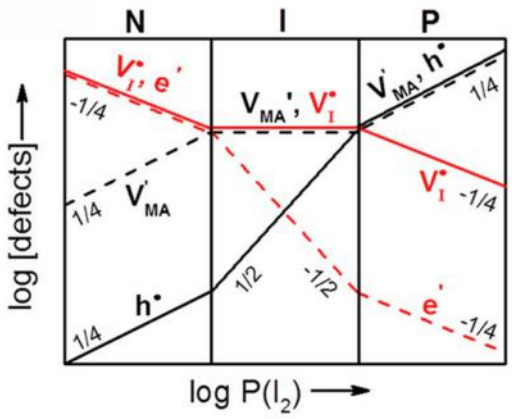

Figure 1.4: Kröger-Vink diagram showing the electronic and the ionic defect concentrations in MAPI assuming Schottky ionic disorder (reused with permission from reference [29]).

The effect of other defects, such as MA-interstitials and Pb-defects, can be neglected as long as their concentrations are well below the concentration range of the majority carriers, and their mobility is low.

Additional complexity to the defect chemistry of MAPI needs to be accounted for in presence of dopants. These can be immobile acceptor or donor dopants. Furthermore, oxygen has been demonstrated to act as dopant in MAPI according to:

$$\frac{1}{2}O_2 + V_I^{\bullet} \rightleftarrows O_I' + 2h^{\bullet} \tag{1.4}$$

$$K_O = \frac{[h^{\bullet}][O_I'] P_{I_2}^{1/2}}{P_{O_2}^{1/2}} \tag{1.5}$$

In Figure 1.5, the resulting defect diagrams (Kröger-Vink diagrams) for MAPI including the contribution of dopants are illustrated. The diagrams show the concentrations of iodide vacancies, MA vacancies, excess electrons, and electron holes as a function of $p(\mathrm{I_2})$, $p(\mathrm{O_2})$ and dopant contents. The diagrams predict that the hole concentration is expected to increase with $p(\mathrm{I_2})$, while the opposite behavior concern the electron concentration. The iodide vacancy concentration is predicted

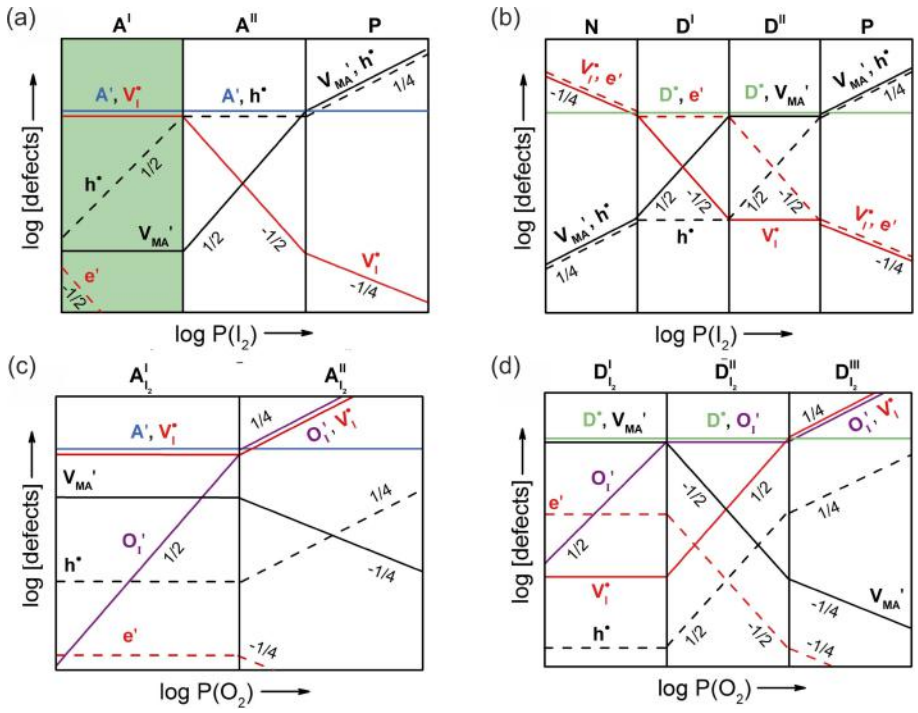

Figure 1.5: Kröger-Vink diagrams calculated as a function of I_2 and O_2 partial pressure for (a), (c) acceptor- and (b), (d) donor-doped MAPI. The slopes of each defect concentrations are indicated in the Figures (reused with permission from reference [42]).

to decrease with $p(I_2)$ but increase with $p(O_2)$ (or acceptor dopant concentration).

In summary, mixed ionic electronic conductivity is an important property of halide perovskites that arises due to the presence of mobile defects in the material. Given the many questions related to how ion transport is connected, beneficially or detrimentally, with the behavior of PSCs, it is crucial to understand and control the mechanisms by which ion transport affects device response.

1.2 Interfacial space charges

When studying devices that use MIECs, it is important to refer to models that are able to describe both electronic and ionic charge carriers. In the previous section, examples of Kröger-Vink diagrams have been presented for the study of the bulk properties of MAPI. When focusing on the bulk but also on the interfacial behavior

of MIECs, other representations become convenient. For example, energy diagrams are a useful tool for displaying charge carrier properties and dynamics under various conditions and as a function of position. While electronic energy diagrams are commonly used to describe semiconductors, when studying PSCs it is essential to represent both ionic and electronic charge carriers. In this section, these energy diagrams are used to describe the charge carrier equilibrium at interfaces, and the formation of space charge zones.

1.2.1 Energy diagrams of mixed conductors

Common energy diagrams are used to represent the energy levels in a semiconductor, depicting the valence (VB) and conduction band (CB) edges (Figure 1.6), often indicated with E_V and E_C. The bandgap (E_g), is the energy difference between the E_V and E_C. It is a crucial parameter for understanding the electrical and optical properties of the material, because E_g represents the standard free energy associated with the electronic disorder reaction (ΔG_f°) of equation 1.2. Here, the transfer of a valence electron into the CB can be considered as the formation of one extra particle, the conduction band electron, and of one vacancy, the electron hole.

Based on a defect chemical description of semiconductors, the band edges can be defined as standard potentials of electronic defects (electron and hole) ($\mu_{e'}^\circ$ and $-\mu_{h^\bullet}^\circ$). The occupation of the two bands is determined based on the position of the

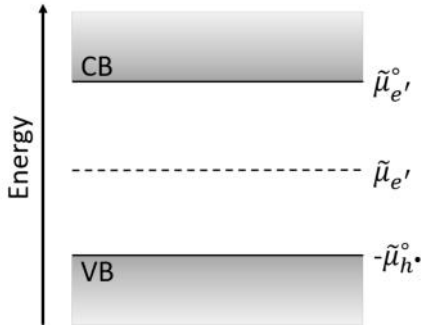

Figure 1.6: Energy diagram indicating the valence and conduction band and the electrochemical potential of the electrons.

Fermi level (E_F), or the electrochemical potential of the electrons. At equilibrium, this is equal to (minus) the electrochemical potential of the holes and is defined as:

$$\widetilde{\mu}_{e'} = \mu^{\circ}_{e'} + RT\ln[e'] - F\phi = \widetilde{\mu}^{\circ}_{e'} + RT\ln[e'] \tag{1.6}$$

$$\widetilde{\mu}_{h^{\bullet}} = \mu^{\circ}_{h^{\bullet}} + RT\ln[h^{\bullet}] - F\phi = \widetilde{\mu}^{\circ}_{h^{\bullet}} + RT\ln[h^{\bullet}] \tag{1.7}$$

A similar definition can be applied to the defects associated with a specific ion, *e.g.* $V_I^{\bullet}$ and iodide interstitials (I_i'). This results in the definition of a generalized energy diagram, where it is also possible to identify the chemical potential of the relevant component (*e.g.* X = iodine in Figure 1.7) [34, 43].

At equilibrium the electrochemical potential of all mobile charge carriers is constant. This condition leads to the calculation of defect concentration profiles and of the electrical potential profile through equation 1.6 and 1.7. The equilibration of both electronic and ionic defects can contribute to such solution, as it is discussed in the next section.

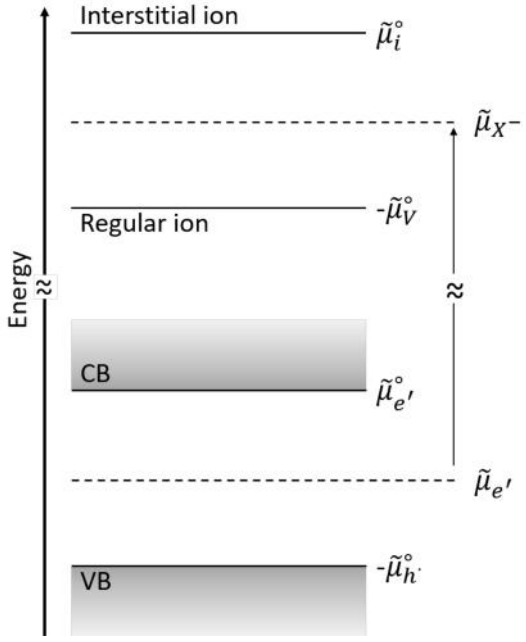

Figure 1.7: The ionic for $V_I^{\bullet}$ and I_i' and the electronic energy level including the chemical potential of the relevant component.

1.2.2 Space charge generation at interfaces of semiconductors

In the conventional view of semiconductor physics, the redistribution of electronic charge carriers is the only factor taken into consideration when evaluating equilibration at interfaces. This means that, when two materials with different E_Fs come into contact, the electronic charge carriers will be transferred until equilibrium is reached (Figure 1.8). A typical example involves the junction between a donor doped and an acceptor doped layer of the same material. Because of their doping, the two phases have different work function and E_F position. Under thermodynamic equilibrium, the resulting p-n junction has a constant E_F and an energy band diagram that shows bending of the E_C and E_V as a function of position. The reason for such bending is the fact that the transfer of free carriers has left some charged dopants behind. Such excess charge gives rise to a change in the electric potential according to Poissons equation

$$\Delta\phi = -\frac{\rho}{\varepsilon} \tag{1.8}$$

where ρ is the net charge density and ε is the dielectric constant of the material. The regions where $\rho = 0$ are referred to as quasi-neutral regions. On the other hand, the regions where the net charge in the system is not zero, and where significant changes in electric potential as function of position, are commonly referred to as space charge regions. In a p-n junction, the barrier in the electric potential between the p and n regions is known as the built-in potential barrier (V_{bi}) (Figure 1.9). This barrier maintains equilibrium between majority and minority carrier electrons and holes between the two layers, by introducing a drift term that counter-balance the diffusion of the electronic charges.

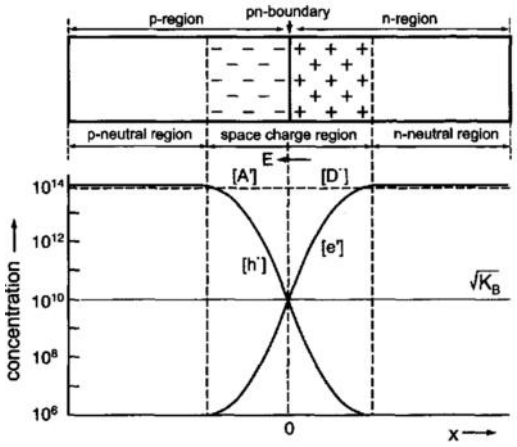

Figure 1.8: Charge carrier distribution in thermal equilibrium at a p-n junction between p-type and n-type materials (reproduced with permission from reference [44]).

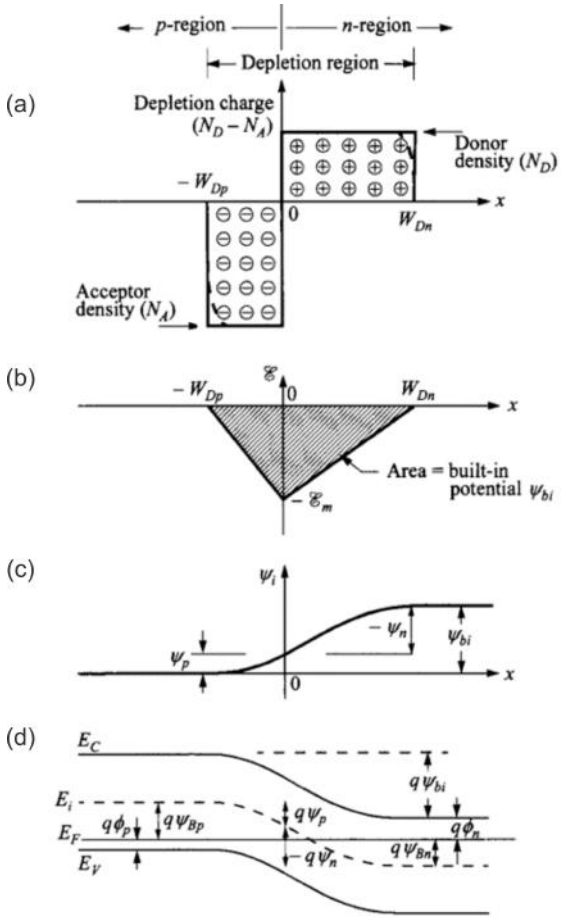

Figure 1.9: P-n junction in thermal equilibrium. (a) charge distribution, (b) electric-field distribution, (c) potential distribution and (d) energy band diagram. Here, ψ_{bi} (or V_{bi}) is the built-in potential (reproduced with permission from reference [45]).

1.2.3 Space charge generation at interfaces of ionic or mixed conductors

In systems involving MIECs, beside the electronic effects described above, the redistribution of mobile ions and their equilibration must also be considered. The field of studying ionic charge carriers and their behavior at interfaces, with special reference to confined systems, is known as nanoionics [44]. Achieving complete equilibrium at interfaces requires that the electrochemical potentials of both ions and electrons are spatially invariant.

The CaF_2/BaF_2 is a well known model system to explain this ion redistribution at heterojunctions (Figure 1.10) [46, 47]. Both CaF_2 and BaF_2 are ionic conductors and have anti-Frenkel disorder (involving fluoride vacancies and interstitials,$V_F^{\bullet}$ and F_i'). Conductivity measurements performed on devices containing such heterojunction in the direction parallel or perpendicular to the interface enabled the identification of accumulation of ionic charge carrier (here, F_i') on the CaF_2 side at the interface between CaF_2/BaF_2. To compensate this, $V_F^{\bullet}$ are accumulated in BaF_2 side at the interface. Both these accumulation layers vary the material conductivity by orders

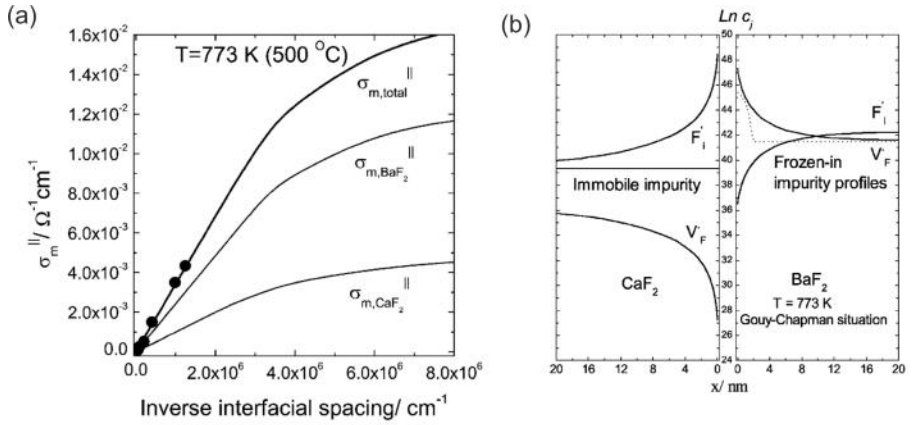

Figure 1.10: (a) The parallel conductivity and fitting results as a function of inverse interfacial spacing in multiple hetero junction of CaF_2/BaF_2 and (b) the derived defect concentration profiles for temperatures at 773 K (reproduced with permission from reference [46]).

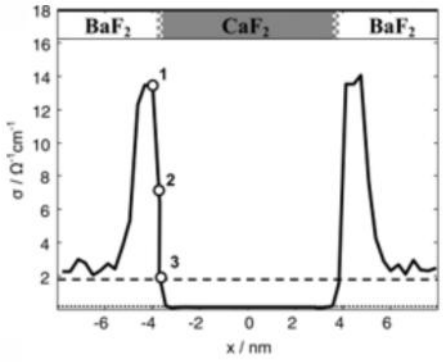

Figure 1.11: Calculated profile of the ion conductivity for the heterojunction interface between CaF_2/BaF_2 at 800 K. The dashed line and the dotted line indicate the conductivity in bulk CaF_2 and BaF_2 as obtained from experiments, respectively (reused with permission from reference [47]).

of magnitude, depending on the fraction of material volume exhibiting interfacial or bulk behavior. The activation energy (E_a) of transport in this system confirms this interpretation. Such result is also consistent with molecular dynamics simulations, which clearly indicate a tendency for mobile ionic charge carriers to accumulate at the interface between these two materials (Figure 1.11) [47]. This system clearly demonstrates that charge redistribution and space charge formation can occur as a result of ionic charge carrier equilibration.

Figure 1.12 shows a variety of other ion interactions between ionic conductors or MIECs with the insulators Al_2O_3 and SiO_2 [48]. When an ion conductor is in contact with an insulator, ion adsorption can occur. Such adsorption of ions at the interface results in formation and redistribution of defects in the bulk. This ionic adsorption on the surface of the oxide induces changes in the charge carrier concentration at the interface, impacting the space charge equilibrium.

Figure 1.13 (a) shows the energy level representation of an example where ionic equilibration between two ionic conductors leads to space charge formation. The two materials′s energy levels represent Frenkel and anti-Frenkel defects. The energy levels in the space charge region bend to achieve equilibrium. Figure 1.13 (b) refers to the changes in the electrical, chemical, and electrochemical potentials of different components (such as ions, electrons, and defects) at the ideal interface.

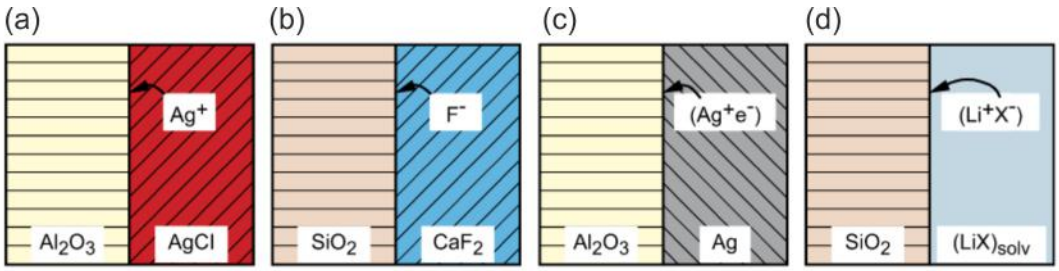

Figure 1.12: Example of ionic adsorption at the contact of the ion conductor to an insulator (reproduced with permission from reference [48]).

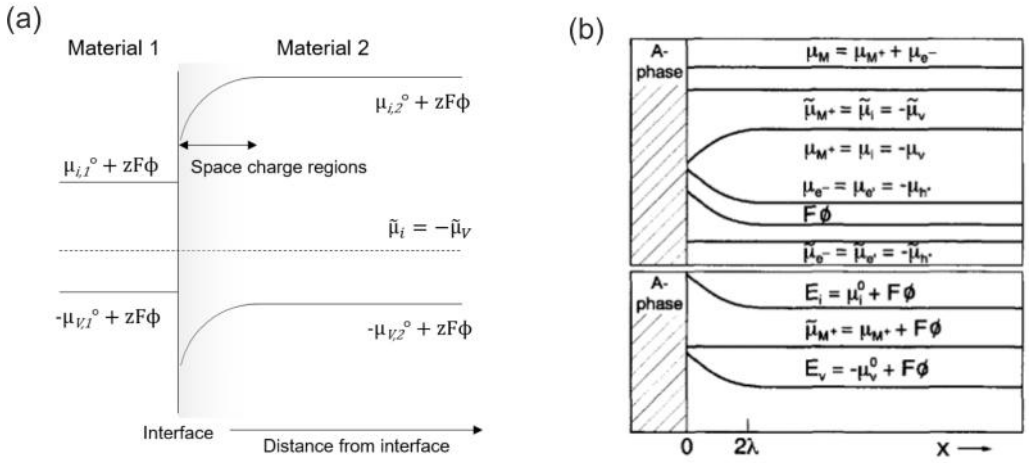

Figure 1.13: (a) Equilibrium in the energy level diagram for Frenkel defects or anti frenkel defects. (b) The variation of the electrical, chemical and electrochemical potentials of ions and electron defects [44]

Depending on the defect that is highest in concentration in proximity of the interface, different solutions to the space charge situation can be obtained. There are two basic cases describing space charge formation: the Gouy-Chapman and Mott-Schottky models (Figure 1.14). Originally, the Gouy-Chapman model was used to explain how a charged surface interacts with ions in a solution, a situation relevant to electrode/electrolyte interfaces [49, 50]. This model assumes that diluted ions are randomly distributed and mobile in the solution, and that the electric field at the surface of the electrode causes ions to accumulate and form a double layer at the interface. The Gouy-Chapman model helps to determine how this diffuse layer

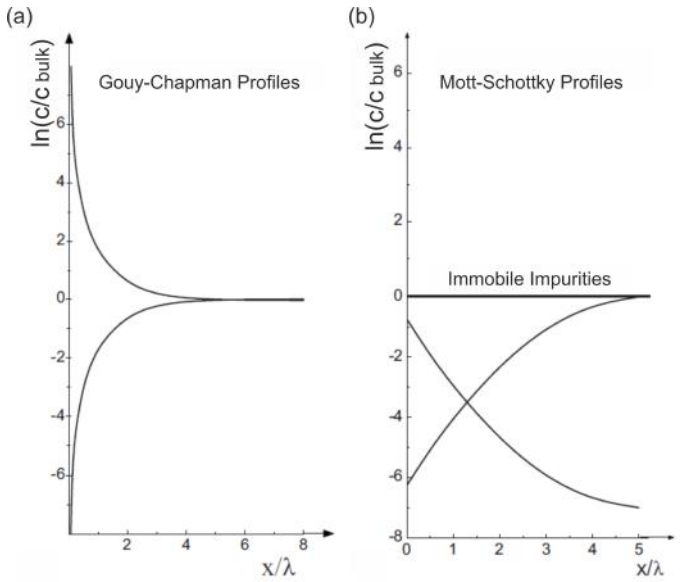

Figure 1.14: Defect profiles of (a) Gouy-Chapman and (b) Mott-Schottky model (reproduced with permission from reference [51]).

of ions is formed as function of distance from the electrode based on the size and charge of the ions.

A similar model applies to the solid state case [52, 53]. Whenever the majority charged mobile defect accumulates at an interface as a result of equilibration with a second phase, the solution describing the electric potential, and therefore the concentration profile of all charged defects, follows the Gouy-Chapman solution. The region where significant changes in concentrations occur with respect to the bulk is confined to about the width quantified by the Debye length (λ).

In other cases, the majority carriers in a material may be compensated by immobile impurities in the bulk. Under such conditions, the mobile majority carrier can still dominate the space charge situation if its concentration increases while approaching the interface. However, in situations where such defect concentration decreases in the interfacial region (depletion), the immobile defect becomes the majority charged species near the interfaces. As a result, the space charge situation follows a different solution, commonly referred to as Mott-Schottky situation [49]. In this case, the impurity profile is assumed to be uniform through the material. As a result, the

width of the space charge region (λ^*) is commonly larger than for the Gouy-Chapman case.

Both Gouy-Chapman and Mott-Schottky models are important in electrochemistry and are used to describe a wide range of interfacial phenomena. Based on these models, it is possible to extract information on the electrical potential profile, whenever knowledge of the defect concentration profiles is available (for example from conductivity measurements). The overall change in potential at an interface is called space charge potential and it is a main parameter in the description of junctions in electrochemical systems.

1.3 Interfaces in perovskite solar cells

1.3.1 Perovskite solar cells

The basic working principle of PSCs is as follows: when sunlight is incident on the perovskite material, photons are absorbed, generating excess electrons and holes. These electronic carriers are then transported to opposite electrodes, where they generate a flow of electrical current into the external circuit (Figure 1.15).

Since MAPI was first used as a sensitizer in solar cells with a power conversion efficiency (PCE) of 3.8% [28], the efficiency of PSCs has increased rapidly in recent years, and now stands at over 25% [54]. Researchers are exploring various approaches

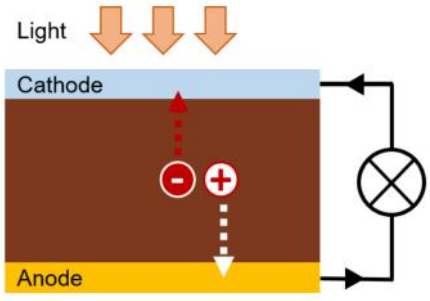

Figure 1.15: Simplified diagram illustrating the working principle of a solar cell. The arrows in the external circuit indicate the flow of electrons.

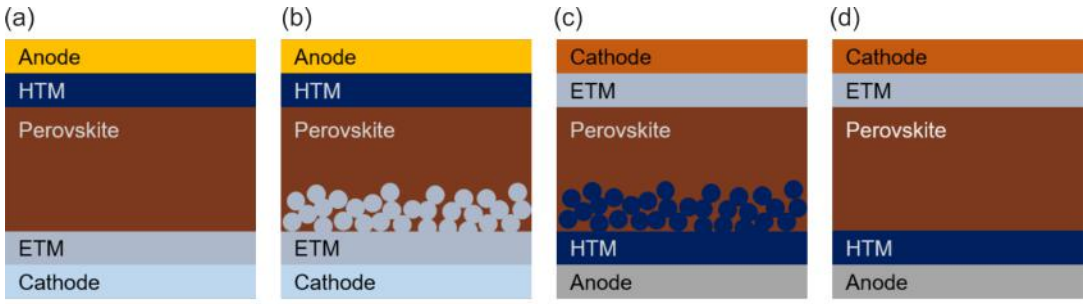

Figure 1.16: PSCs structure of (a) n-i-p (b) n-i-p planar (c) p-i-n and (d) p-i-n planar devices. ETM and HTM denote electron and hole transporting materials.

to improve the efficiency further, such as optimizing the composition and structure of the materials used [22–26], as well as the device architecture [55, 56]. Also, researchers have reported efficiency improvement using two-dimensional perovskites [57–59] and optimizing the contacting charge carrier transport layers [57–59]. Another important direction is the exploration of approaches to improve the stability, such as encapsulation and doping of the active layer [60–62].

The perovskite active layer in a device is in contact with different materials, as shown in Figure 1.16. Such unavoidable interfaces are crucial for efficient charge extraction, in that effective collection of charge carriers generated in the perovskite layer by the electrodes is necessary to produce an external current. However, recombination of charge carriers can be pronounced at the interfaces between the perovskite layer and other layers due to interfacial defects. These can hinder charge extraction and lower the overall efficiency of the device. Such recombination processes follow rate laws with specific dependences on electronic charge carrier concentrations. Control on the carrier concentration profiles at interfaces is therefore an important factor to minimize losses.

As presented in the previous section, the space charge situation in mixed conducting systems is largely set by the majority carriers. For hybrid perovskites, mobile ionic charge carriers are present in large concentrations and their equilibration is expected to significantly impact the space charge formation at interfaces, influencing the charge dynamics within the device. Recent studies have started to consider such

equilibration within the perovskite layer as an important factor to the device function [63]. However, interactions with the contact layers of mobile ionic defects have been largely ignored in the literature, and a precise picture of such ionic interaction is lacking.

1.3.2 Previous studies: ion redistribution in solar cells

Since Snaith *et al.* published their findings on anomalous hysteresis behaviour (the difference in the current-voltage (J-V) curve between the forward and reverse bias directions) in $MAPbI_{3-x}Cl_x$ perovskite solar cells [13], many research groups have been investigating the origin of this phenomenon in halide perovskite solar cell devices [64–67]. It has been established that hysteresis is caused by ion migration in the perovskite layer, which changes the electric potential at interfaces of perovskites [68–72]. Such changes occur spatially and temporally, leading to variation in charge collection and recombination, giving rise to a measured current that depends on the devices history, hence leading to hysteresis effects [73–76].

Researchers are exploring various strategies to control and mitigate ionic redistribution within perovskite solar cells. For example, one approach involves modifying the composition or structure of the perovskite material to reduce the mobility of charged ions. Another strategy involves the use of passivation layers or interface engineering to reduce the impact of ionic defects. To mitigate the effects of ion migration and hysteresis, various strategies have been proposed, such as introducing additives in the perovskite solar cells. Kim *et al.*, found that small amount of PbI_2 additive accelerated ion migration at the grain boundary in FAMA mixed halide perovskites and reduces charge carrier recombination [77]. Abdi-Jalebi *et al.*, used potassium iodide to passivate grain boundary for reducing ion migration [78]. Son *et al.*, also used KI. They suggest K ions to prevent ion migration in FA based halide perovskite [79].

It is worth mentioning that other hypotheses have been proposed for explaining the anomalous behavior in halide perovskite solar cells. One possible explanation is

related to ferroelectric properties of the perovskite material [80, 81]. In ferroelectric materials, the polarization direction can be switched by applying an external electric field, and this switching can be accompanied by hysteresis behavior. However, even though the dielectric constatnt is rather normal ($\varepsilon \cong 30$) [32], this hypothesis is still under debate, and more research is needed to fully understand the role of ferroelectricity in the hysteresis behavior. On the other hand, ionic effects are widely established as a major contributor to the optoelectronic response of these devices. Below, recent understanding of how their influence goes beyond bulk behavior is presented.

1.3.3 Ionically-generated space charges at halide perovskite interfaces: first evidence

Kim *et al.* [82] investigated the equilibrium space charge effects due to ionic interactions between MAPI and the oxides Al_2O_3 and TiO_2. They measured electronic (σ_{eon}) and ionic conductivities (σ_{ion}) in composite films where alumina or titania nanoparticles are embedded in MAPI (oxide:MAPI) with different concentrations of the oxides. By performing DC galvanostatic polarization measurements at different $p(I_2)$ they were able to control the charge carrier concentration in MAPI and analyse the trends as a function of "the fraction of interfaces present in the film" (Figure 1.17). At the low $p(I_2)$, σ_{eon} is increased with increasing oxide concentration in the composite film, while σ_{ion} is decreased. When the conductivities are measured under high $p(I_2)$, σ_{ion} shows similar trends compared to the low $p(I_2)$ case, however σ_{eon} exhibited a decrease with increasing oxide concentration. This results can be explained by considering the space charge forming at the interface between MAPI and the oxides. A depletion of $V_I^{\bullet}$s at the interface was inferred based on the decreased σ_{ion} with increasing oxide content. At low $p(I_2)$, hole concentration close to the interface is largely decreased similar to $V_I^{\bullet}$s, while the electron concentration is increased due to its negative charge. Such increase can induce an inversion space

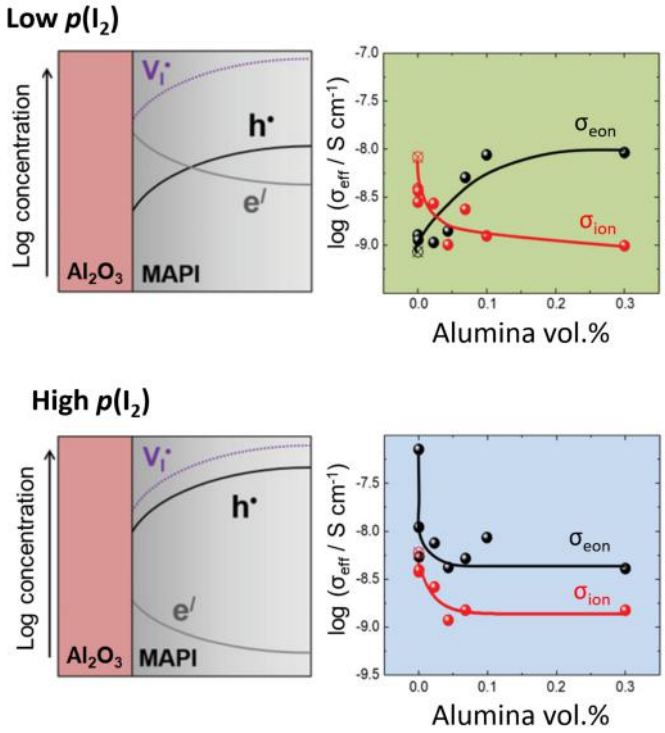

Figure 1.17: (Left) The charge carrier concentration changes at the interface between alumina and MAPI. (Right) The conductivity measurement in alumina:MAPI composite films with different alumina particle concentrations for different iodine partial pressures (reproduced with permission from reference [82]).

charge (electron charge carrier concentration at the interface is higher than the bulk concentration of holes in MAPI) resulting in a high overall σ_{eon} in the system. When $p(I_2)$ is increased, the increase in hole concentration and decrease in electron concentration could explain the disappearance of the inversion trend, giving rise to a depletion trend instead. Because these results were observed for the case of alumina, which is an insulator, they clearly pointed to an ionic interaction being responsible for the inferred space charge equilibrium.

Zeta potential, X-ray photoelectron spectroscopy (XPS) and inductively coupled plasma optical emission spectroscopy (ICP-OES) measurements were performed to identify which ionic interaction occurs at the surface of Al_2O_3 and TiO_2 in MAPI precursor solutions. The results pointed towards Pb^{2+} cation adsorption on the surface of alumina and titania. The adsorption of Pb^{2+} ions on the surface of Al_2O_3

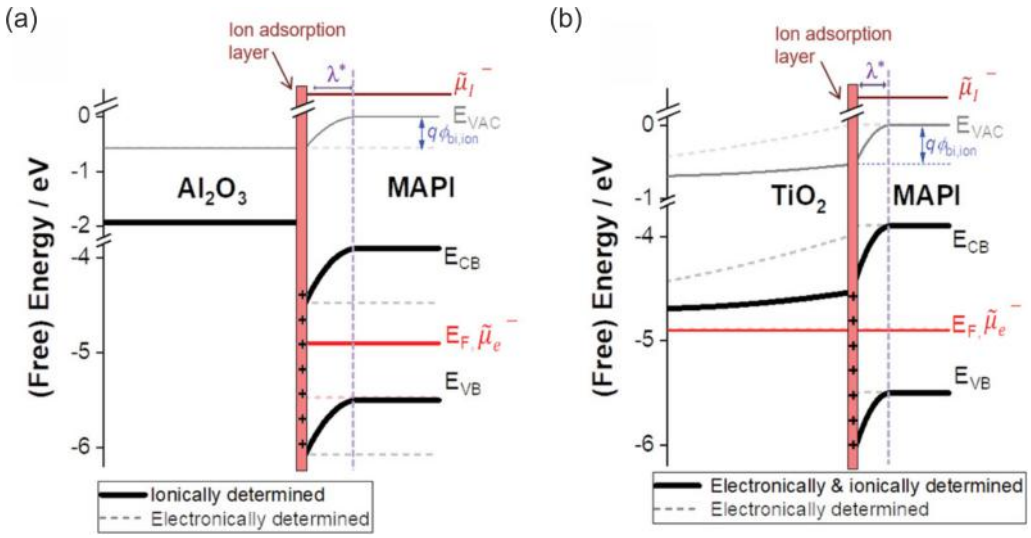

Figure 1.18: Energy diagram with ionically generated space charge in (a) MAPI/Al_2O_3 (b) MAPI/TiO_2 interfaces (reproduced with permission from reference [82]).

and TiO_2 could indeed lead to the depletion of positive charge carriers (*i.e.* iodide vacancies and electronic holes) at the interface between the oxide and MAPI. Since iodide vacancy are majority charge carriers in MAPI, their concentration determines the width of the space charge region and the value of the equilibrium space charge potential.

These experimental results demonstrated that ionically induced space charge effects occur at MAPI-based interfaces (Figure 1.18). Once again, since alumina is an insulator, the behavior is unambiguously attributed to an ionically generated space charge rather than to no electronic contributions. Because TiO_2 is an electronic conductor, additional electronic equilibrium between oxide and MAPI may occur. As Pb^{2+} adsorption at this interface induces a space charge of similar direction with what would be expected based on the materials' work function difference, it is not possible to discriminate their relative contributions.

1.4 Open questions and thesis outline

Despite the importance of interfacial equilibrium for optoelectronic devices based

on hybrid perovskites and the evidence that ionic charge carriers are majority carriers in these systems, the understanding of how mobile ions influence currently developed devices as well as the potential of controlling ionic interactions to design improved devices is still at its infancy.

Among the open questions that requires attention in this context the following are most importnat:

- Is it possible to manipulate or regulate ionically-generated space charges?
- How do the properties of ionic space charges vary between planar and mesoporous device structures?
- What impact does the ionic space charge have on solar cell performance?
- Are ionic space charges a general property of interfaces involving halide perovskites?
- Can the ionic space charge in MAPI be altered when it comes into contact with conductive materials?

In this thesis, I present an experimental investigation of selected interfaces involving hybrid perovskites. In Chapter 2, I present the experimental methods used to fabricate and characterize samples as well as a brief description of the analysis procedure used to analyze the data. Focusing on MAPI as model system, I cover the behavior of mobile ions in this compound when in contact with various materials. The results of my work are presented in Chapter 3. Specifically:

- In Chapter 3.1, I focus on the insulating oxide alumina composite film in MAPI, with and without surface treatment of alumina, in order to examine how the ionic interaction and their space charge contribution can be controlled by using surface modification of oxides in composite configurations.
- In Chapter 3.2, I extend the investigation to the case of MAPI infiltrated in mesoporous TiO_2 devices to demonstrate the applicability of the strategy

mentioned in chapter 3.1 in mesoporous device structure, which is often used as charge transporting layers in real devices.

- In Chapter 3.3, I present the study of mixed conductivity in vertical devices, and highlight the behavior of solar cells to evaluate the impact of ionic space charges in solar cell structures.

- In Chapter 3.4, I investigate the behavior of composite films including other oxide materials. First, I use insulating oxides to obtain a general understanding of ionically induced space charge in halide perovskites. Secondly, charge carrier conducting oxide, NiO, is used to extend knowledge about ionically generated space charges to interfaces with conductive materials.

Overall, this work provides a comprehensive investigation of the ionic charge carrier redistribution and space charge formation at interfaces between MAPI and contacting materials. The findings presented in this thesis have important implications for the design and optimization of halide perovskite solar cells and related optoelectronic devices. They also provide a fundamental understanding of the ionic effects in halide perovskites. By gaining a deeper insight into the ionic interactions and space charge contributions in these systems, we may develop innovative approaches to enhance their performance, ultimately advancing the field.

2 Experimental methods

2.1 Materials and sample preparation

2.1.1 Materials information

Lead(II) iodide (Alfa Aesar, 12724), methylamine hydroiodide (Tokyo Chemical Industry, M2556), lead(II) nitrate (Alfa Aesar, A16345), dimethyl sulfoxide (DMSO) (Sigma Aldrich, 276855), N,N-dimethylformamide (DMF) (Sigma Aldrich, 227756), and anhydrous tetrahydrofuran (THF) (Tokyo Chemical Industry, T2394) are used as purchased without further purification. These samples are kept under argon atmosphere.

Oxide particles used in composite films, such as aluminum oxide (Sigma Aldrich, 544833), silicon dioxide (Sigma Aldrich, 637246), magnesium oxide (Sigma Aldrich, 54649), and nickel oxide (US Research Nanomaterials Inc.) are used after a 200 °C drying process for $>$ 2 hours in argon to remove moisture from the surface of the oxides.

Mesoporous TiO_2 paste (18NR-T, Greatcellsolar) is used for mTiO_2 layer fabrication of horizontal devices. For the surface modification of the oxide surface in this thesis, [2-(3,6-Dimethoxy-9H-carbazol-9-yl)ethyl]phosphonic acid (MeO-2PACz) (D5798, Tokyo Chemical Industry) and benzylphosphonic acid (BPA) (Thermo Scientific, 393340050) are used as purchased and stored under an argon atmosphere.

For solar cell device fabrication, the following materials are used: PbI_2 (Thermo Scientific, 44314), MAI (Greatcellsolar, 101000), titanium diisopropoxide bis(acety-

lacetonate) (Sigma Aldrich, 325252), tin(IV) oxide (Thermo Scientific, 044592.36), mTiO_2 paste (30NR-D, Greatcellsolar), poly(3,4-ethylenedioxythiophene):polystyrene sulfonate (PEDOT:PSS) (Ossila, M121), spiro-OMeTAD, and phenyl-C61-butyric acid methyl ester (PCBM) (Xian Polymer Light Technology Corp., PLT 5020NT and 305006). As dopants for spiro-OMeTAD, tert-butylpyridine (tBP) (Sigma Aldrich, 1442379) and lithium bis(trifluoromethylsulfonyl)imide (LiTFSI) (Sigma Aldrich, 15224) are used. Acetylacetone (Sigma Aldrich, P7754), DMSO, DMF, and chlorobenzene (Acros organics, 326870010, 326880010, and 396970010) are used as purchased.

Iodine crystal (Alfa Aesar, 10619) is used in experiments with controlled iodine partial pressure.

2.1.2 Precursor preparation

1.5 M MAPI solution: PbI_2 (2.075 g, 4.5 mmol) and MAI (0.715 g, 4.5 mmol) are put into 3 mL of DMSO. This solution is then heated at 50 °C. After the powders are dissolved, the solution is cooled down to room temperature and filtered using a 0.45 μm syringe filter.

Surface modification of alumina: To modify the surface of alumina with organic sensitizers, 16.8 mg of MeO-2PACz and 8.5 mg of BPA are added separately to 50 mL of anhydrous THF each. Then, 0.5 g of alumina nanoparticles is added to 10 mL of each solution and left for 24 hours in the dark. The particles are separated by centrifugation at 8000 rpm for 8 min. Following centrifugation, the separated particles are mixed with 20 mL of THF and centrifuged again. The particles are then dried at 60 °C while being ground with a mortar. Next, the dried particles are mixed with 20 mL of DMSO and centrifuged. Finally, the separated particles are dried at 110 °C with mortar grinding.

Precursor solution of oxide:MAPI composite films: For 0.8. vol% nominal volume fraction Al_2O_3:MAPI and SiO_2:MAPI composite film, 7.08 mg of alumina and 4.75 mg of silica are mixed with the filtered 1 mL of 1.5 M MAPI precursor solution in

DMSO, relatively. For 0.3 vol% nominal volume faction of Al_2O_3:MAPI, SiO_2:MAPI, MgO:MAPI and NiO:MAPI composite films, 2.65 mg of Al_2O_3, 1.78 mg of SiO_2, 2.41 mg of MgO and 4.48 mg of NiO are mixed with the filtered 1 mL of the 1.5 M MAPI solution.

0.75 M MAPI in mixed solution: PbI_2 (2.075 g, 4.5 mmol) and MAI (0.715 g, 4.5 mmol) are put into mixture of 5.25 mL of DMF and 0.75 mL of DMSO. This mixed solution is heated at 50 °C until all powders are dissolved. After cool it down to room temperature then, the solution is filtered with 0.45 μm syringe filter.

MAPI and oxide composite solution for solar cell devices: PbI_2 (2.014 g, 4.4 mmol) is put into mixed solvents of 2.4 mL of DMF and 0.6 mL of DMSO. This solution is heated at 90 °C until all powders are dissolved. The solution is then cooled down and mixed with MAI (0.668 g, 4.2 mmol). The MAPI precursor solution is used without filtering. For oxide:MAPI composite solution with 0.80 vol% nominal oxide concentration, 4.56 mg of alumina with or without surface modification is mixed into 0.4 mL of MAPI solution.

2.2 Device fabrication

2.2.1 Horizontal devices

Electrode fabrication: An interdigitated gold electrode pattern is fabricated on a sapphire (0001) substrate with finger width of 5 μm, spacing between the fingers of 10 μm, and thickness of 200 nm using photolithography. To enhance the adhesion between the gold layer and sapphire, a 20 nm thick layer of chromium is evaporated prior to the gold deposition.

The substrate with the interdigitated gold electrode is cleaned before sample fabrication. First, it undergoes sonication in distilled water, acetone, and isopropanol for 5 minutes each. The lithography and evaporation are performed by myself and Achim Güth (Nanostructuring Lab, Max Placnk Institute for Solid State Research).

After drying the substrate, it is further cleaned using oxygen plasma.

Mesoporous TiO_2 layer: $mTiO_2$ paste is mixed with ethanol as a TiO_2 paste-to-ethanol weight ratio of 1:1.15. After cleaning the substrates as described above, a 30 μL solution of $mTiO_2$ in ethanol is dropped onto the substrate. Spin-coating is then performed at 4000 rpm for 30 seconds. The sample is subsequently transferred to a hot plate and heated at 125 °C for 5 minutes. The sample is then heated up to 450 °C with 2 hours ramp then sintered for 30 minutes.

Surface modification of $mTiO_2$ layer: 8.4 mg of MeO-2PACz and 4.3 mg of BPA are dissolved in 50 mL of anhydrous THF. 8×8 mm of $mTiO_2$ on gold electrode or ITO is put into this solution for 24 hours, right after sintering process. Film is taken out from solution and washed in 5 mL of THF solvent. The sample is then dried at 60 °C for 6 min on hot plate.

MAPI and composite film fabrication: 30 μL of the prepared precursor solution is dropped on the cleaned substrates, under argon gas atmosphere. The following spin coating program is used. For 1.5 M MAPI, step 1: acceleration time 1 s, spin speed 65 rps, duration 1 s; step 2: acceleration time 1 s, spin speed 150 rps, duration 180 s. When 165 s are left in whole process, 500 μL of chlorobenzene is dropped. For 0.75 M MAPI, step 1: acceleration time 1 s, spin speed 65 rps, duration 1 s; step 2 acceleration time 1 s, spin speed 100 rps, duration 5 s. 5 seconds after the beginning of the program, 500 μL of chlorobenzene are dropped. After spin coating, films are dried for 1 minute and 10 seconds for 1.5 M MAPI and 0.75 M MAPI, respectively. The films are then annealed at 100 °C for 5 minutes.

2.2.2 Solar cell devices

Solar cells were fabricated during visits at the Laboratory of Photonics and Interfaces (Prof. Michael Grätzel) at École Polytechnique Fédérale de Lausanne (EPFL).

Electrode preparation and compact TiO_2 layer: 4 mm thick FTO coated glass substrates (10 Ω/cm^2) are chemically etched using zinc powder and 4 M of HCl (substrate size 2.5×1.6 cm^2). The substrates are then washed in distilled water. The

substrates are put in sonication with Hellmanex 2% solution in distilled water, followed by brushing and rinsing with distilled water. Following cleaning in water, they are sonicated with acetone and ethanol for 10 minutes each. Finally, air is blown on them for drying.

The solution of compact TiO_2 layer is prepared with 600 μL of titanium diisopropoxide bis(acetylacetonate), 400 μL of acetylacetone and 14 mL of ethanol. The substrates are placed on a hotplate with a metal mask. Then the temperature of the hotplate is increased up to 450 °C. The solution is sprayed with oxygen as gas carrier. After spraying, the temperature of the hot plate is kept at 450 °C for 20 minutes, followed by slow cooling down of the plate to room temperature.

Mesoporous TiO_2 layer: mTiO_2 paste is mixed with ethanol with a TiO_2 paste-to-ethanol weight ratio of 1:10, 1:8 and 1:5. The substrates with compact TiO_2 layer are cleaned with oxygen plasma, then the mTiO_2 solution is spin coated under ambient condition. A 50 μL solution of mTiO_2 in ethanol is dropped onto the substrate. Spin-coating is then performed at 4000 rpm for 20 seconds. The sample is subsequently transferred to a hot plate and heated at 85 °C for 5 minutes. After the solvent is dried, the sample is heated up and sintered as follow: 125 °C for 5 minutes, 325 °C for 5 minutes then 450 °C for 30 minutes. After sintering, temperature is slowly cooled down to room temperature.

Surface modification of mTiO_2 layer: 0.8 mg of MeO-2PACz and 0.4 mg of BPA are dissolved in 5 mL of anhydrous THF. The 60 μL of solution is dropped on mTiO_2 layer then accelerated up to 4000 rpm, and spin coated for 20 seconds. The substrate is dried on a hot plate at 60 °C for 5 minutes. After drying, the substrate is spin coated again by 60 μL of THF and dried again at 60 °C for 5 minutes.

MAPI and composite film fabrication: The mTiO_2 layer is cleaned with oxygen plasma then moved into dry air box. The surface modified mTiO_2 substrate is moved into dry air box right after surface modification process. 50 μL of the MAPI precursor solution is dropped on the mTiO_2 layer. The following spin coating program is used. Step 1: acceleration time 5 s, spin speed 1000 rpm, duration time 10

s; step 2: acceleration time 2.5 s, spin speed 5000 rpm, duration time, 22.5 s. 200 μL of chlorobenzene is dropped when 15 seconds are left in the program. MAPI layer is annealed at 100 °C for 5 minutes.

Hole and electron transporting layers for solar cell and unipolar devices: For the fabrication of the SnO_2 layer, purchased SnO_2 solution is mixed with distilled water as 1:6 volume ratio then sonicated for 10 minutes. This solution is spin coated on ITO substrates under ambient at 3000 rpm for 30 seconds. Then the substrate is dried at 180 °C for 30 minutes. For the spiro-OMeTAD layer, 92 mg of spiro-OMeTAD is mixed with 44 μL of LiTFSI solution (520 mg LiTFSi in 1 mL of acetonitrile), 36.8 μL of tBP and 1007.4 μL of chlorobenzene. This solution is spin coated on MAPI layer at 4000 rpm for 30 seconds and dried under dry air atmosphere at room temperature under ambient light. PCBM layer is fabricated by spin coating of a PCBM solution in chlorobenzene (20 mg/1 mL) at 3000 rpm for 30 seconds. PEDOT:PSS is filtered with 0.45 μm syringe filter then spin coated on ITO substrates at 3000 rpm for 30 seconds. Then the samples are dried at 120 °C for 15 minutes.

2.3 Materials and Device Characterization

2.3.1 Crystallinity and morphology of films

Zeta potential is used to check ionic interaction on the surface of oxides in MAPI precursor solution at room temperature using electroacoustic DT-1200 spectrometer (Dispersion Technology, Inc., Quantachrome). MAI, PbI_2, $Pb(NO_3)_2$ are dissolved in DMSO with the oxide nanoparticles at 2 wt%. Salt is mixed with solvent first. After all salt is dissolved under argon atmosphere, oxide particle is dispersed under ambient atmosphere. Right after dispersion of oxide particle, the zeta potential is measured under ambient atmosphere.

XRD is used to determine the crystal structure of the MAPI film. An X-ray diffrac-

tometer (Empyrean Series 2, PANalytical GmbH) with a Cu Kα radiation energy of 40 kV and a current of 40 mA are used. The samples were mounted in a domed airtight sample holder (PANalytical) under argon atmosphere. XRD measurements were performed by myself and by Helga Hoier of Department of Physical Chemistry of Solids in Max Planck Institute for Solid State Research.

XPS is measured using Kratos Axis Ultra, Mon-ochromatic Al kα (hν = 1486.6 eV); survey scans PE 80, detail scans PE 20. The sample is moved from argon glove box to XPS machine directly using an airtight sample holder without exposure to air. XPS is performed by Kathrin Küster of Interface Analysis group in Max Planck Institute for Solid State Research.

ICP-OES is performed by using SPECTRO CIROS. The intensity obtained from measuring each line was compared to previously measured intensities of known concentrations of the elements, and their concentrations were then computed by interpolation along the calibration lines. The dissolved sample is introduced into the inductively generated argon plasma via an atomizer system and excited. The emitted radiation is transferred to the ICP spectrometer where it is split into the individual wavelengths and evaluated. The intensities of the spectral lines are measured with CCD semiconductor detectors. Calibration is carried out with multi-element solutions mixed from standard solutions or single-element solutions. ICP-OES is performed by Samir Hammoud of chemical synthesis group in Max Planck Institute for Intelligent systems.

DC Galvanostatic polarization is performed using a Keithley source meter (2634B) under dark, and under argon conditions (oxygen $<$ 15 ppm) or fixed iodine partial pressure using argon as carrier gas. A constant current step is applied to the device after equilibration of the resting voltage. The evolution of the voltage is recorded as function of time. The current value is selected so that the measured voltage remains below $\sim$ 50 mV.

Electrochemical impedance spectroscopy (or AC impedance) is measured using a Novocontrol spectrometer with a 2-wire configuration in the frequency range between

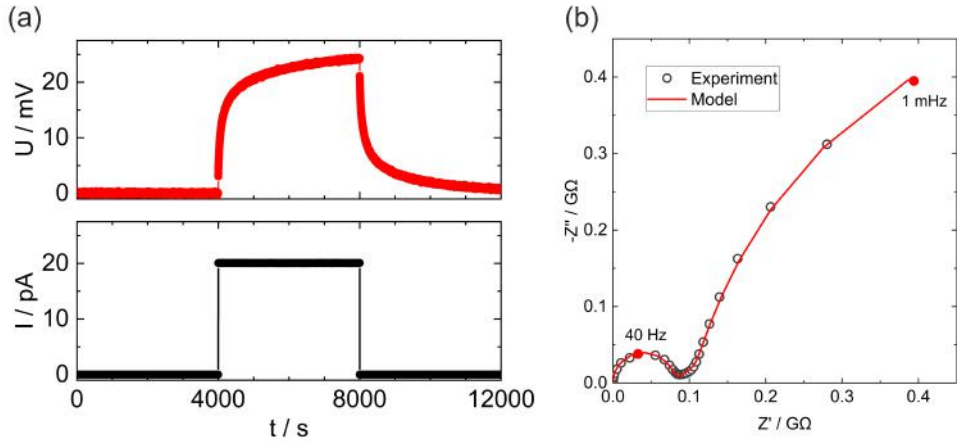

Figure 2.1: (a) DC polarization measurement and (b) Nyquist plot of the AC impedance spectrum of a MAPI sample, both measured under argon in the dark.

1 MHz - 1 mHz, using an AC voltage amplitude of 20 mV (Figure 2.1).

Current-Voltage characterization of solar cells is performed under ambient condition, dark and upon illumination (1 Sun) using source meter (Keithley 2400) and Xenon lamp (Oriel, USA). The cells are left at 0 V for 5 s, then a forward/reverse scan of the voltage is performed using a scan rate of 0.05 V steps and 0.1 s time delay. Measurements under dark and under 1 sun equivalent illumination are recorded. From the measurement under light, the short circuit current density (J_{SC}), the open-circuit voltage (V_{OC}), the fill factor (FF) and the PCE of the devices are evaluated.

2.3.2 Iodine partial pressure measurement

Controlling the iodine partial pressure in the conductivity measurement was performed following literature [33, 83]. Argon is flown in a quartz container with iodine crystals. The quartz container is kept in a thermostat at a fixed temperature. The iodine partial pressure is calculated based on the equilibrium pressure of iodine at the thermostat temperature [84].

2.4 Data analysis

Electronic (R_{eon}) and ionic resistances (R_{ion}) are extracted from the electrical measurements and the corresponding partial conductivities are evaluated using:

$$\sigma = \frac{1}{R}\frac{L}{Wl} \tag{2.1}$$

where W is the total overlap between the electrode fingers in the interdigitated structures, L is distance between the fingers and l is thickness of the MAPI layer. Equivalent circuit models of the impedance spectra is fitted using Z-view. Detailed evaluation of σ_{eon}, σ_{ion} is described in reference [85] for the case of pristine MAPI. Briefly, the high frequency feature of the impedance spectrum is used to estimate the total conductivity σ_{tot} (due to both electronic and ionic charge carriers). As gold is assumed to be ion-blocking in these devices, the electronic conductivity is extracted from the long time scale behavior recorded in the DC measurement. The ionic conductivity is then evaluated as $\sigma_{ion} = \sigma_{tot}$ - σ_{eon}. For the analysis of the impedance of composite films or MAPI infiltrated in mesoporous structures, different analysis was performed to account for the effect of blocking grain boundaries, constriction in the pores *etc.* as described in detail in each section of Chapter 3.

3 Results and discussion

3.1 Modulation of ionically-generated space charge effects at hybrid perovskite-oxide interfaces via surface modification

Ionically-generated space charges forming at the interface of MAPI with alumina were observed in previous work conducted by Kim *et al.* [82]. This finding has major significance in the field of photovoltaics and, more in general, in optoelectronics, as it emphasizes that not only electronic effects but also ionic effects are important when determining the equilibrium situation at the interface of halide perovskite mixed conductors with contacts.

It is important to note that such ionically-generated space charge effects are not exclusive to alumina. As it will be shown in Chapter 3.4, similar behavior is observed whenever MAPI is in contact with other materials that exhibit specific ionic interactions.

An important question to consider is whether, given a certain contact phase, such ionic interaction can be controlled and systematically varied at the sample preparation stage. Achieving modulation of ionic adsorption and exchange reactions at interfaces is expected to impact the space charge formation and the charge dynamics in devices. Ultimately, this could become a novel route towards optimization strategies in optoelectronics.

Surface modification is used in this study to investigate how it influences the formation of space charges, with a specific focus on ionically-generated space charges. Surface modification techniques are widely used for improving interfacial properties in solar cell applications. In several instances, they are applied with the intention of varying the electronic energy level situation and allow for better charge extraction, or charge carrier blocking *etc.* Fewer studies have considered such strategy in the context of ionic interactions. For example, from Kelvin probe force microscopy, Weber *et al.* suggested that anion vacancies localize at the interface between MAPI and SnO_2 [14]. Based on a report by Tumen-Ulzii *et al.*, a fullerene derivative self-assembled monolayer (SAM) can reduce such ionic interactions between SnO_2 and halide perovskites, resulting in a reduction of hysteresis in devices [86]. Their interpretation is that the SAMs reduce the surface concentration of -OH functional group on SnO_2, which in turn reduces cation attraction at the interface. Their study focuses on the change in reduction of cation interaction at the interface between halide perovskite and SnO_2 when incorporating the molecular monolayer, however no direct evidence of the reduced cation adsorption or of its effect on the interfacial space charge was reported.

Surface modification via SAMs is used not only as ion blocking strategy, but also for improving charge extraction and defect passivation [87–90]. However, to the best of my knowledge, there has been no systematic study on how the use of surface modifying molecules impacts the formation of space charges and the resulting charge carrier redistribution. This is especially true with regard to ionically-generated space charges.

This study aims to fill this knowledge gap by examining the effects of surface modification on ionically-generated space charges. The Al_2O_3/MAPI interface is used as model system and the scheme outlining the hypothesis of this study is depicted in Figure 3.1. I employ [2-(3,6-Dimethoxy-9H-carbazol-9-yl)ethyl]phosphonic Acid (MeO-2PACz) and Benzylphosphonic acid (BPA), organic molecules commonly used for interface engineering in PSCs [91–95]. These molecules have a phosphonic acid

group, which is expected to chemisorb on the alumina surface creating a stable molecular monolayer [96–99]. As discussed in the introduction and in detail below, the observed change in charge carrier behavior in the Al_2O_3/MAPI interface can only be caused by an ionic interaction. The hypothesis in this study is therefore that changes caused by the surface modification of the oxide with the selected molecular compounds affects primarily such ionic interaction between MAPI and alumina. In principle, while these molecules can create a barrier for ion adsorption, they are not expected to impede electronic charge carrier equilibration with the oxide (electron can tunnel towards to oxide over such short distance). To remove such uncertainty, the use of electronically insulating alumina allows one to disregard any electronic effects and to focus solely on ionic interactions.

The first part of this chapter demonstrates the preparation of the surface modified particles and examines the ionic interactions occurring on the alumina surface with MAPI's precursor components. Following this, the results of measurements of both ionic and electronic conductivities performed on composite films where either Al_2O_3 or surface modified Al_2O_3 nanoparticles are embedded in a MAPI film at various iodine partial pressures and temperatures are presented. Finally, the discussion centers around the calculation of the space charge potential changes based on the experimental findings.

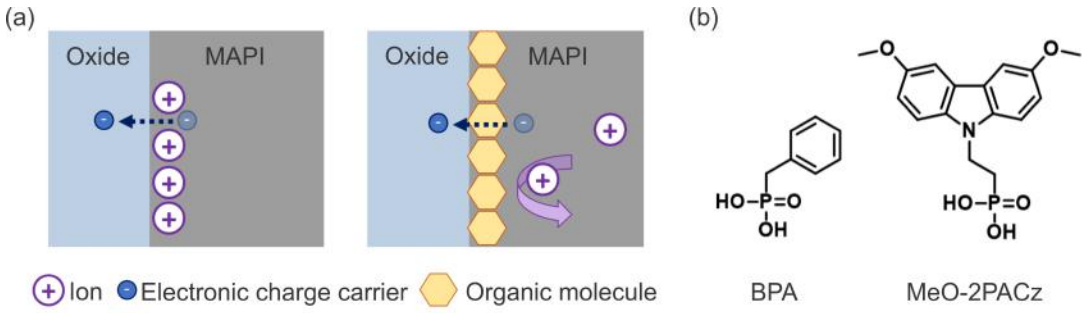

Figure 3.1: (a) A sketch illustrating the ionic interaction blocking effect of organic molecules on alumina, as well as (b) the molecular structures of MeO-2PACz and BPA.

3.1.1 Oxide surface modification and modulation of ionic interactions

Since the composite films based on MAPI are fabricated via solution processing, it is first of all necessary to determine whether the molecules used in this study can be effectively anchored onto the alumina surface and withstand the exposure to the relevant solvent (DMSO). To test this, Fourier-transform infrared spectroscopy (FTIR) measurements are carried out on the alumina particles coated with the organic molecule. Alumina particles (< 50 nm) are immersed in a solution of either MeO-2PACz or BPA in THF with a concentration of 1 mM for 24 hours (see also Chapter 2). The particles are then washed with THF solvent, and FTIR measurements are taken under Ar atmosphere. Subsequently, the particles are subjected to an additional washing step using DMSO. This step is used to test the stability of the molecule towards exposure to the solvent used in the MAPI precursor solution. A second FTIR measurements on the same particles is then performed and the data is compared in Figure 3.2. The FTIR spectrum of alumina with MeO-2PACz surface modification exhibits distinct peaks when compared with the baseline referring to the bare alumina. These include a peak at 1576 cm^{-1}, which corresponds to the asymmetric stretching of the ring with the methoxy group. Additionally, peaks within the range of 1493 - 1436 cm^{-1} indicate the aromatic C=C in-plane stretch. The stretching vibration of the carbazole ring is represented by peaks in the 1329-1289 cm^{-1} range, while a peak at 1246 cm^{-1} corresponds to C-N stretching in the carbazole group. Furthermore, absorption peaks at 1130 - 1174 cm^{-1} and 1040 - 1059 cm^{-1} can be attributed to the presence of P=O and P-OH functional groups, respectively, which are associated with the phosphonic acid group. The BPA surface-modified alumina revealed the presence of peaks at 1496 and 1452 cm^{-1}, indicating the presence of aromatic C=C bonds. Additionally, in the 1040 - 1250 cm^{-1} range, absorption peaks associated with P-OH and P=O functional groups were observed [100]. These tests confirmed that FTIR peaks from the organic molecules were still

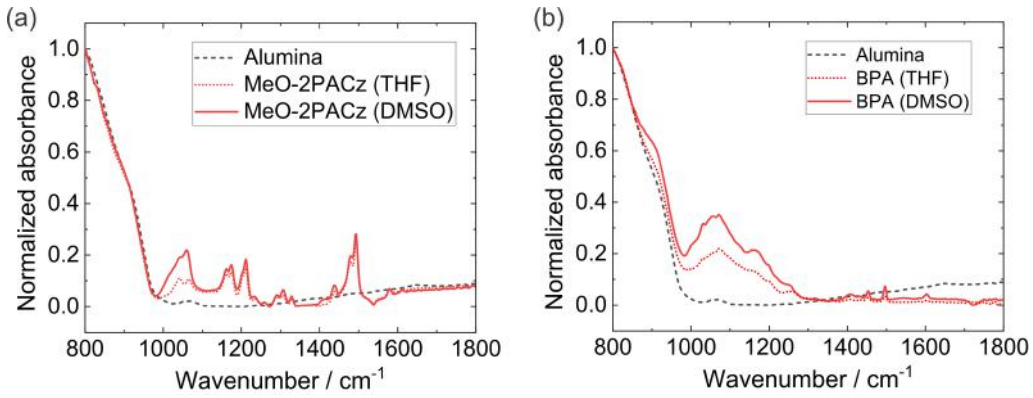

Figure 3.2: FTIR results of surface modified alumina following THF and DMSO washing

detectable even after DMSO washing, indicating that the molecules remained stably anchored to the alumina surface.

In order to examine the effect of MeO-2PACz and BPA on the ionic interaction at the surface of Al_2O_3 in MAPI precursor solutions, zeta potential measurements are performed in a DMSO solution containing various salts such as MA^+, Pb^{2+}, or I^- (Figure 3.3). The zeta potential value of Al_2O_3 in the $Pb(NO_3)_2$ in DMSO solution is tested for the different particles. This $Pb(NO_3)_2$ solution was previously used to isolate the interaction of Pb with the alumina surface from more complex adsorption mechanisms involving Pb-halide complexation [82]. The value of the zeta potential for the alumina case is on the order of 40 mV, and it was found to decrease in the case of surface modified oxide compared to bare Al_2O_3. The data indicate that the presence of MeO-2PACz and BPA molecules reduces the adsorption of Pb cations onto the alumina surface in this solution.

Further experiments are carried out with other precursor combinations. The zeta potential value measured in the presence of PbI_2 showed a value close to zero while a negative zeta potential value is observed in the case of a mixed solution of PbI_2 and MAI. As mentioned above, this discrepancy with $Pb(NO_3)_2$ can be attributed to the complexation of Pb and I ions in the polar solvent [82]. As a result, the zeta potential values in the PbI_2, mixed PbI_2 and MAI salt solutions are unreliable. In any case, the use of zeta potential in suspensions of particles to estimate ionic

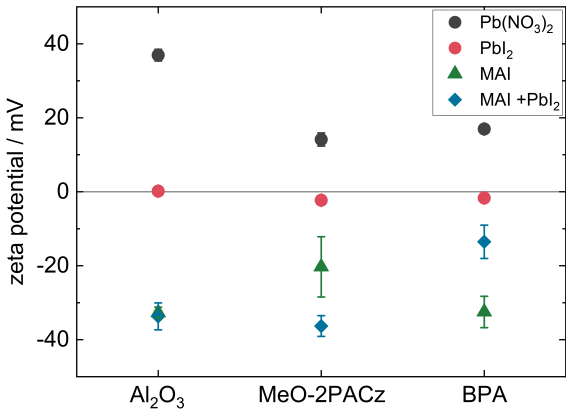

Figure 3.3: The zeta potential measurements results that were obtained by dispersing the oxide particles of alumina, surface modified alumina by MeO-2PACz and BPA with a 2 wt% concentration within 0.5 M salt in DMSO solutions.

interactions in the solid state should be discussed with caution, given the difference in the two environments.

Composite thin films were fabricated using spin coating methods. These films consist of MAPI with embedded oxide particles. The alumina particles, whether bare or surface-modified, were immersed in a precursor solution of MAPI (1.5 M MAI and PbI_2 in DMSO) with a nominal concentration of 0.8 vol% (see Chapter 2 for details). Such concentration was estimated to be large enough to result in a measurable effect of the interfacial space charge on the conductivity properties of the sample, but small enough not to cause significant blocking of mobile charge carriers (see Appendix, Figure 1).

XPS measurements were conducted to gain further insights into the ionic interaction between MAPI and both bare and surface-modified alumina (Figure 3.4). All films were fabricated on SiO_2 substrates. In the case of the Al_2O_3:MAPI film (referred to as A:MAPI below), an Al peak was detected, whereas no such peak was observed for the MeO-2PACz-Alumina:MAPI (MeO:MAPI) and BPA-Alumina:MAPI films. This striking difference indicates that the organic molecules fully cover the surfaces of the alumina particles and further corroborates the FTIR results. Also a shift in the oxygen peak was observed in the A:MAPI film, but not in the MeO:MAPI

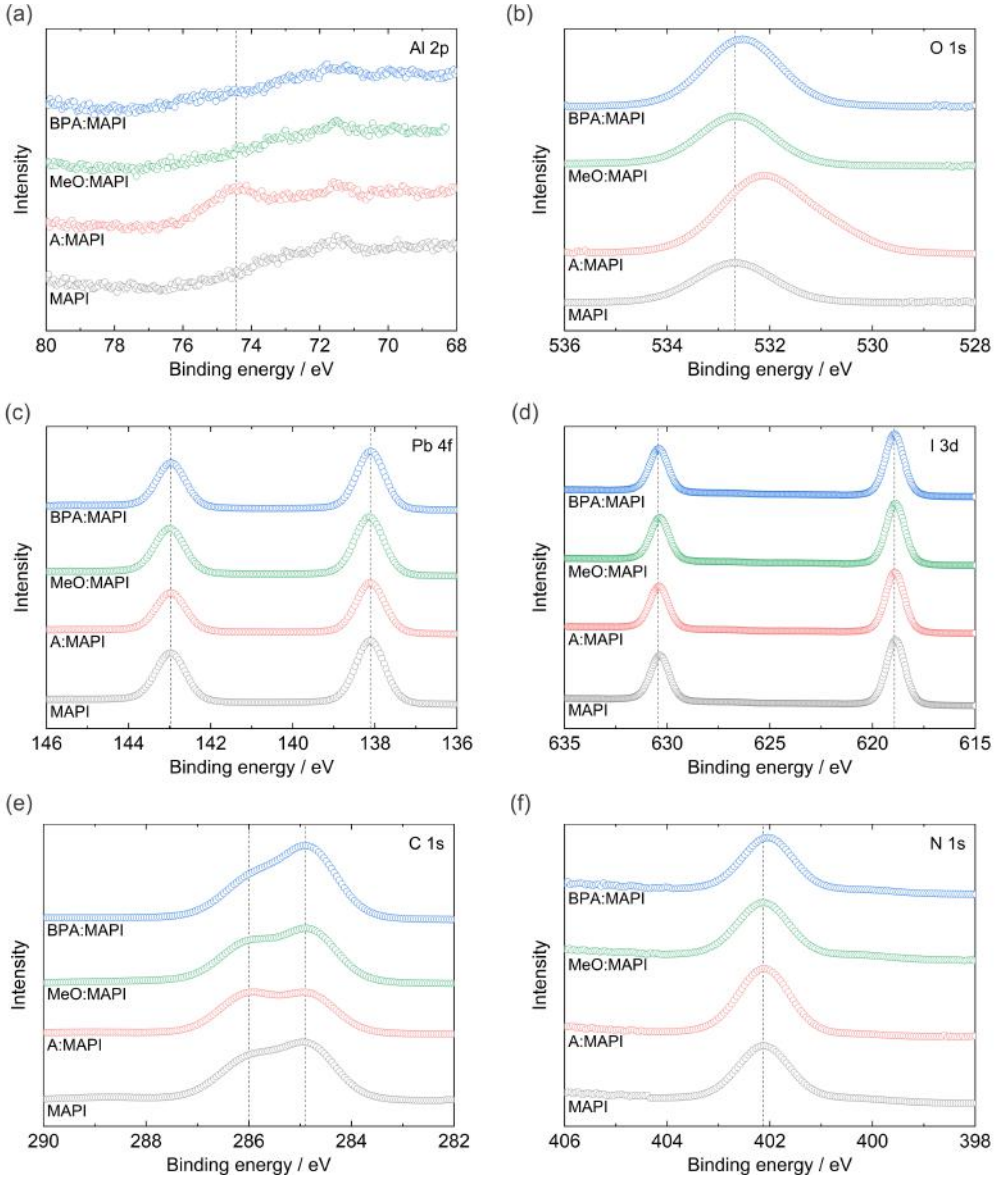

Figure 3.4: XPS measurements of MAPI, A:MAPI, MeO:MAPI and BPA:MAPI on SiO_2 substrates. All composite films are fabricated with 0.8 vol% nominal concentration of oxide particles in MAPI.

and BPA:MAPI films. In the MAPI sample, the oxygen peak is detected because of the oxygen contamination (hydroxides, water *etc.*). For the A:MAPI case, the oxygen peak is shifted because of the presence of the alumina particles. The MeO:MAPI and BPA:MAPI samples showed no peak shift compared to MAPI, because organic molecule are fully covered the oxides particles so that the contribution of alumina

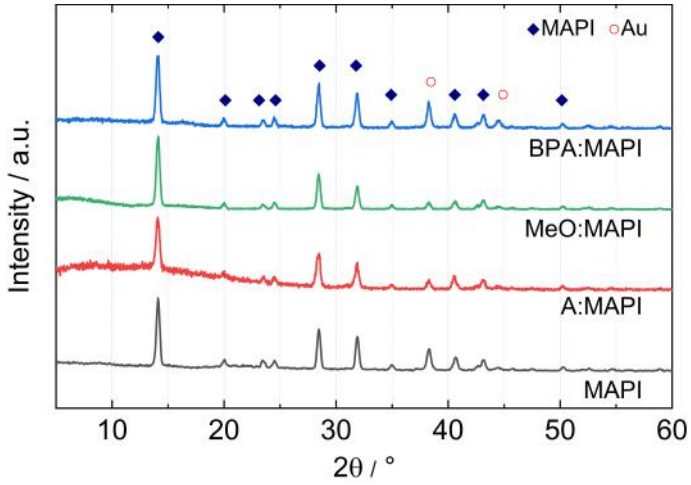

Figure 3.5: XRD results of MAPI, A:MAPI, MeO:MAPI and BPA:MAPI films. All films showed MAPI tetragonal crystal structure without PbI_2 which is degradated product.

disappears. As for the C, N, Pb, and I peaks, no significant changes were observed across the different samples. This is expected given the relatively small ratio of the oxide particles, resulting in a low surface to MAPI bulk ratio that makes changes in peak intensities due to interfacial effects difficult to detect.

Composite films were fabricated on alumina substrates with interdigitated Au electrodes for conductivity measurements (see Chapter 2). Three different samples were prepared: A:MAPI, MeO:MAPI, and BPA:MAPI, as well as a control sample consisting of a MAPI film without any oxide particles. The crystal structure of the MAPI and composite films on the alumina substrate with Au electrodes was analyzed using XRD (as shown in Figure 3.5). All films displayed peaks that corresponded to the tetragonal structure of MAPI, without significant PbI_2 peaks, confirming the absence of significant residue from the fabrication process or degraded MAPI product. No peaks associated with oxide particles were detected, possibly due to the dispersion of small particles (less than 50 nm) with a low volume fraction in films. ICP measurements confirmed the presence of the particles in these films, indicating their actual volume fractions of oxide. The estimated volume fraction of oxide was found to be 1.6 vol% for both the A:MAPI and MeO:MAPI films. The BPA:MAPI

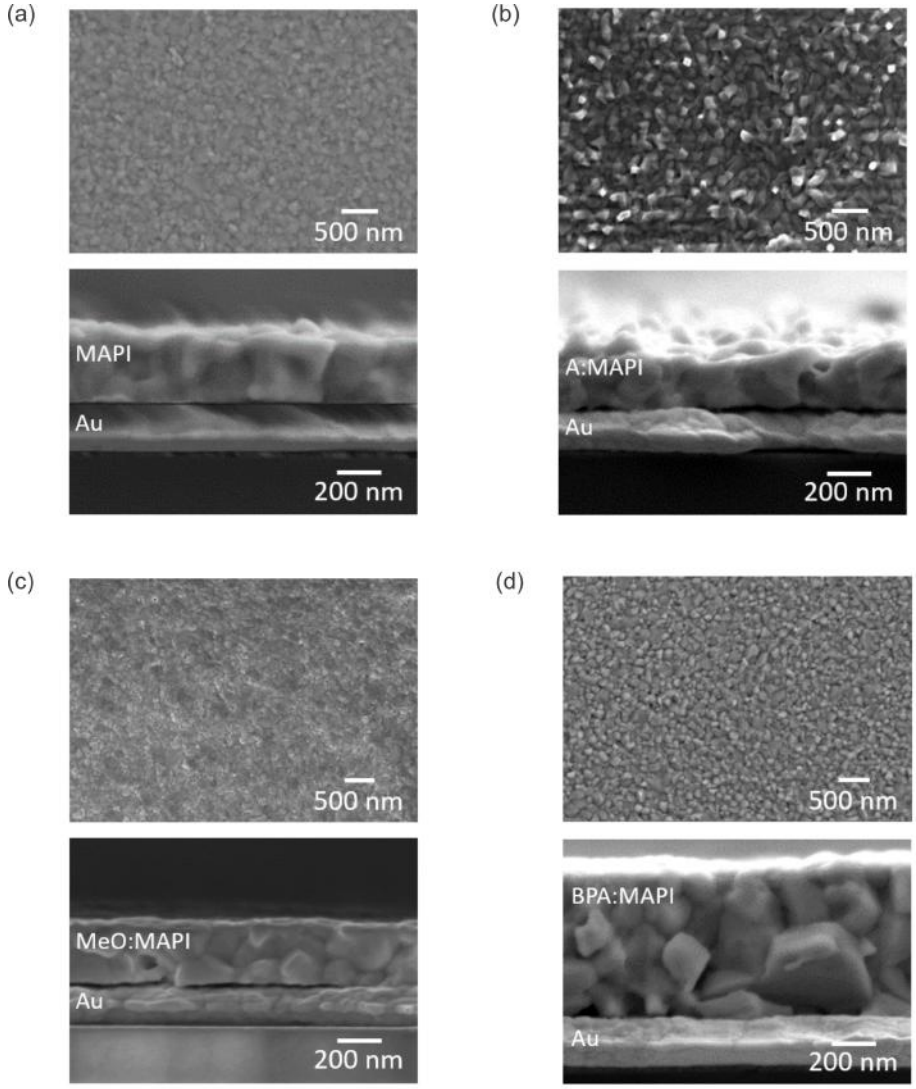

Figure 3.6: The surface (above) and cross-sectional (below) SEM images of the following are shown: (a) MAPI, (b) A:MAPI, (c) MeO:MAPI and (d) BPA:MAPI films with 0.8 vol% nominal volume fraction.

film exhibited a higher volume fraction of oxide, the measured value is 1.8 vol% which is higher than the nominal concentrations (0.8 vol%) in the precursor state.

The film morphology was checked using SEM (Figure 3.6). All films, including the MAPI control, showed similarly sized crystals in the range of 180 - 200 nm. The A:MAPI film showed enhanced roughness compared with the control MAPI sample. This might be due to the tendency of the alumina particle to aggregate within the film, giving rise to a slightly less homogeneous morphology. Interestingly,

the composite films MeO:MAPI and BPA:MAPI exhibited reduced roughness in comparison to A:MAPI film, which could be attributed to an improved dispersion of the surface modified particle in the solution and in the film compared to the bare particles (Figure 2 in appendix). Cross-sectional SEM images revealed that MeO:MAPI and BPA:MAPI films are thicker an the A:MAPI and MAPI films.

3.1.2 Measurements of electronic and ionic conductivities of composite films with surface modification

The electronic and ionic conductivities of MAPI, A:MAPI, and surface-modified alumina:MAPI composite films (MeO:MAPI and BPA:MAPI) were investigated under different conditions. All films are fabricated on alumina substrates with interdigitated Au electrodes as described in the previous section. The extraction of the partial conductivities is described in detail in the Experimental methods section.

Figure 3.7 shows the impedance and the DC polarization measurements performed in argon atmosphere (O_2 < 10 ppm). The total conductivity (including both electronic and ionic conductivity) of the sample is calculated from high and mid-frequency features of the impedance spectra. By including the mid-frequency feature in the estimate of σ_{tot} the ionic resistance related to the bulk and also to the grain boundaries is accounted for in the evaluation [34].

The electronic conductivity of A:MAPI films is more than one order of magnitude higher than that of MAPI under argon condition (Figure 3.8). This striking result, *i.e.* electronic conductivity enhancement on addition of an insulating phase, is due to heterogeneous doping by alumina and is consistent with previous reports on these films as well as reports where alumina is embedded in a mixed conducting host [82, 101]. Both MAPI and A:MAPI films exhibited similar ionic conductivities, approximately 10^{-8} S/cm. This result suggests that, while the favorable interfacial contribution to the electronic conduction is effective at this particle volume fraction, the conductivity reduction expected from the depression in the ionic charge carrier

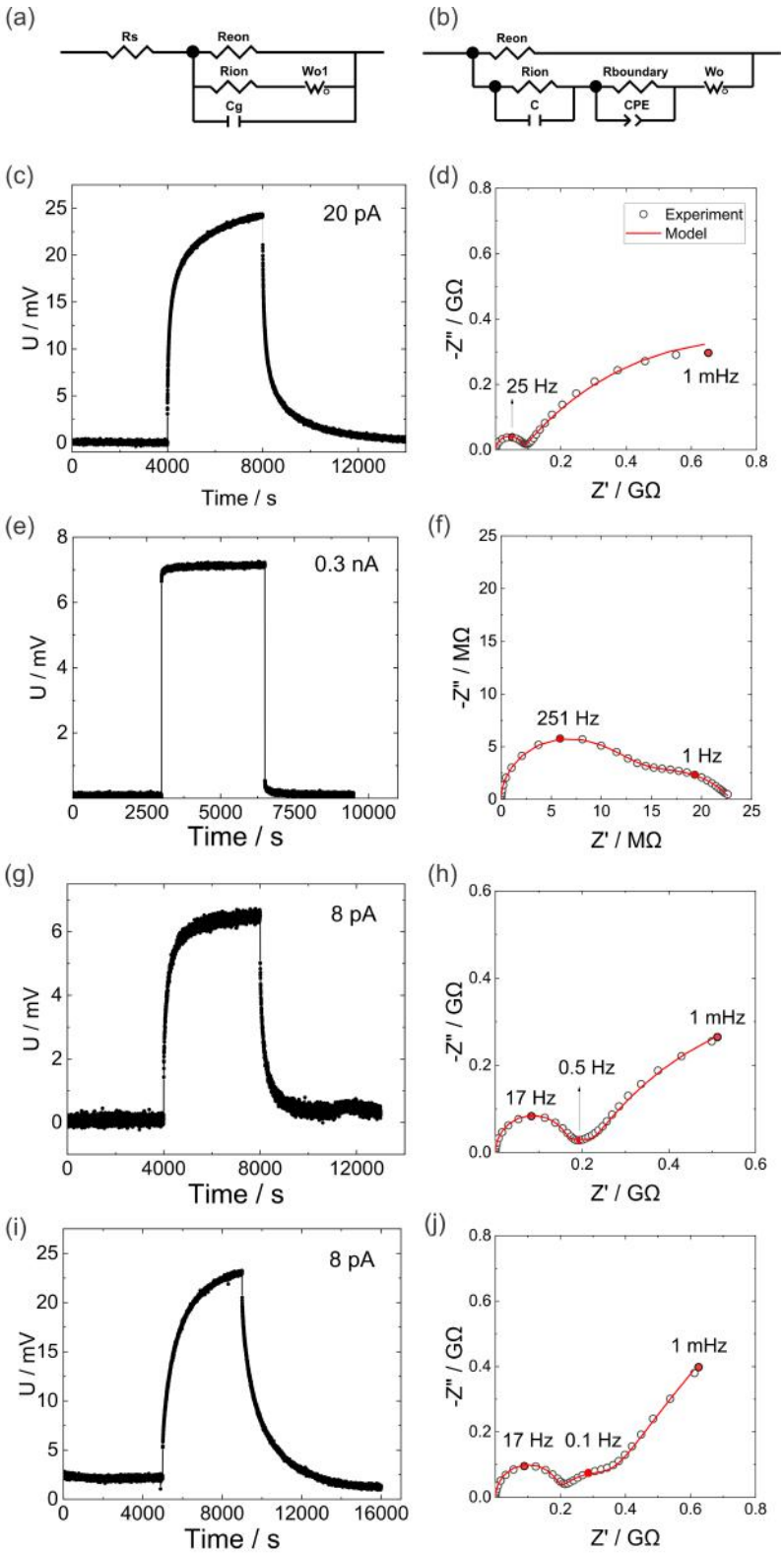

Figure 3.7: The model that is used for AC impedance fitting. (a) standard circuit is used for MAPI, A:MAPI films. Model (b) is used for MeO:MAPI and BPA:MAPI films. The DC polarization curve and AC impedance measurement of (c, d) MAPI (e, f) A:MAPI (g, h) MeO:MAPI and (i, j) BPA:MAPI film in argon atmosphere.

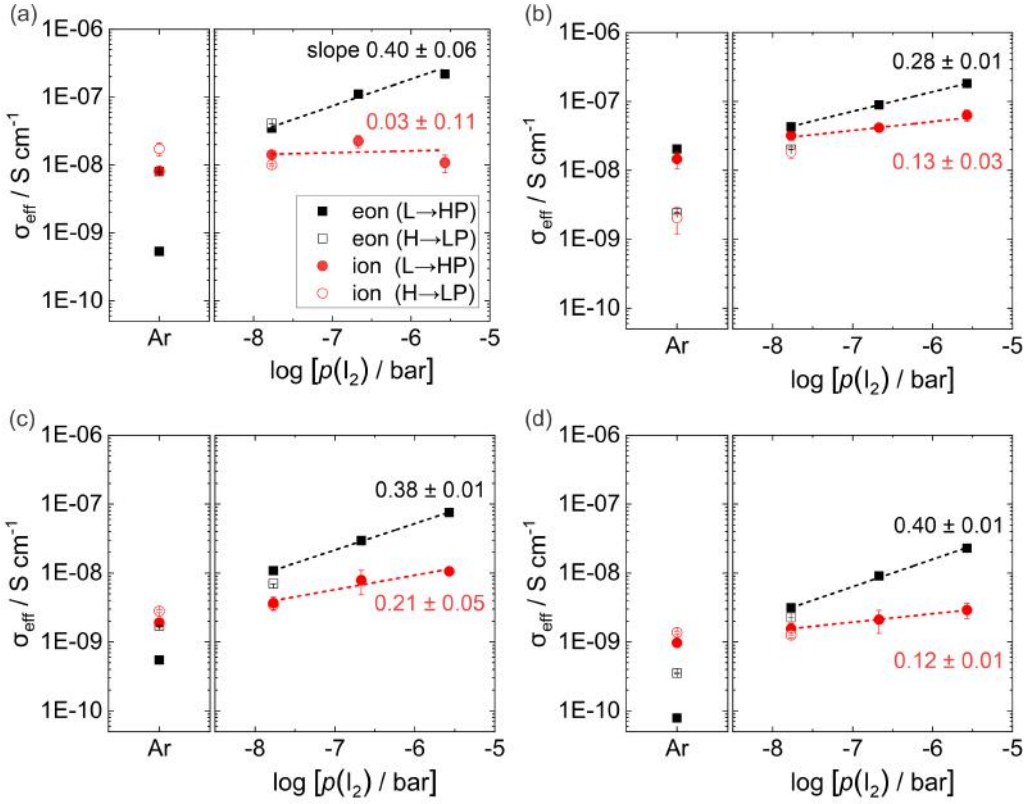

Figure 3.8: Electronic and ionic conductivity measurement results in Ar and different iodine partial pressure condition of (a) MAPI, (b) A:MAPI, (c) MeO:MAPI and (d) BPA:MAPI films.

concentration in the space charge region is not evident. This may be due to the presence of percolating pathways for the ions, also consistent with the possible tendency of alumina particles to aggregate (see Figure 3.6).

Interestingly, for the cases of MeO:MAPI and BPA:MAPI, the electronic and ionic conductivities of the films decreased by more than one order of magnitude compared to both MAPI and the A:MAPI films. This result already indicates that surface modification of the insulator has significant repercussions on the electrical properties of interfaces.

Further insights into the cause of such change in response are obtained by measuring the conductivities of the samples at higher iodine partial pressure conditions. Increasing the iodine partial pressure resulted in increasing of electronic conductivity for all samples, indicating that they all operate in a p-type electronic conduction

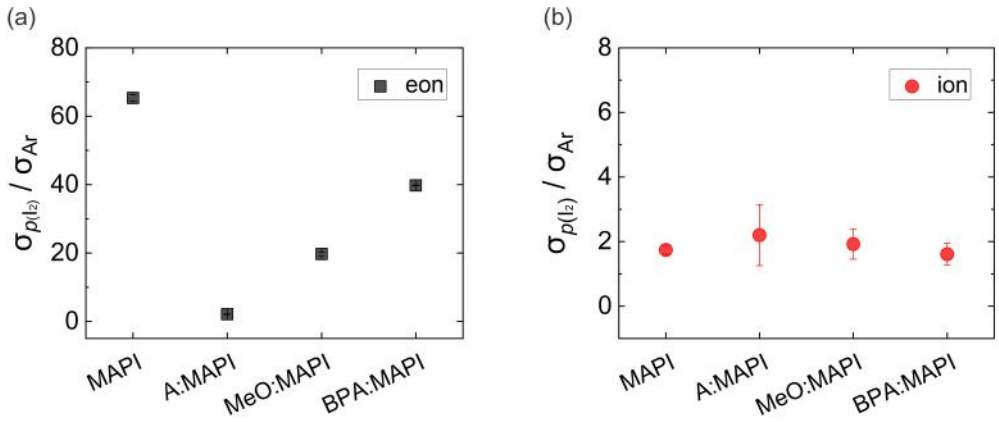

Figure 3.9: Electronic and ionic conductivity values compared Ar and $p(I_2) = 17$ nbar.

regime as based on their defect chemistry (see Chapter 1.1.2). On the other hand, in all cases, the ionic conductivity underwent a relatively smaller change with varying atmosphere. Values of the slope in the range of 0.03 to 0.21 were recorded for the ionic conductivity of samples with increasing iodine partial pressure.

To extract information on the space charge characteristics of these films, the electronic and ionic conductivities in both Ar and at a pressure of $p(I_2) = 17$ nbar are compared (Figure 3.9). In the case of MAPI, the electronic conductivity exhibited a change of approximately 60 times from Ar to $p(I_2)$, attributed to an increase in hole concentration in the bulk resulting from defect reactions involving the incorporation of iodine at the expense of an iodide vacancy, which give rise to an electron hole (see Chapter 1.1.2). Such trend is consistent with previous defect chemical studies of MAPI [33].

In contrast, for the A:MAPI composite, this change in electronic conductivity was lower than for the MAPI case by nearly 60 times. Such reduced increase in electronic conductivity on application of a high iodine partial pressure is due to the presence of an inversion space charge under argon conditions. This inversion space charge at the alumina and MAPI interface induces a large concentration of electrons within the space charge zone compared to the bulk's primary electronic charge carriers (in this case, electronic holes) in Ar. However, this inversion effect is expected to disappear when the iodine partial pressure is increased, increasing the hole concentration and

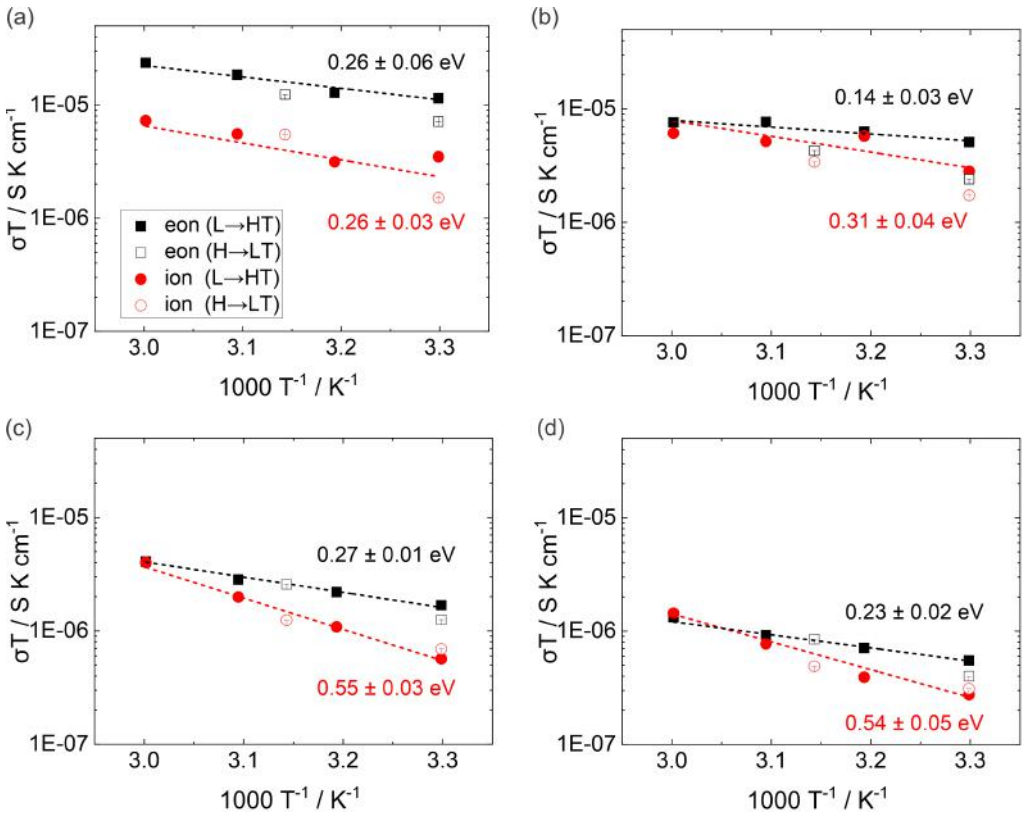

Figure 3.10: Electronic and ionic conductivity measurement results in fixed iodine partial pressure $p(I_2) = 17$ nbar and temparature from 30 to 60 °C of (a) MAPI, (b) A:MAPI, (c) MeO:MAPI and (d) BPA:MAPI films.

decreasing the electron concentration in the whole sample (including the interface).

In the MeO:MAPI and BPA:MAPI films, the electronic conductivity changed by a factor of approximately 20 and 40, respectively. This change is therefore in between the one recorded for MAPI and the one recorded for the A:MAPI sample. This observation can be attributed to a decreased space charge potential at the interface for the composite films that include surface modification. Therefore, consistently with the analysis of zeta potential results described above, such effect can be interpreted in terms of reduced ionic interaction between MAPI and the alumina particles due to the presence of the SAM. A similar analysis of the change in ionic conductivity between the argon situation and the measurement under $p(I_2) = 17$ nbar showed approximately the same value for all samples.

As the iodine partial pressure is increased further in the system, the inversion

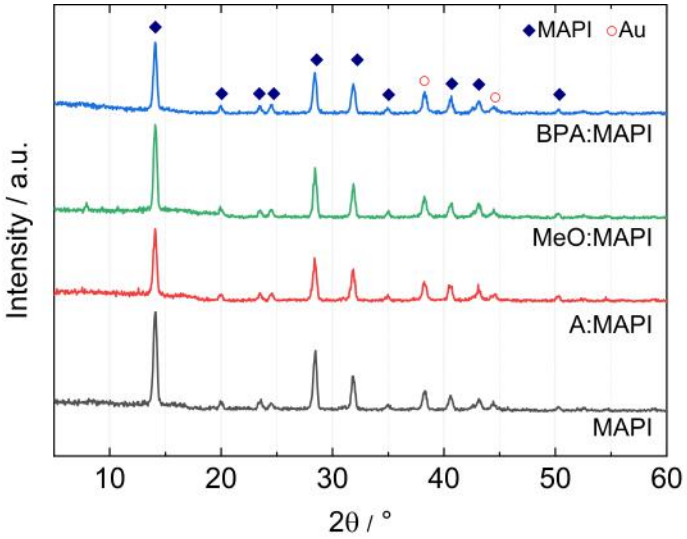

Figure 3.11: The XRD measurements of MAPI, A:MAPI, MeO:MAPI and BPA:MAPI after conductivity measurements of iodine partial pressure dependence and E_a (after 326 days from first XRD measurement Figure 3.5). All film showed clear MAPI tetragonal crystal phase without significant degradations.

regime due to the space charge present in the A:MAPI films is expected to disappear completely. Further details regarding changes in the space charge potential will be discussed in the next section (Chapter 3.1.3).

To verify the presence and the modulation of the interfacial space charge further, the E_a of each film was also measured under a fixed iodine partial pressure, $p(I_2) = 17$ nbar (Figure 3.10). In the case of MAPI, both the electronic and ionic conductivity exhibited an E_a of approximately 0.3 eV. The A:MAPI film displayed a reduced activation energy for electronic conductivity. This would be consistent with electrons being still partially responsible for the electronic conduction in the film even at this fixed $p(I_2)$ condition. On the other hand, the E_a for ionic conductivity remained relatively similar. This observation could be result of incomplete coverage of the MAPI grains by the alumina particles, allowing for ions to be transported through.

Regarding the MeO:MAPI and BPA:MAPI, both cases demonstrated an increased E_a for both electronic and ionic conduction compared to A:MAPI. This suggests the presence of a depletion layer for holes and iodide vacancies at the interface between the oxide (with molecules on the surface) and MAPI, and the absence of

any inversion effect.

All films showed good reversibility when $p(I_2)$ is lowered again, even though the final reversibility test in argon highlighted a conductivity value that was slightly lower than the original value under Ar. This suggests that there may be a slight degradation of MAPI after measurement at high temperatures (the range 30 - 60 °C is used). However, there was no clear PbI_2 peak in the XRD obtained after the measurement (Figure 3.11). Therefore, crystal phase is stable although there is minor degradation potentially.

3.1.3 Interpretation of conductivities and space charge formation

Based on the conductivity measurements of the films, the space charge potential at the various interfaces can be calculated considering a simplified model. Figure 3.12 shows a qualitative scheme including space charge formation at the interface between MAPI and alumina, and in the surface modified alumina case. As shown in this figure the variation in concentration of all defects in proximity of the alumina interface is reduced in presence of a molecule on surface.

To evaluate the value of the space charge potentials, different scenarios are considered based on the results above. According to such analysis, one can write for the measured electronic conductivity (σ_m) of accumulated charge carrier as

$$\sigma_m = \sigma_\infty + \beta_\ell \Psi_a \Omega_a \lambda \exp^{(Fd\phi)/RT} \frac{\sigma_{n\infty}}{\sqrt{(Fd\phi)/RT}} \tag{3.1}$$

where σ_∞ denotes bulk conductivity, Ψ_a the volume fraction, Ω_a surface-to-volume ratio of oxide particles and λ the space charge width [44, 82]. β_ℓ is associated to be 0.5 to indicating that particles enable partial percolation. Based on equation 3.1 and using measured electronic conductivity in argon condition, the bare alumina and MAPI interfaces exhibit a space charge potential of approximately 840 ± 90 mV, approximately consistent with previous estimates [82]. However, in the case of

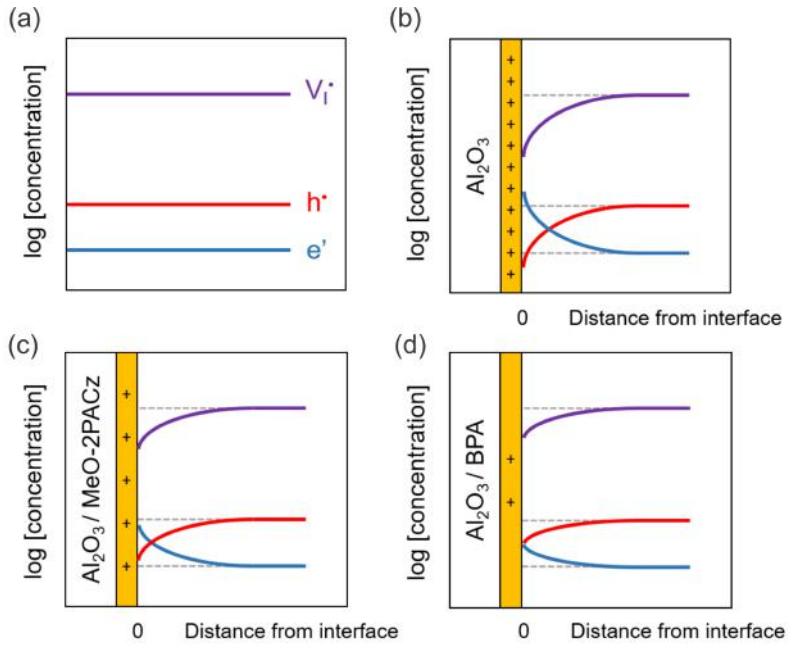

Figure 3.12: Scheme of charge carrier concentration at the interfaces between alumina and MAPI (A:MAPI, MeO:MAPI and BPA:MAPI) and MAPI bulk. Only significantly mobile charge carriers are presented.

MeO:MAPI, the space charge potential is reduced to approximately 740 ± 40 mV based on a similar analysis using the measured electronic conductivity under argon. This reduction can be attributed to the presence of organic molecules on the surface, which decreases the adsorption of Pb cations at the interface between alumina and MAPI, resulting in a smaller space charge potential.

Since in BPA:MAPI films showed depletion of charge carriers under argon measurement condition, equation 3.2 is applied to calculate space charge conductivity [82]. In this equation, the σ_m is evaluated as the series of the bulk (σ_∞) and the interfacial (σ_{SC}) contributions.

$$\sigma_m = \frac{1}{1/\sigma_\infty + 3\Psi_a(1/\sigma_{SC})} \tag{3.2}$$

The space charge conductivity σ_{SC} is calculated to be 2×10^{-12} S/cm.

3.1.4 Conclusions

The possibility to modulate the ionically-generated space charge potential at the interface between alumina and MAPI was investigated. A surface modification strategy was developed where organic molecules containing a phosphoric acid anchoring group were adsorbed on alumina, forming a chemical bond that is stable towards exposure to the solvent used for the perovskite precursor solution. Examination of the ionic interaction between bare alumina, MeO-2PACz, BPA surface-modified alumina, and MAPI through zeta potential and XPS measurements on the surface of alumina showed that the molecular sensitization successfully affects the whole oxide surface. When the alumina surface is covered with MeO-2PACz and BPA, the interaction between Pb cations and alumina is reduced compared to bare alumina.

The electrical response of composite films of bare and surface-modified alumina in MAPI, along with a pure MAPI film as control sample was investigated. The electronic and ionic conductivities were measured as a function of temperature and for different iodine partial pressures. The inclusion of alumina nanoparticles within MAPI resulted in an increased electronic conductivity at low iodine partial pressures consistent with a previous report. It is attributed to Pb cation adsorption on the surface of alumina and the formation of a space charge region where electronic conduction dominates the electrical response through the interfaces between MAPI and alumina. Such deviation from the behavior of MAPI tends to vanish for samples with surface modified alumina.

Based on these measurements, calculations of the space charge potential at the interface for the different composite films are carried out. Analysis of the conductivities using a brick-layer model resulted in an estimated for the space charge potential at the interface between alumina and MAPI of approximately 840 $\pm$ 90 mV. When MeO-2PACz is used to cover the alumina surface, the space charge potential is reduced to around 740 $\pm$ 40 mV (approximately 3 orders of magnitude change in each defect concentration at the interface compared with unmodified alumina). For

BPA the calculated space potential is 160 mV. The larger reduction in the space charge potential for the BPA case compared with MeO-2PACz is attributed to its smaller molecule size. By creating a more compact monolayer, BPA molecules allow the surface to be protected from ionic interactions to a larger extent.

The findings of this study suggest new tools for the design of devices that utilize MAPI, particularly in the context of all PSCs where interface engineering is commonly employed to enhance device performance. When employing surface modification techniques, it is crucial to consider not only how these molecules can alter the energy level alignment between materials, but also how they may selectively block or interact with specific mobile ionic defects, leading to modulation of the space charge potentials at the interfaces. Furthermore, it has implication for the design of molecules used as transporting molecular monolayer in that the size of molecule and density of the monolayer play an important role in determining the ionic interaction between halide perovskites and contact materials. Mastering such effects could ultimately contribute to the development of more efficient and stable halide perovskite based devices.

3.2 Effect of surface modified mesoporous films

In the previous chapter, the investigation of space charge modulation with organic molecules between alumina and MAPI has primarily focused on composite film configurations. While composite perovskite structure have been utilized in perovskite-based optoelectronic devices [102, 103], their application to state-of-the-art devices is limited.

Within solar cell devices, mesoporous structures are commonly employed. In such structures, the halide perovskite is infiltrated into a porous scaffold of charge transporting or insulating oxide (*e.g.* TiO_2, SnO_2 and ZrO_2). Of particular interest is the case of conductive oxides, such as mesoporous TiO_2 ($mTiO_2$). $mTiO_2$ has been extensively investigated in the field of dye-sensitized solar cells [104]. The utilization of $mTiO_2$ played a crucial role also in the initial breakthroughs of hybrid perovskite solar cells [105–107], and its continued implementation remains a promising approach for attaining devices with high PCE.

It is currently unclear whether the incorporation of mesoporous films in perovskite solar cells leads to high-performance devices primarily due to enhanced interfacial charge collection by enlarged surface area, or merely due to improved wetting and optimal film formation when processing the perovskite film from solution [108–110]. To answer this question, improved understanding of the role of interfaces in the charge carrier distribution and dynamics within halide perovskite in mesoporous structures is required. In particular, because mesoporous structures have such wide surface area, space charge formation is expected to have a significant impact on the behavior of charge carriers and on device performance. Additionally, when the pore size in these structures is small enough, interfacial effects on charge carrier redistribution becomes more significant, leading to completely different conduction properties compared to the bulk (Figure 3.13) [111]. This corresponding field is known as nanoionics [112]. This is especially likely for cases where Mott-Schottky situations are present, due to the relatively wide space charge regions forming in

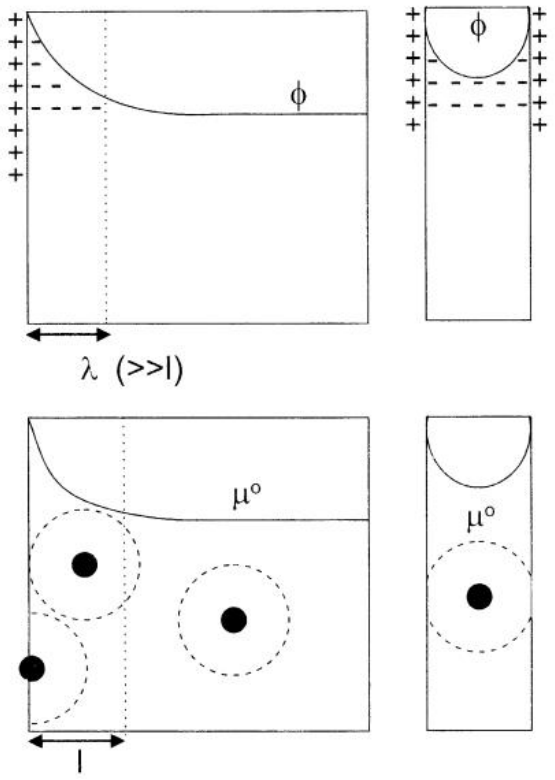

Figure 3.13: The effect of a space charge with width λ has very different consequences on the charge carrier redistributions depending on whether such width is (left) much narrower or (right) of comparable size with the characteristic size of the system (nanoionics regime) (resued with permission from reference [111]).

this case (see Chapter 1).

As shown in the introduction section, the current understanding of interfaces in halide perovskite devices, including the $mTiO_2$/halide perovskite structure, primarily revolves around electronic equilibrium [113, 114]. However, recent research conducted by Kim *et al.* [82] has presented evidence suggesting that, when MAPI is in contact with TiO_2, it exhibits similar interfacial ionic effects as for the case of alumina/MAPI (see Chapter 3.1). This observation implies that, at $mTiO_2$ interfaces, space charges may not be purely electronically-induced, but also ionic effects could play a role. The validation of this concept could potentially bring about a "paradigm shift" in the design of optoelectronic interfaces involving MAPI, and mixed conductors. By controlling the ionic properties of interfaces, a new parameter set could

be introduced, thereby enabling device optimization. Therefore, comprehending the space charge effects within porous structures is essential for revealing and controlling ionically-generated space charge formation and optimal charge carrier dynamics at the interfaces of halide perovskites.

In this chapter, the space charge at the MAPI interface with the electron transporting $mTiO_2$ is investigated. Initially, the film structure is optimized to measure conductivity exclusively in the MAPI infiltrated in the mesoporous region. The use of horizontal device structures for this electrical characterization requires processing the perovskite layer in a way that avoids the formation of a capping layer, which would otherwise affect the measurements.

Based on the electrical characterization of samples where MAPI is infiltrated in $mTiO_2$, the space charge behavior at the TiO_2/MAPI interface is discussed, including the possible relevance of nanoionic effects in this mesoscopic system (see Figure 3.13). Next, the surface of TiO_2 is modified using the organic molecules MeO-2PACz and BPA similarly to the previous chapter. This is done with the intention to modulate the ionic contribution to the space charge formation on the MAPI side of the interface. In the final part, I discuss the interpretation of the results, based on a simplified model of the mesoscopic system.

3.2.1 Film fabrication and surface modification

To assess the stability of MeO-2PACz and BPA on the surface of the $mTiO_2$ layer, FTIR analysis is conducted. The $mTiO_2$ layer is fabricated on a sapphire substrate using spin coating, based on the procedure outlined in Chapter 2. Following the fabrication of the $mTiO_2$ layer on the substrate, either of the MeO-2PACz or BPA molecules are applied onto the TiO_2 surface by immersing the substrate in a solution containing the relevant molecule. Subsequently, the substrates are washed with THF and DMSO and FTIR measurements are carried out within the glove box environment (see Methods section for details).

In the case of MeO-2PACz on $mTiO_2$, clear peaks corresponding to the organic

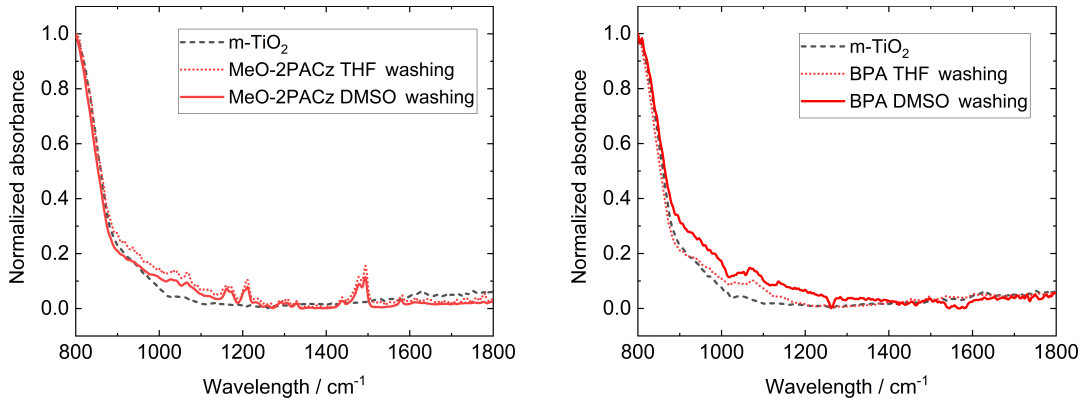

Figure 3.14: FTIR results of $mTiO_2$ surface with organic molecule following THF and DMSO washing.

molecules (C=C aromatic in plane stretching about 1490 cm^{-1} and C-N stretching at about 1250 cm^{-1}) are observed in the FTIR spectra after washing with THF and DMSO (Figure 3.14). In the case of BPA, although there was no significant increase in the intensity of the peak associated with the aromatic ring, a clear peak within the range of 900 - 1400 cm^{-1} related with phosphonic acid group is observed. This result confirms that the BPA is also successfully anchored to the surface of the TiO_2 and is expected to remain stable during the DMSO solution processing.

In order to ascertain that the contribution of MAPI only is detected through electrical conductivity experiments performed on horizontal devices structures, preliminary control experiments without the MAPI phase are conducted and compared with the electrical response of a MAPI film. To do this, MAPI, $mTiO_2$, and $mTiO_2$ films with surface modifications using MeO-2PACz and BPA are prepared on Au interdigitated electrodes. The electronic conductivity of these films are measured using DC galvanostatic polarization under argon at 40 °C, dark (appendix, Figure 3). Under argon conditions, the $mTiO_2$, surface-modified $mTiO_2$ layers with MeO-2PACz, and BPA exhibited electronic conductivities on the order of 10^{-13} - 10^{-11} S/cm, while MAPI displayed conductivity on the order of 5×10^{-10} S/cm (Table 3.1). Under a fixed $p(I_2)$, the conductivity of MAPI increases by almost two orders

Table 3.1: The measured conductivity of MAPI, $mTiO_2$, and $mTiO_2$ films with organic molecule surface modification (MeO-2PACz and BPA) under dark at 40 °C in Ar and $p(I_2)$ = 1.3 μbar (*MAPI in 0.2 μbar).

Film structure	σ_{eon} (Ar) S/cm	σ_{eon} $p(I_2)$ S/cm
MAPI	$(5.0 \pm 0.4) \times 10^{-10}$	$(1.1 \pm 0.2) \times 10^{-8}$
TiO_2	$(4.2 \pm 0.2) \times 10^{-11}$	$(2.3 \pm 0.1) \times 10^{-10}$
TiO_2/MeO-2PACz	$(2.5 \pm 0.1) \times 10^{-12}$	$(3.7 \pm 0.1) \times 10^{-11}$
TiO_2/BPA	$(5.6 \pm 0.1) \times 10^{-13}$	$(3.3 \pm 0.1) \times 10^{-13}$

of magnitude. The dependence of the conductivities for the control samples on $p(I_2)$ is consistent with oxidation of the electron conducting oxide (for the $mTiO_2$ case) or the molecular sensitizer (for the $mTiO_2$/MeO-2PACz case) by iodine. Very low conductivity and minor dependence on $p(I_2)$ is observed for the $mTiO_2$/BPA sample, possibly due to a lower photoinducex electron concentration due to the very large B_g of the molecule.

This analysis has two important implications. First, it sets a lower boundary to the conductivity values measured for the MAPI infiltrated $mTiO_2$ system that can be ascribed to the MAPI contribution, and for which the contribution of TiO_2 or of the molecular monolayer can be safely neglected [115]. Secondly, it shows that, in the presence of a capping layer of MAPI on top of the infiltrated layer into $mTiO_2$, the conductivity measurement in a horizontal configuration would be significantly influenced by transport in the MAPI capping layer. Therefore, it is necessary to make sure that a minimal capping layer forms during the preparation step. When adopting a standard MAPI fabrication procedure, however, a capping layer of significant thickness (in the order of 65 nm, see Figure 3.15) is obtained.

In order to reduce the thickness of the capping layer while maintaining the phase stability of MAPI, the concentration of the precursor solution is optimized to 0.75 M, and a mixed solvent of DMF/DMSO was used (detailed information is provided in Chapter 2). The optimized precursor solution was directly fabricated on an Au electrode and on $mTiO_2$ with and without surface modification (referred to as $mTiO_2$/MAPI, $mTiO_2$/MeO/MAPI and $mTiO_2$/BPA/MAPI).

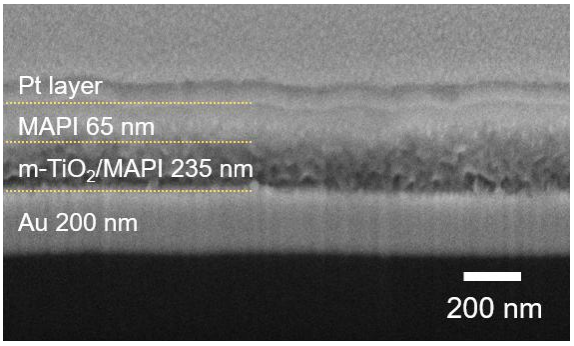

Figure 3.15: SEM cross section images of MAPI film that is infiltrated into $mTiO_2$ scaffold before film optimization. Approximately 65 nm of MAPI capping layer is placed on top of mesoporous layer. The film cross section is prepared with focused ion beam (FIB).

The SEM images in Figure 3.16 demonstrate the structure of the optimized films. The cross-section image reveals a uniform MAPI layer formed on the Au electrode, while the $mTiO_2$ films, also with surface-modified by MeO-2PACz and BPA, exhibit a porous layer of TiO_2 infiltrated with MAPI. SEM-EDX analysis is conducted to verify the penetration of MAPI into the porous TiO_2 layer (Figure 3.17). All samples, regardless of the surface modification of TiO_2, exhibited well-penetrated MAPI within the porous layer. An upper limit to the capping layer thickness of 20 nm is evaluated from the cross-section images. In the top-view SEM images, MAPI crystals are clearly visible, confirming the presence of a very thin capping layer.

The crystal structure of the samples was examined using XRD (Figure 3.18). The films exhibited peaks corresponding to the tetragonal structure of MAPI without significant PbI_2 peak. The MAPI film shows a small intensity PbI_2 peak beside a dominant signature from the MAPI tetragonal crystal structure.

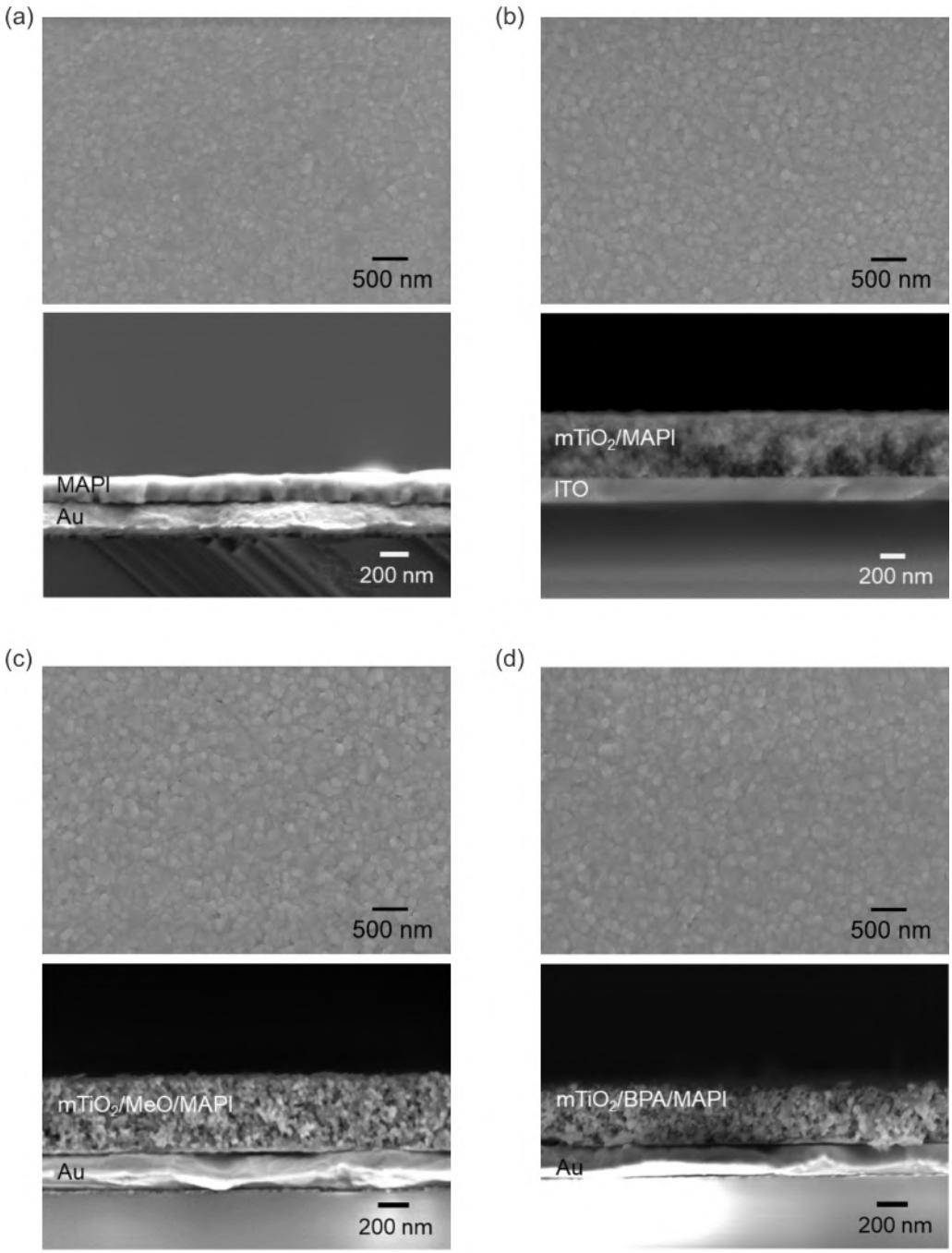

Figure 3.16: SEM images of the cross sections of the optimized mesoporous structure devices fabricated on both Au and ITO substrates. The use of an ITO substrate was implemented during the optimization process to mitigate the e-beam charging effect observed in SEM imaging.

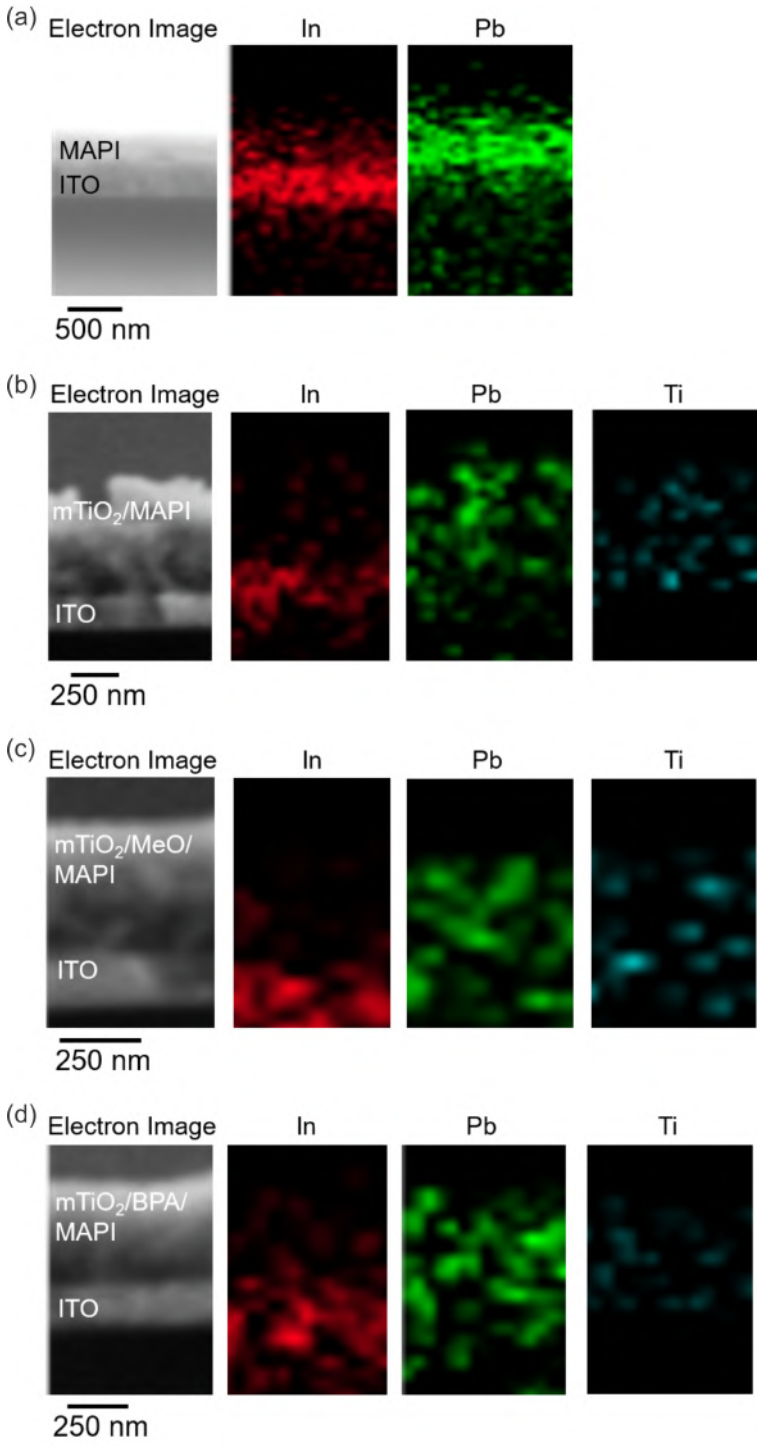

Figure 3.17: SEM-EDX images of the cross sections of the optimized mesoporous structure devices fabricated on ITO substrates.

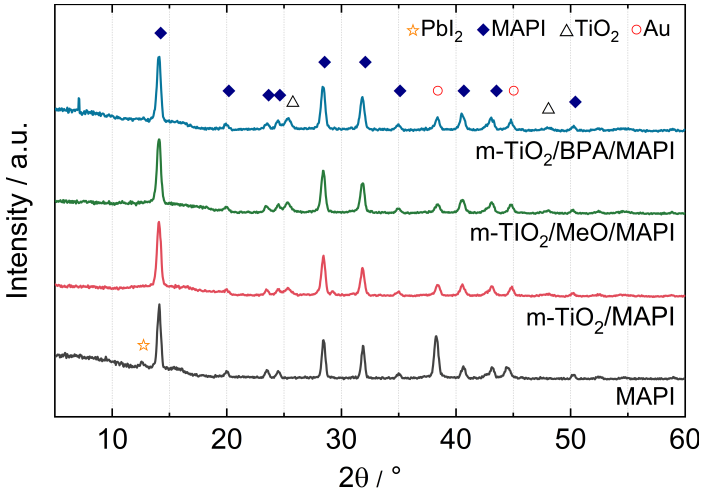

Figure 3.18: XRD spectra of MAPI, $mTiO_2$/MAPI, $mTiO_2$/MeO/MAPI and $mTiO_2$/BPA/MAPI films on Au electrode.

3.2.2 Results of electronic and ionic conductivity measurements

In order to investigate changes in the space charge potential of the different $mTiO_2$ surface modified films with MAPI, electronic and ionic conductivity measurements are conducted under Ar and different $p(I_2)$ conditions in the dark, using DC galvanostatic polarization and AC impedance.

Before examining the effects of $mTiO_2$ and surface modifications, it is necessary to evaluate the conductivity of a control sample (MAPI without $mTiO_2$) fabricated with the optimized recipe (0.75 M, DMF and DMSO mixed solvents). The measurement of such film is compared with that of a thicker perovskite layer fabricated using a 1.5 M MAPI in DMSO precursor solution, which is used as control sample in Chapter 3.1 (Figure 3.19).

In an argon environment, the ionic conductivity is very similar in the two films, while the electronic conductivity of the optimized MAPI layer is lower by approximately three-fold compared to the MAPI layer fabricated with a 1.5 M precursor solution. Interestingly, under controlled iodine partial pressure, such difference disappears. The difference observed in argon can therefore be ascribed to a slightly

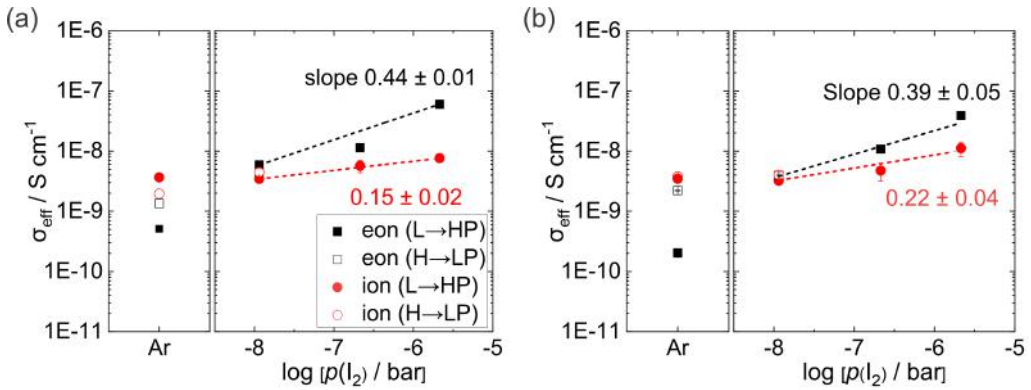

Figure 3.19: The results of electronic and ionic conductivity measurements on two types of MAPI films: (a) MAPI films fabricated using a 1.5 M precursor solution, as same as in Chapter 3.1 and (b) the optimized MAPI films specifically prepared for this study. In both cases, the films exhibited electronic and ionic conductivity in the range of 10^{-10} and 10^{-9} S/cm in an argon environment. Furthermore, both films displayed similar behavior in conductivity changes with varying iodine partial pressure.

different defect chemical situation under such non-fixed iodine partial pressure environments for the two samples. The mismatch could also be due to a slightly different contribution deriving from an inversion layer at the alumina/MAPI interface (see Chapter 3.1), possibly caused by changes in ionic interactions with the substrate for the two different fabrication procedures (*e.g.* different solvents and deposition procedures used). In either case, the fact that the conductivity under fixed iodine environment is similar indicates that the optimized procedure results in a MAPI film that is comparable with previous studies [82]. This is therefore used as control sample in the following.

The conductivities of $mTiO_2$/MAPI, $mTiO_2$/MeO/MAPI, and $mTiO_2$/BPA/MAPI are compared to the MAPI film. Figure 3.20 shows the impedance spectra collected for these samples under argon. The data indicate significant variations in the spectral shape, depending on the sample composition. When interpreting conductivity measurements in mesoporous structured devices, the morphology of the films must be taken into account. This is because the charge carriers flow through the infiltrated MAPI layer in the pores between oxide particles (Figure 3.21). Structure and morphology of the samples are of importance also when comparing the results with

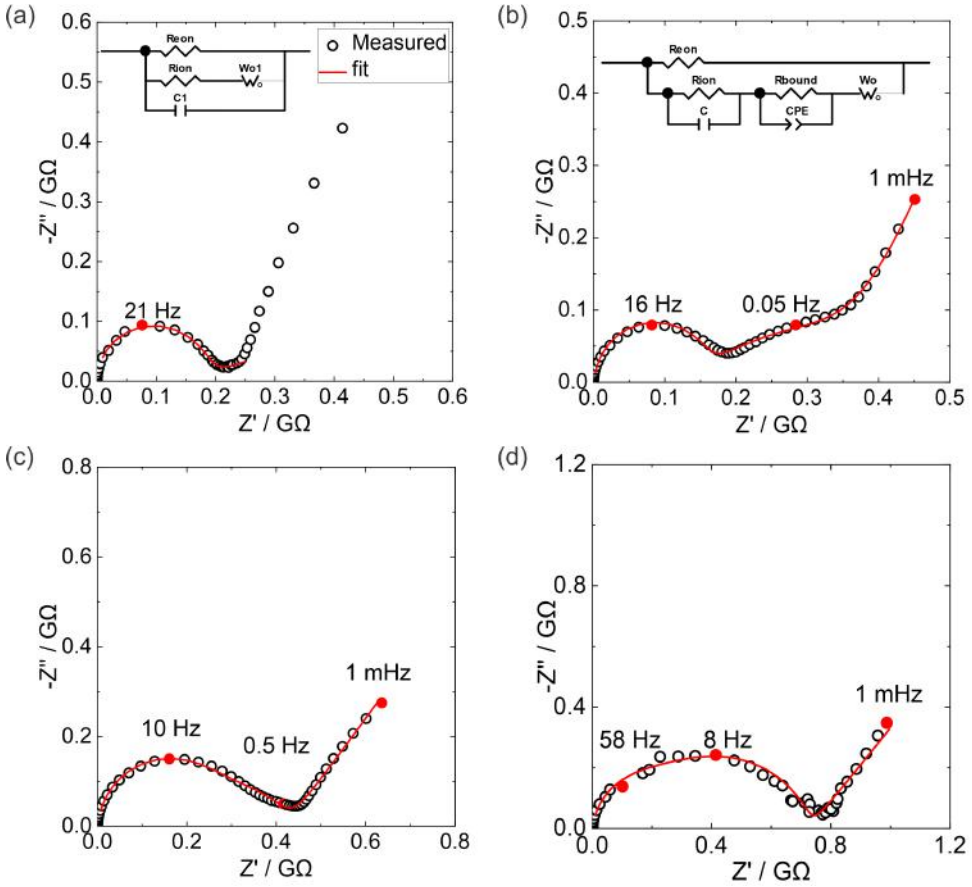

Figure 3.20: Equivalent circuit models,the AC impedance impedance spectra and fitting results for (a) MAPI and (b) $mTiO_2$/MAPI device. The impedance spectra of mesoporous structured device are fitted with same model used for (b). The AC impedance spectra and fitting result of (c) $mTiO_2$/MeO/MAPI and (d) $mTiO_2$/BPA/MAPI. Their results are obtained under Ar at 40 °C.

the composite samples investigated in literature [82] and in the previous chapter. Specifically, because the $mTiO_2$ film is deposited and sintered before the deposition of MAPI, the interface between MAPI and the $mTiO_2$ scaffold always presents percolation paths between the two electrodes. Therefore, the MAPI phase in the pores is also expected to percolate, connecting the two electrodes (note that this is not necessarily the case in a composite system). The consequence is that, (i) any carrier concentration enhancement occurring at the interface should always be visible in the measured conductivity. Also, it implies that (ii) a depleted carrier at the interface with $mTiO_2$ would not lead to a significant drop in its measured

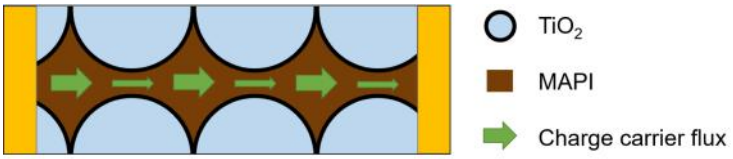

Figure 3.21: The scheme for morphological impacts on charge carrier transporting in the mesoporous devices.

conductivity, unless the depletion region is on the order of the pore size. Specifically, within the distribution of pore size in the $mTiO_2$, a large enough concentration of pores with sizes on the order of the depletion width can lead to a measurable effect in the samples electrical response. Evidence that this morphology effect may be relevant to the measured samples is given by the presence of an additional feature in the impedance measured for the mesoporous samples. Such feature is analyzed in the AC impedance fitting model using an additional resistor and constant phase element, referred to as R_{bound} and CPE (Figure 3.20 (b)). To assess the relationship between R_{bound} value and morphological impacts, the capacitance value is compared for each feature in impedance measurements. In impedance measurement of the mesoporous structured device, the capacitance from the first semicircle (C1 or C_g) exhibits an order of magnitude of 10^{-8} F/cm^2, which are associated with the geometrical capacitance (bulk of MAPI film and substrate). In contrast, the second feature yields a capacitance of 10^{-6} F/cm^2, which could be attributed to the morphological heterogeneity of the sample (constricting pores). The relevance of this point to the interpretation of the data is discussed below.

When considering the first feature only for the evaluation of the total conductivity, the ionic conductivity calculated in the $mTiO_2$/MAPI film is on the order of $\times 0.4$ lower than for the MAPI sample, a result that can be explained based on the volume fraction of MAPI infiltrated into the pores (appendix, Figure 4). This suggests that the first impedance feature may be dominated by the ionic conduction in the pores that are large enough to exhibit a behavior close to the bulk case.

In the case of $mTiO_2$/MAPI film, the electronic conductivity decreased according to a factor of 0.67 compared with the MAPI-only film. As above, this could potentially

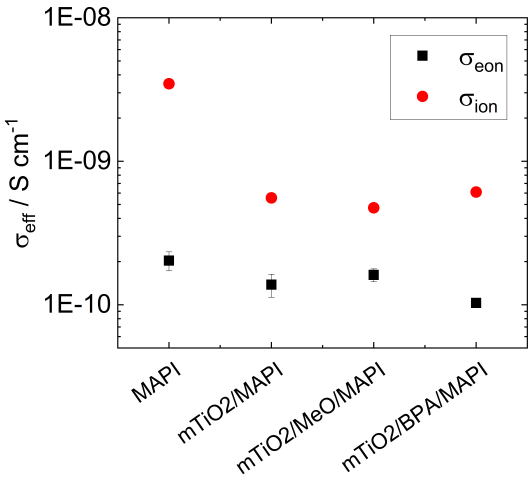

Figure 3.22: Comparison of electronic and ionic conductivities of MAPI, $mTiO_2$/MAPI, $mTiO_2$/MeO/MAPI and $mTiO_2$/BPA/MAPI in argon at 40 °C.

be explained considering the expected porosity of mesoporous TiO_2. However, a different picture arises if one considers the ionic conductivity evaluated from the total conductivity including the high frequency and the mid-frequency feature. Such ionic conductivity decreased by an order of magnitude in the $mTiO_2$/MAPI sample compared to MAPI under Ar conditions (Figure 3.22). This decrease is interpreted here as resulting from the large concentration of narrow pores in the sample that induce either significant current constriction effects, or even depletion of the local ionic defect concentration. Such resistance is not visible at high frequencies, where ions mostly migrate within the large pores, but become evident at intermediate frequencies.

Assuming that the ionic behavior is dominated by positively charged iodide vacancies, a similar depletion effect is expected to influence the electron holes in the pores and should affect the electronic conductivity to a similar extent. As mentioned above, however, the experimental observation indicates a mild drop in the electronic conductivity in the mesoporous system. Such a value that is larger than expected is explained when considering the formation of an inversion space charge on the MAPI side at the interface between TiO_2 and MAPI. Indeed, in such a space charge situation, the concentration of iodide vacancies and electron holes on the MAPI side

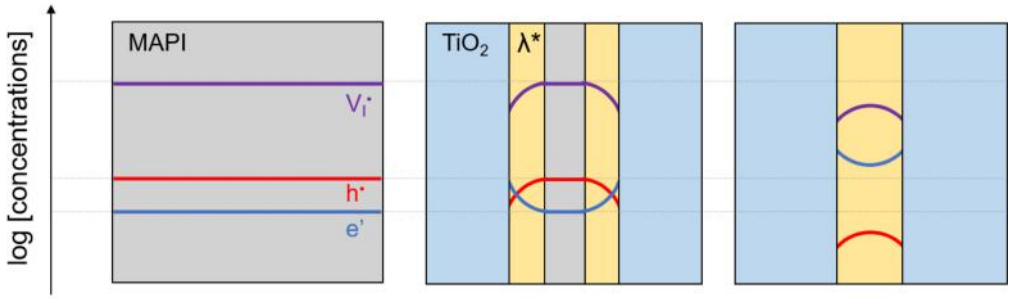

Figure 3.23: Scheme of charge carrier concentration changes depends on space charge width (λ^*) in mesoporous structure (color code: grey MAPI; blue TiO_2; yellow space charge region within MAPI).

decreases, while the electron concentration increases within the space charge zone at the mTiO_2/MAPI interface. As a result, interfacial electron conduction contributes to the electronic conductivity, leading to a smaller decrease in electronic conductivity compared to the ionic conductivity when comparing MAPI in mTiO_2 with the MAPI control.

To summarize:

(i) the ionic conductivity drop in the mTiO_2/MAPI sample compared with MAPI could be attribute to the presence of small pores constricting the long range (pore-to-pore) transport of ionic defects and to potential nanoionic effects.

(ii) the mild electronic conductivity decrease is a combined effect of volume fraction and (inversion) space charge contributions (see discussion in Chapter 3.3.3).

In order to obtain detailed information on which charge carrier is contributing to the electronic conductivity and on the region of ionic redistribution within the pores (see Figure 3.23), the iodine partial pressure dependence of the partial conductivities is measured (Figure 3.24) in the range of $p(I_2)$ between 12 nbar to 2 μbar. The MAPI film shows increasing electronic conductivity when the atmosphere is changed from Ar to 12 nbar of iodine gas pressure, with further increase when $p(I_2)$ is increased up to 2 μbar. This is consistent with the electron hole concentration increasing on iodine incorporation at high $p(I_2)$. On the other hand, the ionic conductivity is not changed significantly by varying the $p(I_2)$. Based on this result, it can be concluded

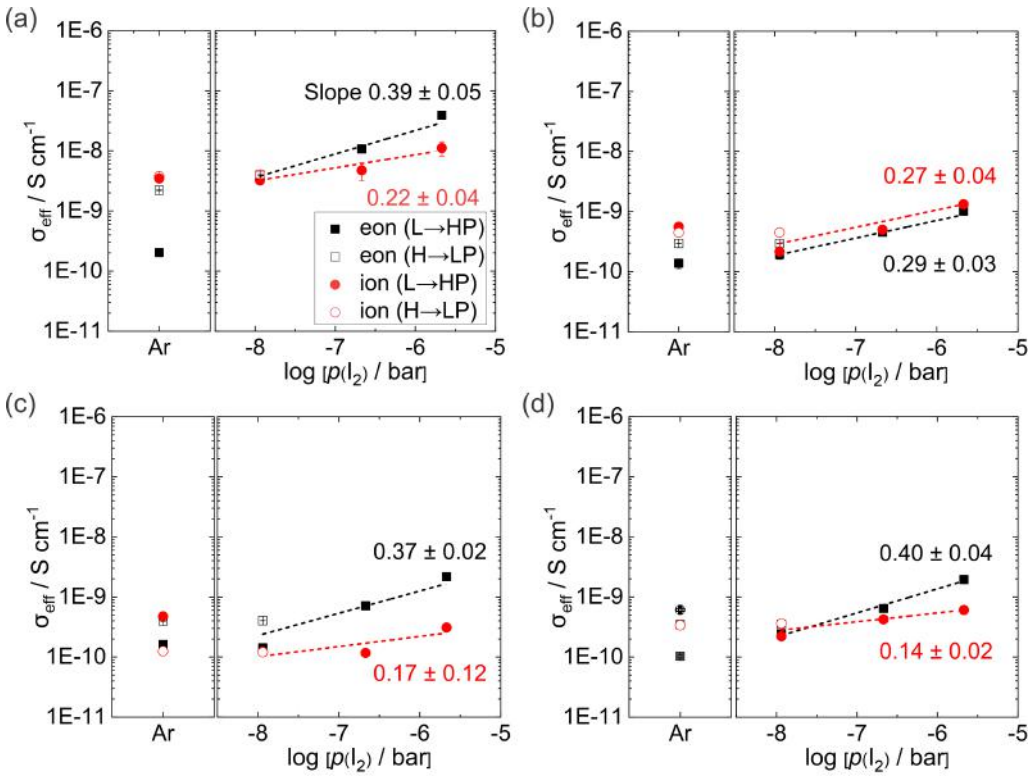

Figure 3.24: The results of electronic and ionic conductivity measurements on different films, including (a) MAPI, (b) $mTiO_2$/MAPI, (c) $mTiO_2$/MeO/MAPI, and (d) $mTiO_2$/BPA/MAPI. Irrespective of the film morphology, all films exhibited electronic conductivities are on orders of 10^{-10} S/cm in an argon environment. The $p(I_2)$ was varied from 12 nbar to 2 μbar. Additionally, the reversibility of the conductivity was examined (empty symbols) under both $p(I_2)$ = 12 nbar and argon conditions.

that MAPI shows mainly p-type electronic conduction and that it operates in the intrinsic regime under the specified conditions. Also, based on the slope of electronic conductivity in different iodine partial pressure, the iodine partial pressure in Ar measurement conditions is expected to be in the order of 10 pbar.

In the $mTiO_2$/MAPI sample, a positive slope for the electronic conductivity vs. $p(I_2)$ indicates p-type conduction in this iodine partial pressure regime. Importantly, under argon conditions, the electronic conductivity is very similar to the value measured under $p(I_2)$=12 nbar. This observation confirms the above hypothesis, whereby electrons are significantly contributing to the electronic conduction at very low $p(I_2)$ (argon) through an inversion space charge effect (Figure 3.24). Consis-

tently, a slightly lower slope for the electronic conductivity vs. $p(I_2)$ is also observed for the $mTiO_2$/MAPI sample compared with MAPI. The samples where the $mTiO_2$ is modified with either MeO-2PACz or BPA molecule show similar behavior to the unmodified samples.

The positive slope for the $p(I_2)$ dependence of the ionic conductivity in these samples is not expected. In MAPI, this can be because of (1) oxygen effects (2) large error in the conductivity estimate at high iodine partial pressure at $p(I_2)$ of 2 μbar. Regarding (1), MAPI films are fabricated under argon condition, and the samples were mounted into the measuring cell within glove box environment. Furthermore, the oxygen partial pressure within cell during the measurement was estimated to be < 10 ppm in this case. Under these conditions and based on previous studies on this question, oxygen effects should be negligible. As for (2), since the electronic conductivity is larger than the ionic conductivity at high iodine partial pressure, there could be a large calculation error while extracting ionic conductivity from total conductivity ($\sigma_{tot} = \sigma_{eon} + \sigma_{ion}$). Indeed, at $p(I_2)$ lower than 2 μbar, the ionic conductivity shows almost flat profile. In the device using a $mTiO_2$ scaffold a positive slope of ionic conduction at fixed iodine partial pressure is also observed. Besides the above explanations, in this case additional uncertainty due to electronic contribution to the mid-frequency feature could influence the evaluation and separation of the ionic conductivity and lead to potential interference of the electronic conductivity vs. $p(I_2)$ slope in the ionic conductivity trend.

In order to discuss the origin of the observed space charge behavior at the $mTiO_2$/MAPI interface, the ratio between the ionic or electronic conductivity measured under fixed $p(I_2)$ and measured in argon is evaluated for all samples (Figure 3.25).

The electronic conductivity changes significantly from Ar to $p(I_2)$ in the MAPI case, but not as much in the mesoporous structures. In particular, the sample MeO-2PACz shows the same change in conductivity (within error) with the $mTiO_2$/MAPI sample, while for the BPA case, a slightly larger change is observed. These data provide evidence that: (i) the inversion effect discussed above occurs in $mTiO_2$/MAPI

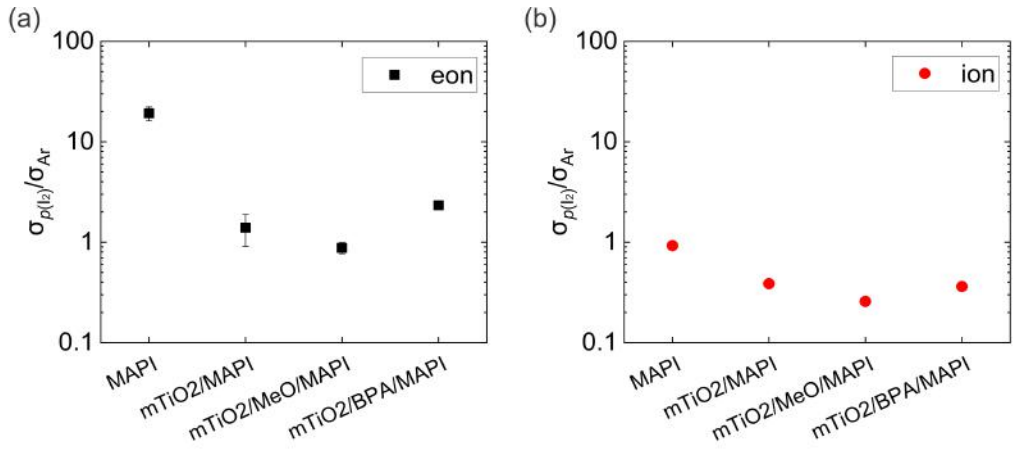

Figure 3.25: Comparison of (a) electronic and (b) ionic conductivities of MAPI and mesoporous structured films measured in $p(I_2) = 12$ nbar and under argon condition.

sample; (ii) surface modification with molecules of the TiO_2 surface does not significantly change such behavior. The latter point could be evidence that, because TiO_2 is an electronic conductor, electronic equilibration at the $mTiO_2$/MAPI interface is dominant, compared to ionic adsorption effects. However, it is challenging to prove that the molecules on the surface of TiO_2 do in fact completely block ion adsorption. The slightly larger value of $\sigma_{p(I2)}/\sigma_{Ar}$ observed for the BPA molecule, which might form a more compact monolayer compared with the MeO-2PACz case, shows a trend that could be consistent with the varying ability to block ion adsorption depending on molecule size (see also Chapter 3.1). Also, the negligible change in behavior on sensitization of the $mTiO_2$ with MeO-2PACz points towards limited influence of the change in pore size due to the adsorbed molecule. In order to validate the significance of the observed change in electronic conductivity across samples, the change in ionic conductivity is also shown (Figure 3.25), for which the changes among all films are very small, as expected.

3.2.3 Interpretation of electronic and ionic conductivities

Based on the measured ionic conductivity of MAPI, $mTiO_2$/MAPI, $mTiO_2$/MeO/MAPI and $mTiO_2$/BPA/MAPI films in argon (Section 3.3.2), the expected space charge

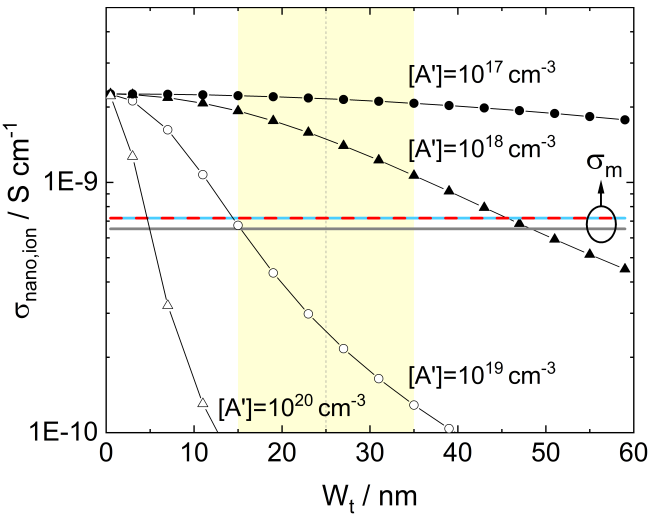

Figure 3.26: Calculated ionic conductivity of MAPI in mesoporous systems as function of W_t for different [A′]. The calculation assumes $2W_d$=W_t in order to predict the conductivity value when the nanoionics regime becomes active. The measured ionic conductivities for $mTiO_2$/MAPI (red dash line), $mTiO_2$/MeO/MAPI (blue solid line) and $mTiO_2$/BPA/MAPI (gray solid line) are showed as σ_m. The yellow area indicates an estimated range of pore size in the $mTiO_2$ film used in this study.

width in the mesoporous structure is calculated. A very rough evaluation contemplates the quantification of the 'bulk' within the pores that contributes to the ion conduction with a value of conductivity $\sigma_{bulk,ion}$ (measured for the MAPI case). By neglecting the contribution of the depletion space charges and by considering a simplified cylindrical symmetry of the pore, one can write for the measured ionic conductivity ($\sigma_{m,ion}$) :

$$\sigma_{m,ion} = \sigma_{bulk,ion} \times P_t \times \frac{(W_t - 2W_d)^2}{W_t^2} \times \frac{1}{\delta\tau} \tag{3.3}$$

where P_t denotes porosity, W_t diameter of pore, W_d space charge width in the MAPI on the surface of the TiO_2, $\delta\tau$ constrictivity and tortuosity.

Figure 3.26 shows $\sigma_{nano,ion}$ as function of W_t for different [A′] (concentration of acceptor dopants) compared to measured ionic conductivities in the samples described above. When a pore size of 25 nm is considered, the measured ionic conductivities in the mesoporous structure devices are lower than $\sigma_{nano,ion}$ for [A′] = 10^{18} cm^{-3}

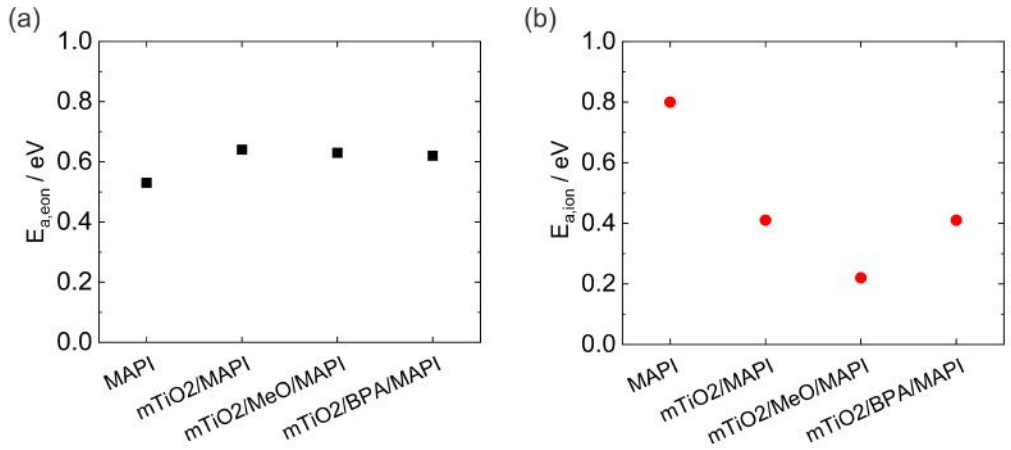

Figure 3.27: Results of (a) electronic and (b) ionic E_a measurements of MAPI, $mTiO_2$/MAPI, $mTiO_2$/MeO/MAPI and $mTiO_2$/BPA/MAPI films.

condition. This would indicate that the conductivity of these samples are limited by regions that operate in the nanoionic regime. When considering higher dopant concentrations (*e.g.* $[A'] = 10^{19}$ cm^{-3}), $\sigma_{nano,ion}$ is smaller than measured ionic conductivity, suggesting that the latter value can be due to conduction through percolating pores that are not fully depleted. However, one needs to consider the distribution of pore sizes in the system. It is possible that, for example, conduction through larger but also smaller pore size than 25 nm is required for percolation. Even when considering $[A'] = 10^{19}$ cm^{-3}, contribution from pores in the nanoionic regime cannot be excluded.

The measured conductivity, and in particular the presence of a mid-frequency feature in the impedance spectra of the devices containing $mTiO_2$, is likely to be a combined effect of constriction and of (partial) nanoionic regime. For the case of $mTiO_2$/MeO/MAPI and $mTiO_2$/BPA/MAPI samples also showed similar electrical behavior in this frequency range. The actual pore size in these samples could be smaller than $mTiO_2$/MAPI sample because of the molecules' presence on the oxide surfaces although, as mentioned above, this may not be a significant effect.

Additional insights into the role of nanoionic effects can be obtained from E_a measurement of the conductivities. The electronic and ionic activation energies are measured under fixed iodine partial pressure ($p(I_2) = 11.5$ nbar) (Figure 3.27). All

mesoporous structures show an E_a for the electronic conductivity on the order of 0.62-0.64 eV. This value is slightly larger compared with MAPI (0.53 eV). This result would point to the presence of significant depletion in most percolating pathways, and therefore to nanoionic effects being of relevance. However, E_a of ionic carriers in case of mesoporous films are decreased (0.2-0.4 eV) compared with MAPI (0.8 eV), a result that cannot be explained based on the proposed model.

3.2.4 Conclusions

This study investigated the nanoionic effects and the mixed ionic-electronic conducting properties of mesoporous structures as well as the impact of surface modification on the ionic interaction at the interface between TiO_2 and MAPI. The fabrication of $mTiO_2$ and subsequent surface modification were optimized to obtain samples where conduction in MAPI within the pores of the mesoporous scaffold is accessible.

The electrical response of mesoporous films, including bare and surface-modified $mTiO_2$ with infiltrated MAPI, as well as a control sample of MAPI thin film, was examined. The electronic and ionic conductivities were measured at various temperatures and under different iodine partial pressures.

The trend in electronic conductivities indicates the presence of a space charge region at the interface between TiO_2 and MAPI that induces an inversion layer where electrons become majority carriers. The decrease in ionic conductivity observed upon infiltrating MAPI into the $mTiO_2$ layer, was ascribed to a combined effect of current constriction and the presence of pores where the nanoionic regime (complete depletion of iodide vacancies) is reached. Assuming a pore size of 25 nm and $[A'] = 10^{18}$ cm^{-3} for $mTiO_2$/MAPI, $mTiO_2$/MeO/MAPI and $mTiO_2$/BPA/MAPI samples, such regime could be confirmed from a simplified model. E_a of electronic conductivity seems to support such trend. On the other hand a decrease in the E_a of the ionic conductivity is observed for the mesoporous samples, which could not be explained on the basis of the proposed model and requires additional investigations.

Based on the findings of this study, understanding of nanoionic effects is essential in order to comprehend the space charge behavior within mesoporous structures of halide perovskite-based devices. Furthermore, the data showed that heterogeneous doping due to the oxide is not influenced by surface modification of conductive TiO_2 to the same extent as it is for alumina.

3.3 Impacts of ionically generated space charges on MAPI in perovskite solar cells

This chapter presents the study of solar cell devices in the context of the interfacial effects discussed in chapters 3.1 and 3.2. The use of oxide:MAPI composite films as active layer of solar cells is explored, in order to verify the effect of space charge regions and, potentially, distributed p-n junctions within the active layer of the device. Secondly, the role of interfacial effects in MAPI infiltrated in mTiO_2 is studied, in relation to their influence on charge carrier redistribution and nanoionic effects.

In the previous chapters, electrical measurements on horizontal device structures have been presented. While such architecture is convenient for a careful characterization of mixed conducting properties of hybrid perovskites, most optoelectronic devices of relevance to the field of this class of materials are based on a vertical architecture (see Chapter 1). Therefore, the electrical properties in a vertical device structure need to be discussed, also in order to analyze the performance of solar cells that include composite and mesoporous structures.

Firstly, the role of the contact layers in the measurement of the electrical response of vertical structures needs to be addressed. In horizontal devices, metal electrodes can be deposited on the substrate before the deposition of the perovskite, allowing one to fabricate devices where highly conductive electrodes are connecting the active material to the measuring setup. In vertical devices, limitations in the processing conditions need to be taken into account, implying that at least one of the contacts is deposited on top of perovskite layer. Such restriction raises questions regarding the analysis of the conductivity measurement on such devices. It is important to clarify potential contributions of the contact material to the overall conductivity of the device. Importantly, the conductivity may differ when the contact material is investigated separately from the active material, in that space charges at the

interface due to specific interactions could have a major influence on the vertical resistance of the hole or the electron transport layer. More in general, the contact with the hybrid perovskite, which is a mixed ionic-electronic conductor, requires understanding of the electronic, but also the ionic equilibration between the two phases. The latter may involve ion adsorption effects, but also ionic exchange between the materials [116, 117]. Such question is tested here for the most commonly used hole transport material (HTM), 2,2′,7,7′-Tetrakis[N,N-di(4-methoxyphenyl)amino]-9,9′-spirobifluorene (Spiro-OMeTAD). The implication of the iodine partial pressure dependence of this HTM conductivity are discussed.

Next, the electrical characterization of vertical solar cell devices, following a similar procedure as the one used in the previous chapters, is presented. Here, the focus is clarifying the interpretation of DC and AC experiments that can be performed on solar cells, in order to extract estimates of the ionic and electronic conductivities in the perovskites. The role of the preparation conditions and of the contact layers choice is discussed.

Based on such analysis of solar cells containing oxide nanoparticles and mTiO_2 contact, the space charge effects investigated in the previous chapters are confirmed also in the vertical structures. Finally, the solar cells' performance are presented and the influence of the interfacial effects, based on the comparison between devices with either surface modified or unmodified oxides, are discussed in detail.

3.3.1 Iodine diffusion into organic contacting layer

This study investigates the nanoionic effects and the mixed ionic-electronic conducting properties of mesoporous structures as well as the impact of surface modification on the ionic interaction at the interface between TiO_2 and MAPI. The fabrication of mTiO_2 and subsequent surface modification were optimized to obtain samples where conduction can occur in infiltrated MAPI.

The structure of hybrid perovskite solar cells commonly involves the contact of a halide perovskite layer with one or more organic semiconducting layers. For exam-

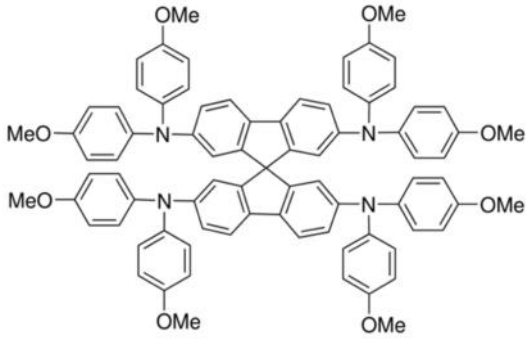

Figure 3.28: The molecular structure of Spiro-OMeTAD which is used in this chapter as hole transporting organic layer in solar cell devices.

ple Spiro-OMeTAD, poly[bis(4-phenyl)(2,4,6-trimethylphenyl)amine] (PTAA), and Poly(2,3-dihydrothieno-1,4-dioxin)-poly(styrenesulfonate) (PEDOT:PSS) are among the most used HTMs in the field significant. Iodine diffusion into organic layers has been demonstrated when these materials are exposed to iodine vapor, but also as a result of illumination of hybrid perovskite layer in contact with the HTM [118, 119]. Such results suggest that: (i) the properties of these organic semiconductors can be changed on exposure to different iodine partial pressures; (ii) more interestingly, the effective partial pressure provided by the halide perovskite, such as MAPI, could modify the property of the contact material, already after deposition.

This section focuses on examining the conductivity of organic layer at varying iodine partial pressures in order to gain insight into how it influences the conductivity analysis of MAPI within the solar cell structures. The results will be then discussed in relation to the expected doping effect of contacting an HTM with MAPI. The hole transporting material spiro-OMeTAD (Figure 3.28) will be investigated here and used also in the following sections in the study of vertical devices.

Spiro-OMeTAD layers are prepared with and without doping, as described in Chapter 2. Two commonly used dopants for Spiro-OMeTAD in solar cell fabrication, namely LiTFSI and tBP, are employed. LiTFSI is added as a p-dopant to enhance the hole conductivity of Spiro-OMeTAD, while tBP is used to improve the morphology [120–122]. The conductivity of these films is assessed under argon and under

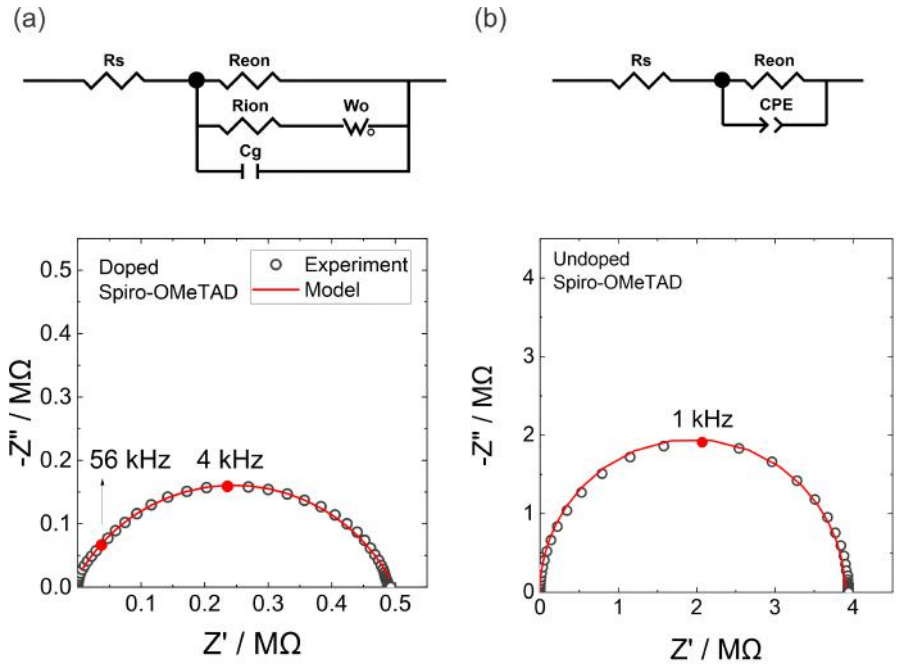

Figure 3.29: AC impedance measurements of (a) doped and (b) undoped spiro-OMeTAD in Ar. The spectra in different $p(I_2)$ are showed in Figure 5 and 6 (Appendix).

different iodine partial pressures by AC impedance measurement. The measured AC spectra and equivalent circuits used for the analysis are shown in Figure 3.29, 5 and 6 in appendix. Interestingly, the doped spiro-OMeTAD showed two features in the impedance spectra, while the undoped sample's response is well approximated by a single semicircle in the Nyquist plot. One possible explanation for such behavior is that, due to the strong doping, an interfacial depletion layer close to the Au contacts is induced. Contribution from ionic species resulting from the dopants could also be involved in the high frequency response. In the analysis that follows, the electronic resistance (R_{eon}) measured at low frequencies is extracted.

The electronic conductivity of the film is shown in Figure 3.30 for doped spiro-OMeTAD (see Figure 7 for undoped spiro-OMeTAD results in appendix). This film shows approximately an order of magnitude larger conductivity value than the undoped film within the entire $p(I_2)$ range probed in the experiment. Both films show an increase in conductivity when $p(I_2)$ is increased. A slope on this graph close to 0.5 also suggests iodine doping of the HTM according to

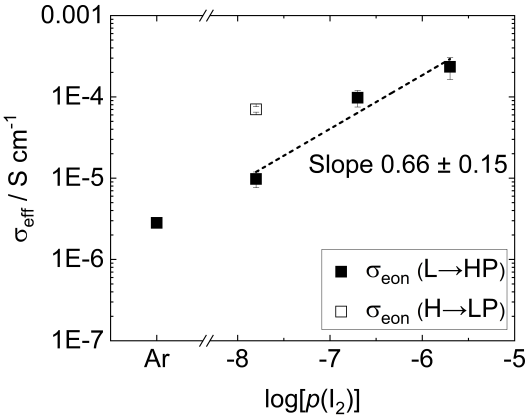

Figure 3.30: The electronic conductivity of doped spiro-OMeTAD in argon and different $p(I_2)$.

$$Spiro - OMeTAD + \frac{1}{2}I_2 \rightarrow Spiro - OMeTAD^+ + I^- \tag{3.4}$$

Interestingly, when the film of doped spiro-OMeTAD is measured under low $p(I_2)$ again after the $p(I_2)$ measurement scan, the conductivity showed only partial reversibility. This indicates that the oxidation of spiro-OMeTAD by iodine is a very favorable reaction, also consistent with the relatively high lying HOMO of this molecule [119]. As a result, when spiro-OMeTAD is in contact with MAPI, the iodine chemical equilibrium between these material can, depending on the initial doping of the film, induce further doping and increased conductivity in the HTM compared to the case before contact. Furthermore, such enhancement, which could be more pronounced after the device is exposed to light and MAPI may tend to excorporate iodine [123], is largely irreversible.

Another important observation is that the doped Sprio-OMeTAD shows conductivities in the order of 10^{-6} - 10^{-4} S/cm in the probed range of $p(I_2)$. Based on the values of conductivity expected for MAPI and on the fact that the perovskite thickness is generally greater the HTM film thickness, one can expect that MAPI dominates the measured resistance in vertical device configuration (solar cell structure) under dark and close to equilibrium. This points towards the opportunity to quantify partial conductivities of the hybrid perovskite within solar cell structures.

3.3.2 Conductivity measurements: horizontal device vs. solar cell device

This section aims to compare the properties of horizontal devices (MAPI deposited on interdigitated electrodes on sapphire substrate) and vertical devices (solar cell structure as well as single carrier devices). The use of different contact layer configurations is explored to emphasize the role of interfacial resistances and recombination resistances in the evaluation of the electronic conductivity in the perovskite.

Another important point to consider when investigating partial conductivities of halide perovskites within solar cells, is that such devices are often fabricated under inert gas conditions, but occasionally also in air or under controlled moisture conditions. Such differences in preparation conditions are expected to have major impact on the equilibrium defect chemistry of the mixed conductor.

To show the importance of these points, the electrical properties of an horizontal device with a MAPI film fabricated under argon (MAPI (H)) are compared with a solar cell device (MAPI (V)) fabricated using a standard procedure under dry air. The solar cell structure here is FTO/cTiO_2/mTiO_2 (145 nm)/MAPI/spiro-OMeTAD/Au. A detailed sample preparation procedure can be found in Chapter 2. The comparison between these films fabricated with different structures and under different atmospheres emphasizes the importance of these factors in the determination of the electrical properties of MAPI-based devices.

In Figure 3.31 (a) the MAPI (H) exhibits a significantly larger electronic conductivity compared with MAPI (V) (more than two orders of magnitude difference). Since MAPI (V) is fabricated in dry Air atmosphere, it is expected to have higher conductivities compared to the device that is fabricated under argon conditions. This is because oxygen doping affects the concentration of electronic charge carriers. Senocrate *et al.*, showed the role of oxygen doping in MAPI under controlled oxygen partial pressure. The result clearly shows that oxygen increases electronic conductivity of MAPI under dark (see Figure 3.31(b)), possibly due to the reaction

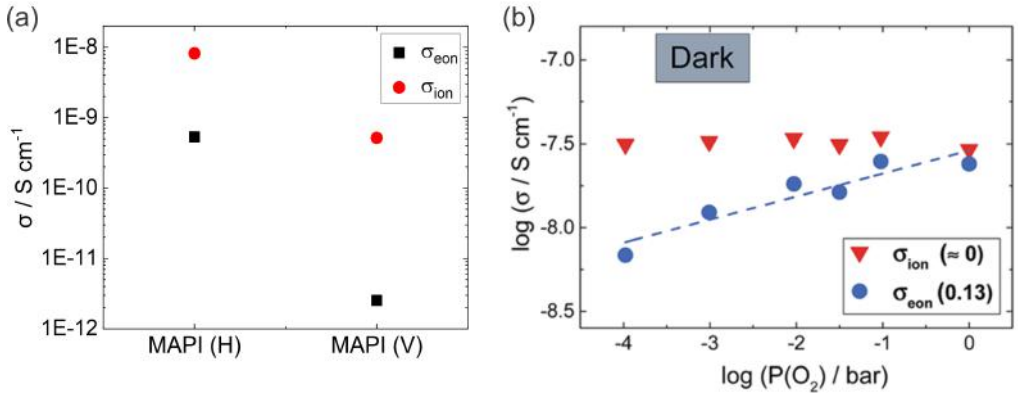

Figure 3.31: (a) The electronic conductivity of MAPI film in horizontal configuration fabricated under argon atmosphere (MAPI (H)) and MAPI solar cell device (MAPI (V)). (b) Electronic and ionic conductivity changes in different oxygen partial pressure ($p(O_2)$) in horizontal configuration (reproduced from reference [124]).

$$V_I^{\bullet} + \frac{1}{2}O_2 \rightleftarrows 2h^{\bullet} + O_i' \tag{3.5}$$

In the results shown in Figure 3.31 (a), this trend is not visible. Such apparent contradiction is likely due to the difference in the contact configuration in the two devices. While in the MAPI (H) device Au contacts allowing for effective hole injection and extraction are used, in the MAPI (V) device asymmetrical contacts with either selective hole blocking or electron blocking properties are used. This means that recombination of electrons and holes is needed in the bulk of MAPI or at the interfaces with the contacts to maintain a steady-state electronic current through the device. If the resulting charge recombination resistance is larger than the electronic transport resistance through the bulk of MAPI, the results in Figure 3.31 (a) can be explained.

To test this hypothesis, hole and electron only devices (HOD and EOD) are fabricated through the same process described above (under dry air conditions). The device structure of HOD is ITO/PEDOT:PSS/MAPI/spiro-OMeTAD/Au and EOD is ITO/SnO_2/MAPI/PCBM/Au. These devices include contacts that are either good hole injecting/extracting materials (HOD) or good electron injecting/extract-

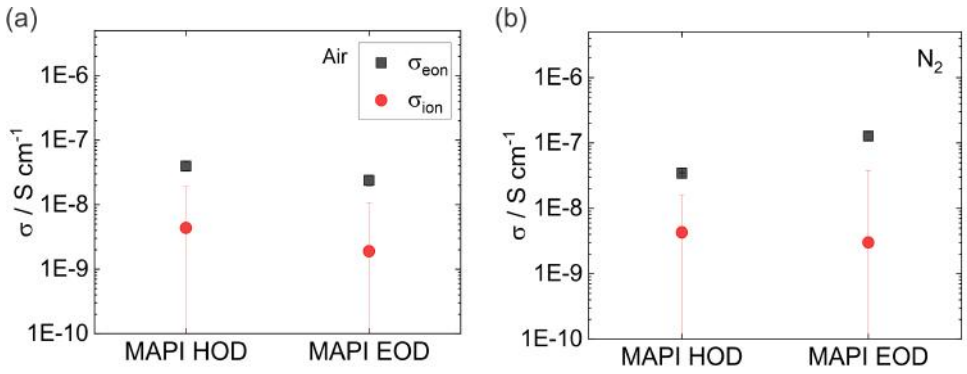

Figure 3.32: The electronic and ionic conductivities of MAPI in unipolar devices (HOD and EOD) devices that are fabricated (a) under air and (b) nitrogen.

ing materials (EOD). In addition, to verify the effect of oxygen doping, similar devices fabricated under nitrogen atmosphere are also characterized (Figure 3.32 and Figure 8 in appendix). The hypothesis for such experiment is shown in Figure 3.33. The E_F is closer to the valence band in the samples fabricated under dry air conditions, due to oxygen doping. As a result, the energy barrier for electron transport gets higher when MAPI is fabricated in air, while hole conduction should be favored.

The HODs fabricated in air and nitrogen show an electronic conductivity of approximately 4×10^{-8} S/cm, regardless of the environmental conditions during preparation. Interestingly this value is much larger than the value recorded for MAPI (V) in Figure 3.31, and even larger than the electronic conductivity measured for MAPI (H). This result clearly indicates the importance of excluding the recombination reaction between electrons and holes when evaluating the transport properties of hybrid perovskites. The fact that the conductivity is larger by two orders of magnitude compared with the value obtained for MAPI (H) may be ascribed to the effect of oxygen during the preparation. Because these samples are exposed to air after the deposition of the hole or electron transport layer on top of MAPI before gold top contact evaporation, and the preparation and characterization of the samples were carried out in different laboratories (EPFL in Lausanne and MPI in Stuttgart, respectively), it is not possible to exclude that, also for the samples in Figure 3.32

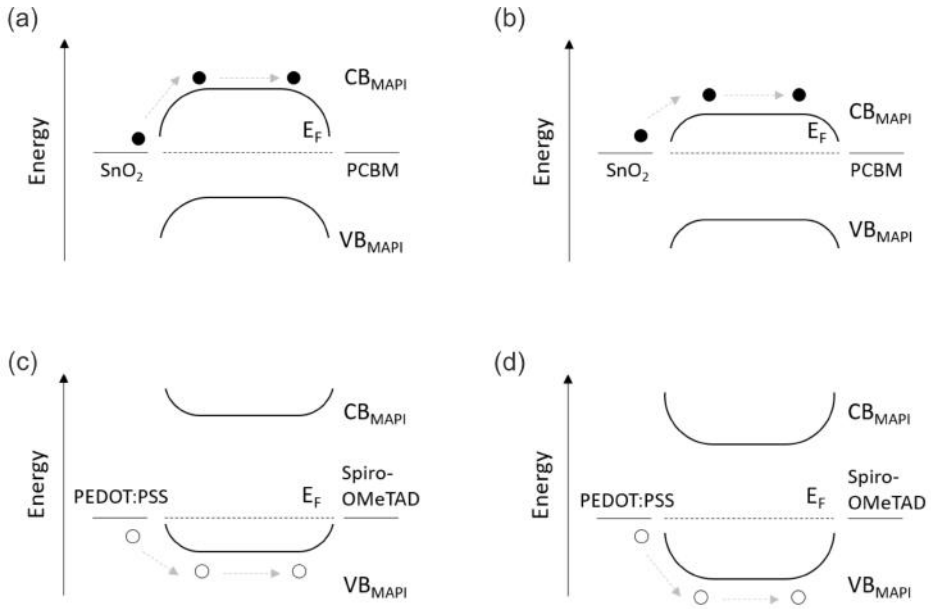

Figure 3.33: The energy diagram of EOD and HOD consist of MAPI active layer fabricated under (a),(c) air and (b),(d) nigrogen. Band bending of the contact material is not considered here.

(b), exposure to oxygen of the MAPI layer has occurred.

The EOD devices exhibit a conductivity of approximately 2.4×10^{-8} and 1.3×10^{-7} S/cm when prepared under dry air or nitrogen, respectively. Such value would suggest that, for these devices, the concentrations of electrons and holes are approximately similar (assuming similar mobilities for the two carriers). The larger value of the conductivity recorded for the EOD sample fabricated in nitrogen compared with dry air would point to a less p-type character of the MAPI layer in this case. Importantly, different degrees of permeation of oxygen may occur through the top contact depending on material properties, explaining the different trends observed for the HODs and EODs.

The large electronic conductivities in these devices imply a large error in the estimate of the ionic conductivity. The values extracted for such parameter are on the order of 3×10^{-9} S/cm for all samples. While the error is very large, this value is the same order of magnitude as the values extracted from the analysis of MAPI (H) and MAPI (V). This analysis suggests that, while a systematic analysis of the ionic con-

ductivity may be easier to carry out for horizontal rather than vertical structures, the use of the latter configuration still results in reasonable estimates and will be used further in the analysis below.

3.3.3 Effect of composite film in solar cells

This section aims to compare the properties of horizontal devices (MAPI deposited on interdigitated electrodes on sapphire substrate) and vertical devices (solar cell structure as well as single carrier devices). The use of different contact layer configurations is explored to emphasize the role of interfacial resistances and recombination resistances in the evaluation of the electronic conductivity in the perovskite.

In Chapter 3.1, the study of the ionically-generated space charge forming between alumina and MAPI is carried out. Modulation of such space charge is presented through the utilization of organic molecules modifying the alumina surface in A:MAPI composite films. Here, the focus lies in, first, investigating the effect of using such composite as the active layer of a perovskite solar cell and comparing the results to a control MAPI device and, second, verifying the effect of the surface modification within the solar cell device.

Solar cell devices are fabricated using the procedure described in Chapter 2. Four different active layer compositions are tested, similarly to the devices investigated in Chapter 3.1. Based on the findings reported in the previous section, the electronic and ionic conductivities measured through DC galvanostatic polarization and AC impedance measurement techniques for the solar cell devices are estimated and shown in Figure 3.34 (b), where they are compared with the results obtained in Chapter 3.1 (Figure 3.34 (a)).

In the solar cell configuration, the ionic and electronic conductivities are lower than the values extracted for the horizontal devices. The two data sets, however, highlight similar trends. While the overall electronic conductivity is very low for the solar cells, based on the contribution of the recombination resistance, in both vertical and horizontal devices, the A:MAPI composite exhibits the highest elec-

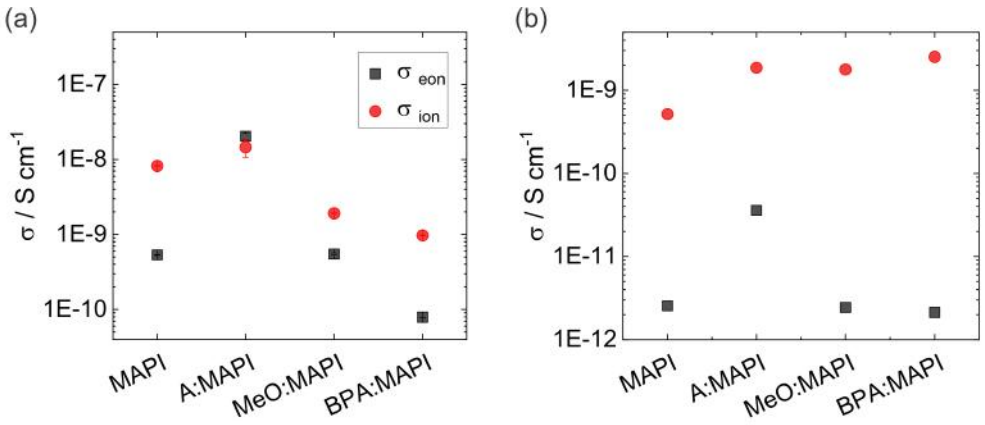

Figure 3.34: Electronic and ionic conductivities of (a) horizontal and (b) solar cell devices using MAPI, A:MAPI, MeO:MAPI and BPA:MAPI composite film as active layer.

tronic conductivity. Also, in both data sets, the surface-modified alumina shows much lower conductivity than the samples using unmodified alumina and slightly lower conductivity than MAPI. This trend could be attributed to the formation of a space charge at the interface between alumina and MAPI, which provides an efficient pathway for electron transport at the interface between the two materials, while most of the holes flow through the bulk material. Because of such inversion space charge forming between alumina and MAPI, the electrons, which are majority electronic charge carrier in the space charge zone, are transported close to the interface with alumina, where they can percolate from one electrode to the other. This not only increases the recombination of electrons and holes (lowering the recombination resistance) but also leads to the formation of a distributed p-n junction within the bulk of the device.

To verify this picture further, the electronic conductivity of HOD and EOD device with MAPI and A:MAPI composite active layer are compared (Figure 3.35). In the pure MAPI active layer, because holes are majority charge carriers, HOD shows slightly larger conductivities than EOD. However, the A:MAPI composite active layer device shows the opposite trend. EOD of this active layer shows a factor of 2.3 larger electronic conductivity than HOD. This confirms the presence of electron

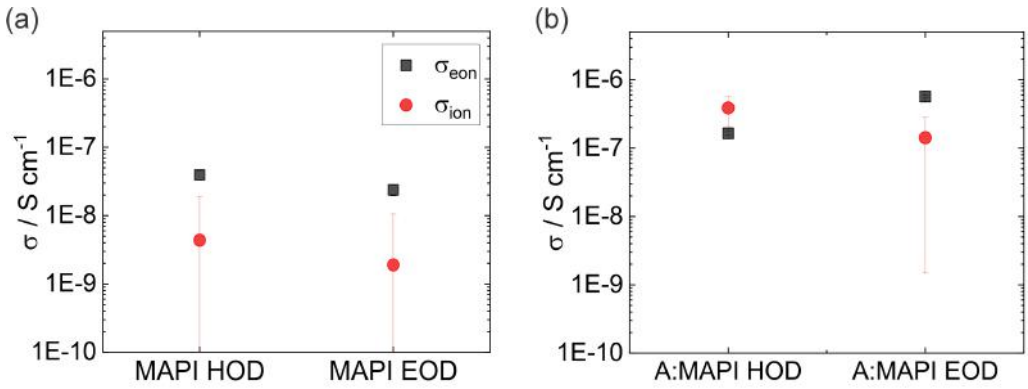

Figure 3.35: Electronic and ionic conductivities of unipolar devices consisting of MAPI and A:MAPI active layer fabricated in air.

conduction through space charge regions between alumina and MAPI. Based on this result, it is reasonable to expect that the space charge zones are percolating in MAPI layer from bottom ($mTiO_2$ interface side) to top (spiro-OMeTAD side) also in solar cell devices.

Consistently with the results in Chapter 3.1, the use of molecules on the alumina surface provides a strategy to suppress the formation of such space charge, as indicated by the similar values of conductivity measured for solar cell structures where surface modified alumina is used in the composite active layer compared to the MAPI active layer device. In other words, these devices are expected to have a reduced distributed p-n junction character in the active layer compared to A:MAPI composite device.

Next, the performance of these solar cell devices is measured under 1 sun equivalent illumination and the relevant photo-conversion parameters are shown in Figure 3.36 and 3.37. The data associated with the forward and the reverse scan collected during a current voltage measurements are included in the graphs. Compared with the MAPI control device, the sample with A:MAPI composite as active layer shows lower value of J_{SC}, V_{OC}, FF and overall PCE. This result indicate that the presence of the distributed p-n junction is not beneficial to the working mechanism of the solar cell. While such space charges could be expected to improve charge separation (holes being transported in the bulk and electrons close to the interface with alumina) and

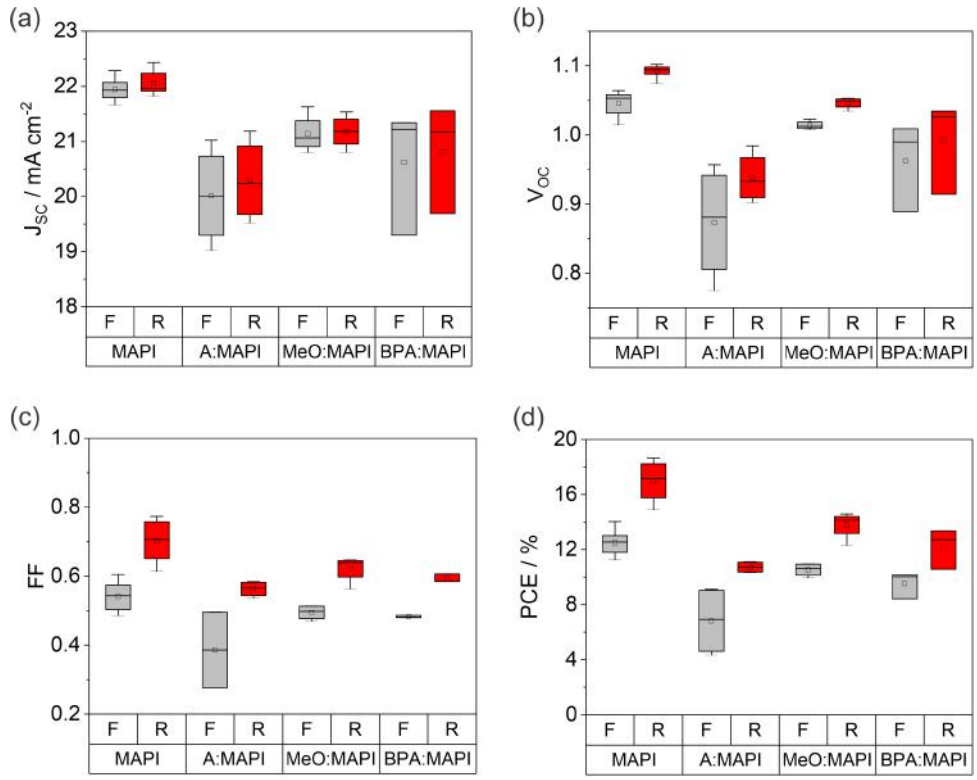

Figure 3.36: J_{SC}, V_{OC}, FF and PCE of solar cells. The active layer of solar cells are MAPI and composite films as A:MAPI, MeO:MAPI and BPA:MAPI with 0.8 vol% oxides.

to lower recombination (electrons and holes are far from each other), these data show that any such charge separation is not necessary, indeed it is detrimental to the performance of the solar cell.

Interestingly, the surface modified alumina shows improvement of V_{OC} and FF compared to solar cells with A:MAPI active layer. This result, once again, is consistent with a reduced ionically-generated space charge potential at the MAPI-alumina interface. Furthermore, because such reduced space charge potential improves the V_{OC} and solar cell performance it also supports the hypothesis that the low efficiency recorded for the A:MAPI solar cell is due to formation of such distributed p-n junctions in the active layer, rather than due to the presence of the particles and the different morphological properties of the active layer. The data suggest that, for hybrid perovskites such as MAPI, having electrons and holes being uniformly trans-

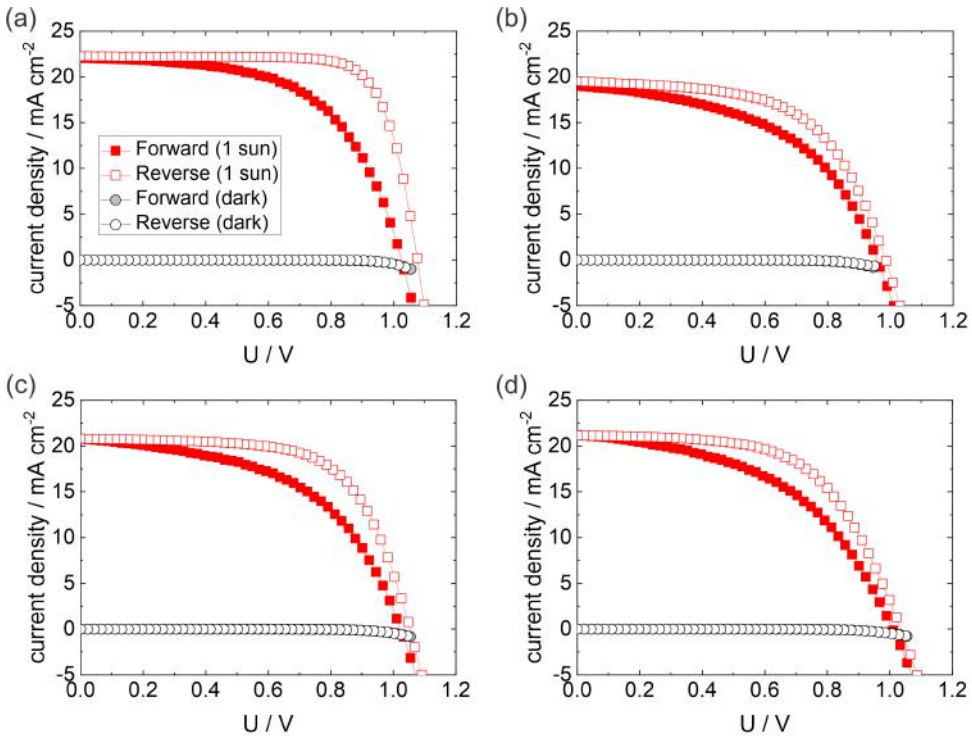

Figure 3.37: J-V curve of (a) MAPI, (b) A:MAPI, (c) MeO:MAPI and (d) BPA:MAPI based solar cell in the 1 sun and dark condition.

ported within the bulk of the active layer is a more favorable strategy to improve solar cell performance rather than having separated p and n conduction paths.

3.3.4 Effect of surface modified mesoporous oxide layers in solar cells

In Chapter 3.2, the interfacial situation at the MAPI/mTiO_2 interface was studied. Such study was also conducted for the cases with or without MeO-2PACz and BPA molecules modifying the oxide surface. In this chapter, such investigation is applied to solar cells in order to study the influence of the space charge region in the infiltrated MAPI, as well as of surface modification, on the performance of these devices.

First, in order to investigate the role of the MAPI infiltrated in the mTiO_2 layer, a mTiO_2 thickness dependent study is performed. In this experiment, a device

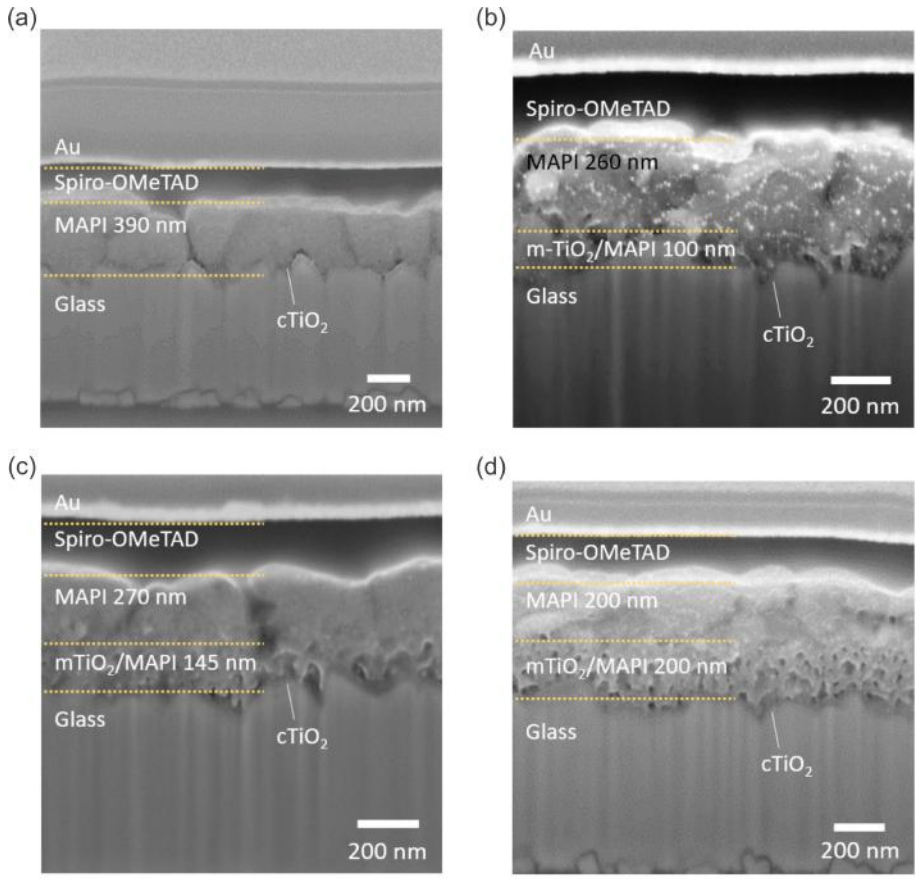

Figure 3.38: The cross section SEM images of different $mTiO_2$ thickness devices. The samples cross sections are prepared by FIB.

structure FTO/$cTiO_2$/$mTiO_2$/MAPI/spiro-OMeTAD/Au is used. The $mTiO_2$ layer was fabricated with different concentration of the TiO_2 paste used. Details on the procedure are described in Chapter 2. Figure 3.38 shows the SEM cross sectional images of the devices, indicating the successful variation of the $mTiO_2$ layer thickness in the range between 0-200 nm. Beside the MAPI phase that is infiltrated in the oxide pores, an additional capping layer of MAPI is present in all devices, with thickness in the order of 200-270 nm.

The partial conductivities of these devices are measured using AC and DC measurements and they are displayed in Figure 3.39. The J-V curve of this device is shown in Figure 3.40. Interestingly, while the ionic conductivity extracted from such series of devices is approximately unvaried, a decreased electronic conductivity is

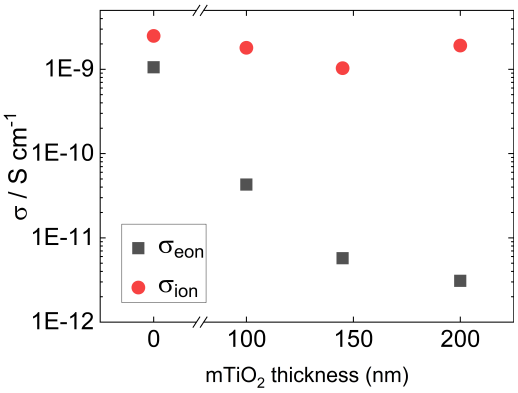

Figure 3.39: Electronic and ionic conductivities of MAPI based device with different thickness of $mTiO_2$ layer.

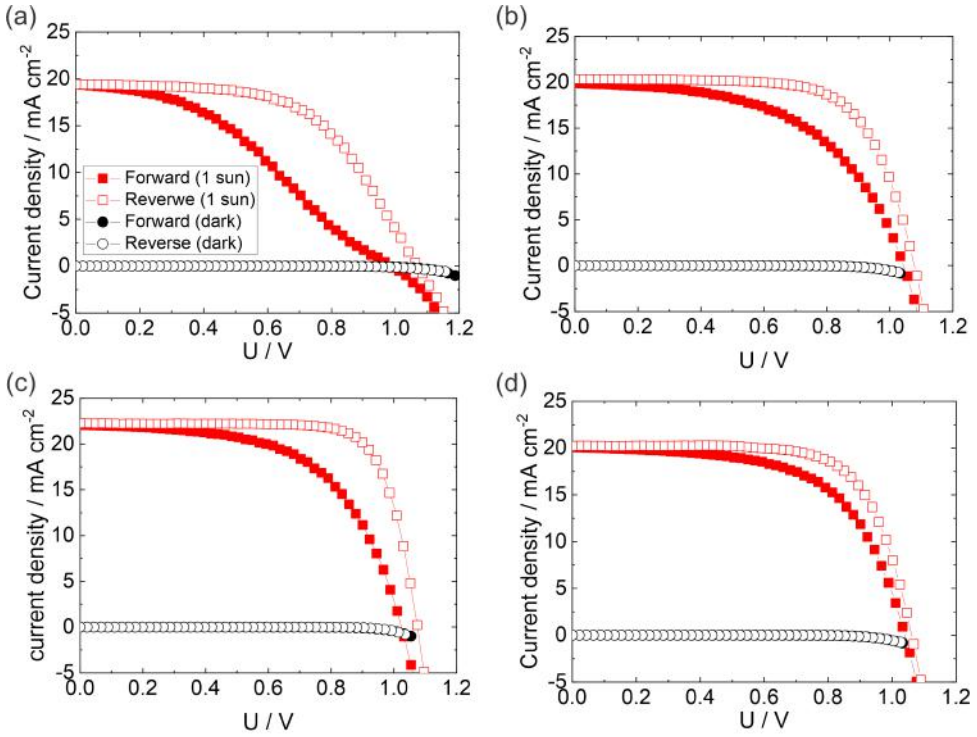

Figure 3.40: The J-V curve of $mTiO_2$ layer thickness of (a) 0, (b) 100, (c) 145 and (d) 200 nm.

observed for increasing $mTiO_2$ thickness. This result suggests that the presence of a depletion space charge between MAPI and TiO_2 is responsible for a significantly lower conductivity of MAPI within the pores of the $mTiO_2$ compared with pure MAPI. This introduces a significant resistance in series with the capping layer resis-

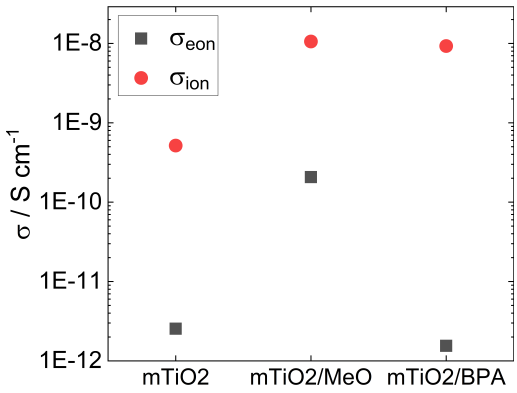

Figure 3.41: Electronic and ionic conductivities of MAPI based solar cells with, without surface modification on $mTiO_2$. '$mTiO_2$' refers to $mTiO_2$/MAPI device, 'mTiO2/MeO' $mTiO_2$/MeO2PACz/MAPI device, and 'mTiO2/BPA' $mTiO_2$/BPA/MAPI device.

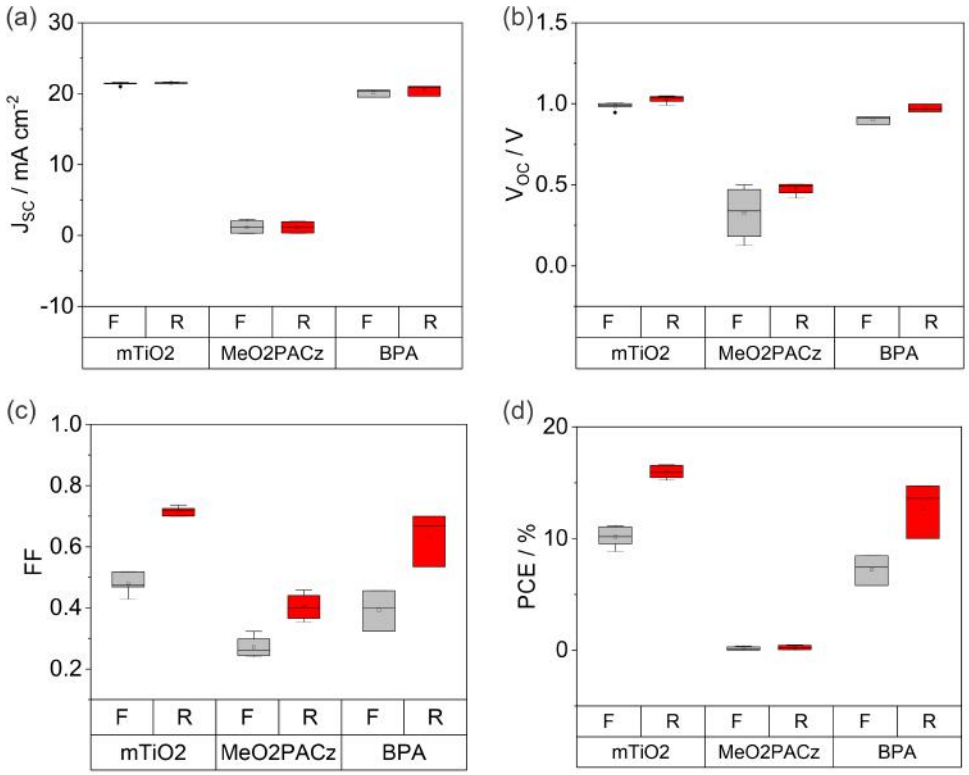

Figure 3.42: Device performances of MAPI based devices with, without MeO-2PACz and BPA on surface of TiO_2. In the figures, 'mTiO2' refers to $mTiO_2$/MAPI devices, 'MeO2PACz' represents $mTiO_2$/MeO2PACz/MAPI devices, and 'BPA' denotes $mTiO_2$/BPA/MAPI devices.

tance and the recombination resistance, reducing the overall electronic conductivity measured for the device when increasing the $mTiO_2$ layer thickness.

Next, solar cells with unmodified and surface modified $mTiO_2$ layers are compared. A $mTiO_2$ layer of thickness 145 nm is used for this experiment. The impedance data collected under dark is used to extract electronic and ionic conductivity of the devices. These are estimated to be 10^{-8}-10^{-10} and 10^{-10}-10^{-8} S/cm, respectively (Figure 3.41). The high electronic conductivity in the $mTiO_2$/MeO is probably due to the fact that the molecule is a hole conductor and it is adsorbed on TiO_2 that is an ETM, which is likely to increase the recombination at that interface.

3.3.5 Conclusions

It was shown that vertical device structures can be used in the analysis of partial conductivities of the mixed conducting active layer, provided that appropriate contacts are explored. The control of the environment where the hybrid perovskite is fabricated is crucial in the determination of the electronic conductivity due to oxygen doping, consistent with previous studies.

Regarding the influence of space charge effects at the MAPI/oxide interface on solar cell behavior, the findings reported in this chapter show that a distributed p-n junction within a hybrid perovskite active layer is not an effective strategy to improve photoconversion efficiencies of these devices. Specifically, the use of particles of alumina, or other insulating materials that induce ionically-generated space charges within composite films, significantly reduces the performance of devices compared with the MAPI only control device. Surface modification with BPA molecules does not affect significantly the electronic properties of the oxide surface that is modified (electron transfer and equilibration between MAPI and the oxide). In the case of alumina, BPA blocks (at least partially) the ionic adsorption and reduces the space charge potential magnitude, with evident effects in the conductivities measured for horizontal devices and in the solar cell performance.

Regarding the interface between MAPI and $mTiO_2$, $mTiO_2$ thickness dependent

data show that the space charge forming at such interface may be very important in reducing the hole concentration close to the ETM of the solar cell. The data show that BPA modification does not modify significantly the space charge situation. This could be because, for this oxide, ions are still able to reach the surface of the oxide, or because the electronic equilibration between MAPI and $mTiO_2$ has a major contribution to the space charge equilibrium of this interface. Because BPA does not change such equilibration significantly, the partial conductivities in horizontal devices are comparable for the $mTiO_2$ and $mTiO_2$/BPA systems and the respective solar cell efficiencies are also largely unvaried.

In order to clarify this question further, one could examine the electronic and ionic conductivity changes on BPA surface modification of a charge transporting oxide that has opposite electronic equilibration properties with MAPI, compared to TiO_2. Also, it would be useful to test molecules with larger size that do not have electron blocking properties. In this way, the role of molecular size in the ion blocking ability of the surface modifying molecule and in the photoconversion processes in solar cells could be verified.

3.4 Relating surface and electronic properties to the ionic space charge formation between oxides and hybrid perovskites

In the previous chapters, the influence of ionically-generated space charges was investigated for composite films, mesoporous films and vertical device configuration (*e.g.*, solar cell structure), and alumina and titania were used as model contact materials. The results emphasized the importance of the ionic interaction at the interface between MAPI and the insulator alumina in the charge carrier redistribution in MAPI close to its surface, an effect that can be modulated via surface modification strategies. They also suggested that, in the case of an electronically conducting oxide, such redistribution may result from a combined electronic and ionic equilibration.

In this chapter, the study of ionic interactions on the formation of space charge at the interface of MAPI with insulating or semiconducting oxides is extended to other materials, aiming for a general understanding of these effects based on the contact phases' electronic and surface properties. Given the more accessible analysis of composite films, this configuration will be considered for the investigation of the electrical properties.

Ion adsorption phenomena in composite films including alumina have been reported for systems involving several different ionic and mixed conductors [125, 126]. In order to explore whether the observed ionically-generated space charge effects in alumina:MAPI films is a phenomenon exclusive to alumina or a more general effect, other insulators, such as silicon dioxide (SiO_2) and magnesium oxide (MgO), are investigated here. Films of MAPI and of Al_2O_3:MAPI are used as control samples in this experiment. These oxide materials are selected based on their distinct surface ionic interactions compared with Al_2O_3, as documented in the literature [127, 128]. Table 3.2 reports the points of zero charge measured for these oxides. Note that

Table 3.2: Point of Zero-charge value of oxides that are used in this study [125, 126].

Oxide	PZC	Electrolyte
Al_2O_3	9	NaCl
SiO_2	3	NaCl or KCl
MgO	12	$MgCl_2$ + KCl
NiO	10	NaCl

these values are meant as rough estimates as they depend on surface crystallography. Nevertheless, they show pronounced differences in the tendency of these materials to interact with cations or anions in aqueous solution. The objective of this work is to assess whether such difference in surface properties is reflected in their ionic interactions with MAPI, within composite films. Insulating oxides are particularly suited to answering this question due to fact that their electronic properties can be excluded from the data analysis, allowing one to focus solely on ionic effects. In addition Al_2O_3, SiO_2, and MgO have been previously employed in solar cells, in order to minimize surface recombination [129, 130], making their study potentially relevant to device optimization.

A second question, which is of relevance based on the findings reported in the previous chapters, concerns the interplay between ionic and electronic effects in the determination of the space charge situation between MAPI and a semiconducting contact phase. As shown in Figure 3.43, the sign of the space charge potential can be easily predicted when these two effects are "pointing in the same direction". This is for example the case of the TiO_2/MAPI interface, where both electron transfer from TiO_2 to MAPI and cation adsorption on the surface of TiO_2 would lead to a space charge potential with the same sign (see Chapter 3.2). In situations, where these two effects contribute in opposite directions, it can be difficult to predict which effect would dominate.

Here, I focus on the study of the space charge situation at the interface between MAPI and the hole transporting material nickel oxide (NiO). NiO is a commonly used hole transporting material in perovskite solar cells [91, 92]. NiO has a work

(a)

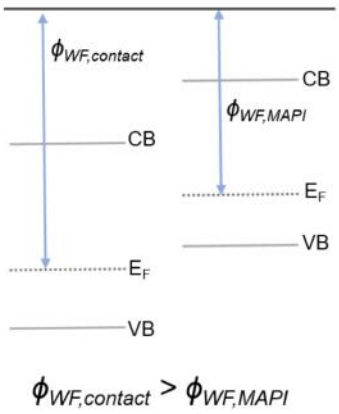

(b)

	Cation adsorption	No ion interaction	Anion adsorption
$\phi_{WF,contact} > \phi_{WF,MAPI}$	MAPI:NiO (in this study)	$\phi_{space\ charge} < 0$	?
$\phi_{WF,contact} \sim \phi_{WF,MAPI}$	$\phi_{space\ charge} > 0$ (e.g. Al_2O_3)	$\phi_{space\ charge} = 0$	$\phi_{space\ charge} < 0$
$\phi_{WF,contact} < \phi_{WF,MAPI}$	$\phi_{space\ charge} > 0$ (e.g. TiO_2)	$\phi_{space\ charge} > 0$	?

$\phi_{space\ charge}$ indicate space charge in MAPI

Figure 3.43: (a) Diagram of the energy levels of a contacting material and MAPI, before contact. The difference in work function (ϕ_{WF}) between the two materials establishes an electronic contribution to the space charge potential. (b) The expected sign of such potential, depending on different electronic and ionic interactions between the materials.

function of about 5.3 eV. This means that its E_F, lies at lower energies compared with MAPIs, whose work function is in the order of 4.7 eV under common preparation conditions. When NiO is in contact with MAPI, an accumulation of holes in a space charge within the MAPI side of the interface would be expected (electronic equilibration). However, the point of zero charge (PZC) of NiO is reported to be 10 (see Table 3.2), suggesting cationic interaction on its surface, similar with alumina. This would induce the formation of a depletion of holes within a space charge in the MAPI side. Clarifying the space charge situation at the NiO/MAPI interface is an important aspect in the optimization of charge extraction and recombination

performance in devices using such material as HTM.

3.4.1 Interaction of MAPI precursors at the oxides' surfaces

In order to investigate the interaction between the selected oxides with ions in MAPI, the zeta potential is measured in a DMSO solution containing various salts (*e.g.* MA^+, Pb^{2+}, or I^- ions). In the $Pb(NO_3)_2$/DMSO solution, Al_2O_3, SiO_2 and NiO shows similar Pb^{2+} interaction. On the other hand, MgO exhibited a smaller zeta potential value, suggesting that Pb cations are adsorbed less on the surface of MgO compared to others. This is in contrast with the very large value of PZC recorded for MgO, the largest in this series of materials. This result already indicates how specific interactions may be essential in the investigation of surface properties, even in the solution case.

The measured zeta potential value in the case of particles immersed in a PbI_2 solution decreases close to zero, while in the case of a mixed solution of PbI_2 and MAI, the zeta potential shows a negative value, possibly due to the complexation of Pb and I (see also zeta potential experiment results in Chapter 3.1.1) [131]. In the MAI case, a negative value is observed, indicating anion adsorption on the surface of alumina. However, a previous study has shown that the adsorption of I anion

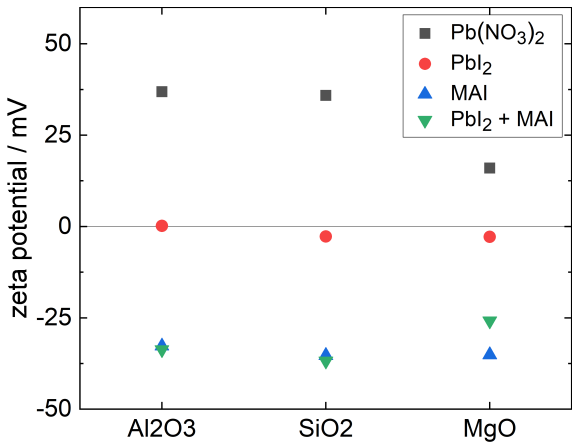

Figure 3.44: Zeta potential measurements of insulating oxides in the presence of various salts. Each oxide is dispersed in solution with 2 wt% concentration.

does not occur when Pb cation is present in the solution using $Pb(NO_3)_2$ and KI salts [82]. Additionally, based on previous studies of high ionic conduction in AgX:alumina [125, 126] which show vacancy concentration enhancement on the surface of alumina, it can be concluded that these oxides adsorb cations on the surface. These results differ from the PZC values reported in the literature, likely due to differences in the salt and solvent used for measurement. However, in this study, DMSO solvent, which is used for MAPI fabrication, and MAPI-related ion salts were used, providing a more relevant context for the following conductivity measurement results obtained.

3.4.2 Ionic interactions at the interfaces between insulating oxides and MAPI

3.4.2.1 Composite film morphology and crystallinity

The MAPI and oxide:MAPI composite films are deposited on sapphire substrates patterned with interdigitated Au electrodes using the sample preparation method described in Chapter 2. The concentration of the oxide in the films are selected by conducting preliminary conductivity measurements. Concentrations as low as possible and, at the same time, large enough to ensure a measurable change in conductivity (Figure 1 in appendix) are selected. The introduction of alumina and silica particles in MAPI films at a concentration of 0.30 vol% showed an electronic conductivity change within a factor of 2 compared with the MAPI film. On similar nominal particle concentration conditions, the MgO:MAPI composite film shows a more significant change of approximately one order of magnitude. Therefore, a higher concentration of alumina and silica (0.80 vol%) is used, while MgO is used with 0.30 vol% in the film fabrication.

The morphology of each film is examined using SEM imaging (Figure 3.45). The crystal size of all films is between 100-200 nm. The Al_2O_3 and SiO_2 in MAPI composite films exhibited a rougher surface compared to the pure MAPI film, possibly

due to some oxide aggregation within the film. The cross-sectional SEM images reveal that all films are approximately 200 nm thick and have been fabricated without any noticeable voids or pin-holes.

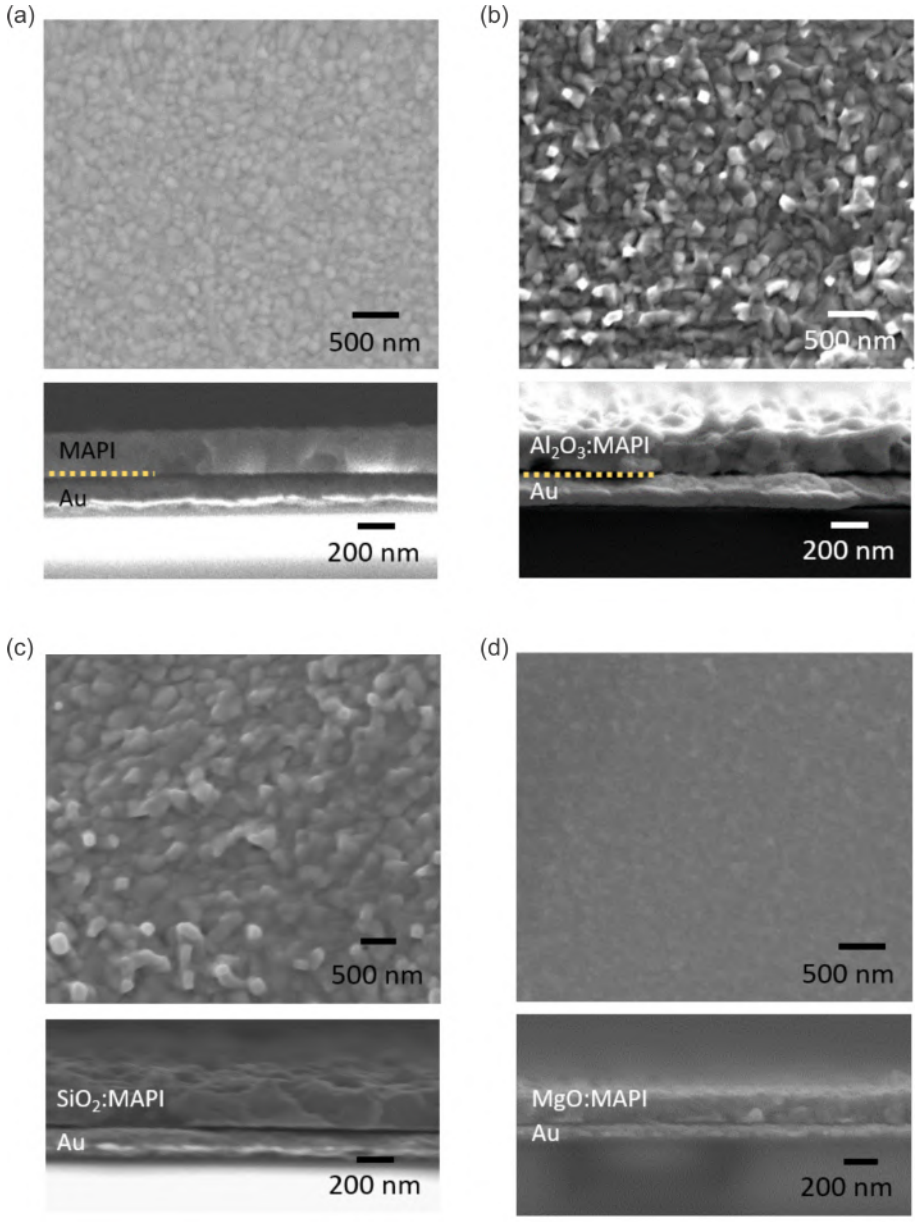

Figure 3.45: The surface (above) and cross-sectional (below) SEM images of the following samples are shown: (a) MAPI, (b) 0.8 vol% Al_2O_3:MAPI, (c) 0.8 vol% SiO_2:MAPI, (d) 0.3 vol% MgO:MAPI films. The concentration of oxides used in the composite films is optimized at the nominal concentration.

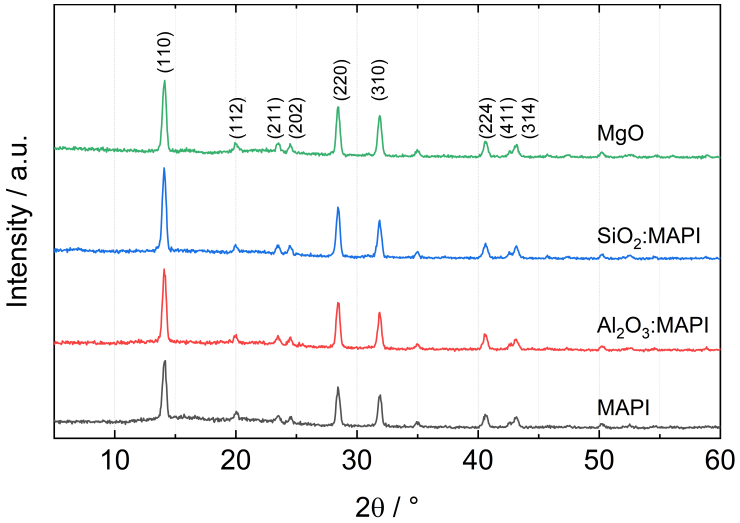

Figure 3.46: The XRD results of MAPI and oxide:MAPI composite films indicate that all the films exhibit the tetragonal phase of MAPI, without PbI_2.

The crystal structure is examined using XRD (Figure 3.46), and all the films exhibited peaks corresponding to the tetragonal structure of MAPI without any PbI_2 signiture, which could be a residue from the fabrication process or degraded MAPI product. No peaks associated with the oxide particles are detected, possibly because the small particles (less than 50 nm) are dispersed in the MAPI film with a low volume fraction of 0.3 to 0.8 vol%.

3.4.2.2 Results and interpretations of electronic and ionic conductivities

Figure 3.47 and 3.48 show the AC impedance and the DC polarization measurements performed in argon and $p(I_2) = 3.5$ μbar atmosphere, respectively. The total conductivity (including both electronic and ionic conductivity) of the samples is calculated from the high frequency features of the impedance spectra, which is associated with the bulk conductivity properties of MAPI (the capacitance of such feature is in the order of C $\approx 10^{-8}$ F/cm^2).

The films are subsequently measured under a fixed $p(I_2)$ environment, and their change in conductivity is discussed here in terms of potential contributions to the conduction due to the interfacial regions between MAPI and each oxide phase (Fig-

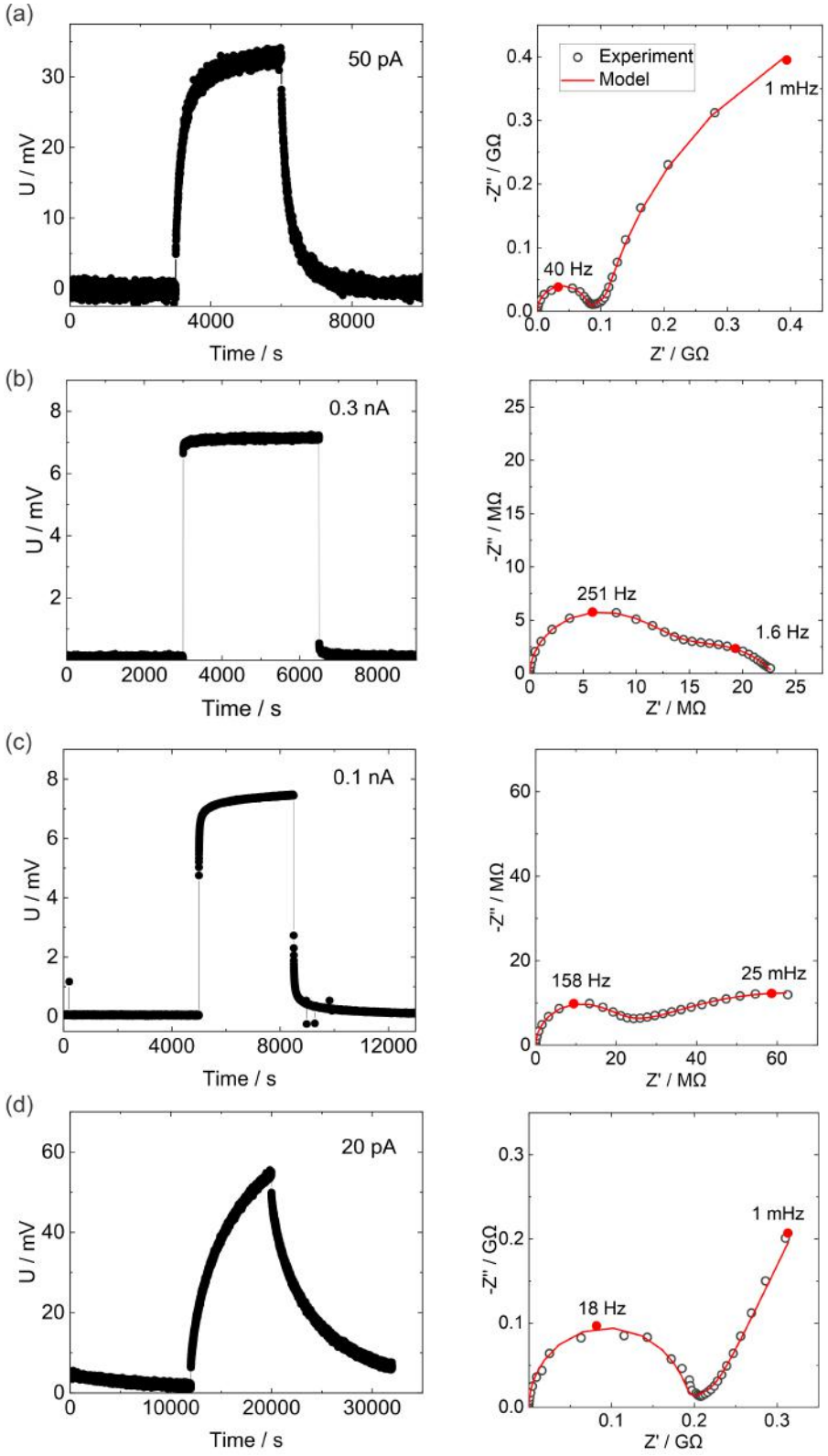

Figure 3.47: Galvanostatic DC polarization curves (left) and AC impedance measurements (right) performed on (a) MAPI, (b) Al_2O_3:MAPI, (c) SiO_2:MAPI and (d) MgO:MAPI films in Ar, dark conditions at 40 °C.

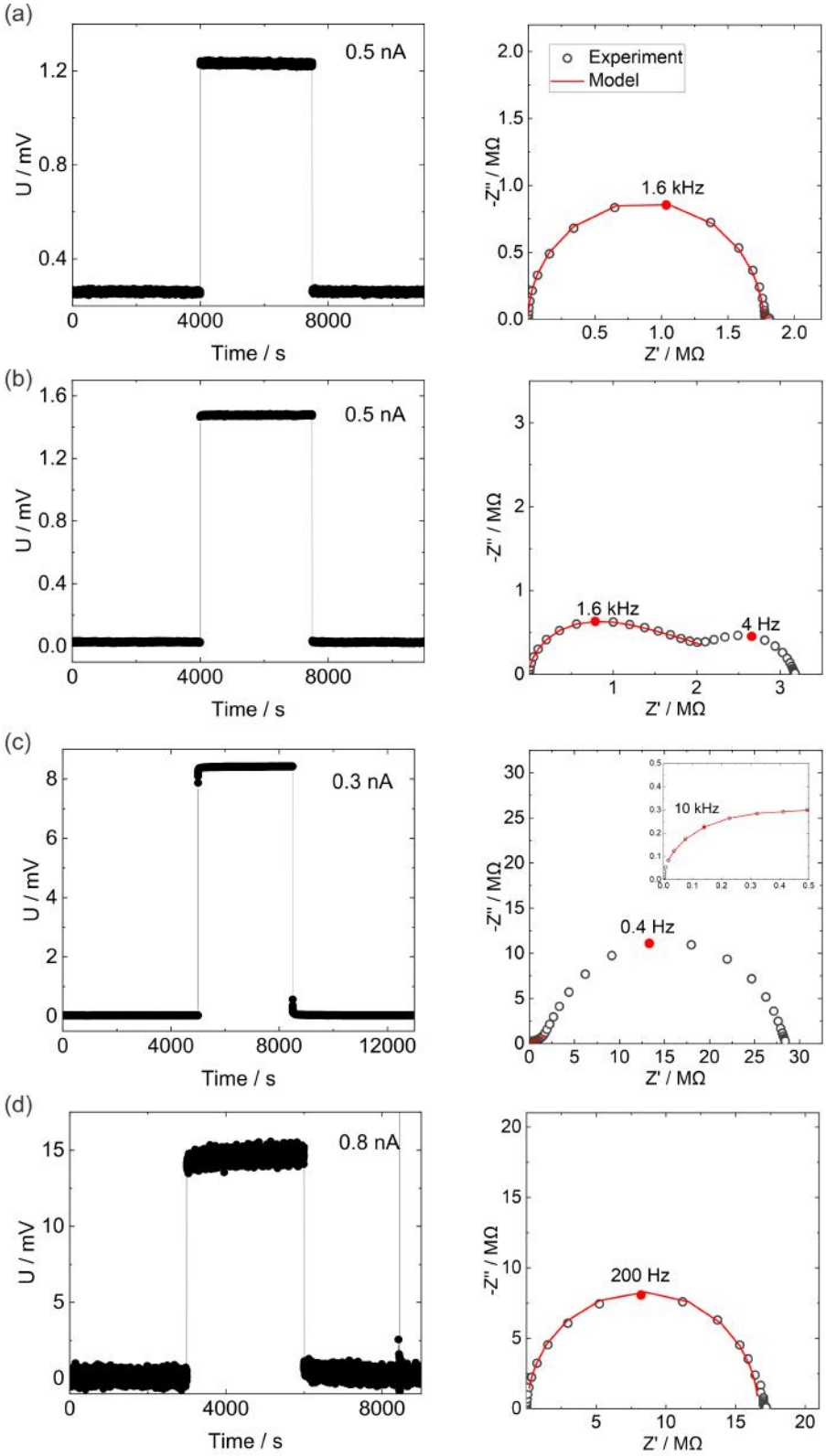

Figure 3.48: Galvanostatic DC polarization curves (left) and AC impedance measurements (right) performed on (a) MAPI, (b) Al_2O_3:MAPI, (c) SiO_2:MAPI and (d) MgO:MAPI films in $p(I_2) = 3.5$ μbar, dark conditions at 40 °C.

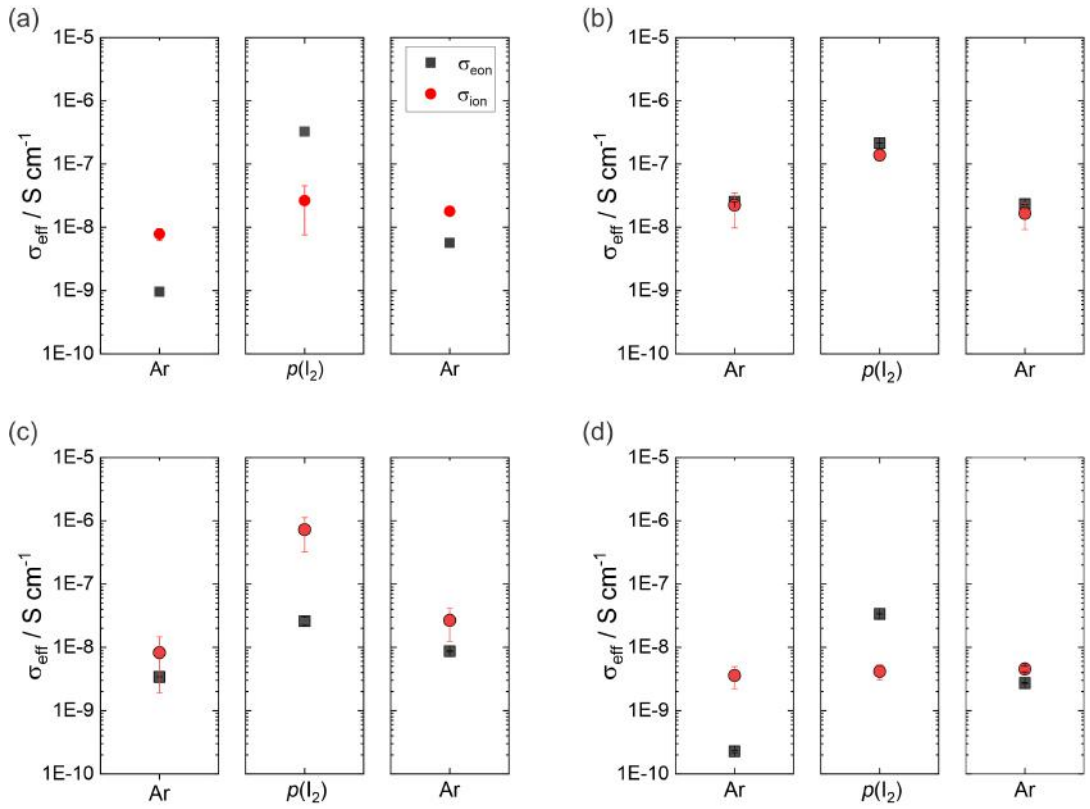

Figure 3.49: Results of conductivity measurement in Ar and $p(I_2) = 3.5$ μbar of (a) MAPI, (b) Al_2O_3:MAPI, (c) SiO_2:MAPI and (d) MgO:MAPI films.

ure 3.49). The MAPI film shows more than 2 orders of magnitude increase of electronic conductivity from Ar to $p(I_2)$ condition. This is consistent with the literature, and the data presented in Chapters 3.1 and 3.2, and it is assigned to an increase in the electron hole concentration. The alumina:MAPI composite film showed a less pronounced increase in electronic conductivity, confirming the reproducibility of the data in Chapter 3.1. In particular, under Ar, the electronic conductivity in this film is an order of magnitude larger than MAPI, consistent with the formation of an inversion space charge region at the interface between alumina and MAPI (see Chapter 3.1). By increasing iodine partial pressure, this inversion effect disappears and the electronic conductivity is increased by one order of magnitude due to the hole conduction in the bulk of MAPI. The smaller increase of electronic conductivity from Ar to $p(I_2)$ condition compared with MAPI is therefore associated with a

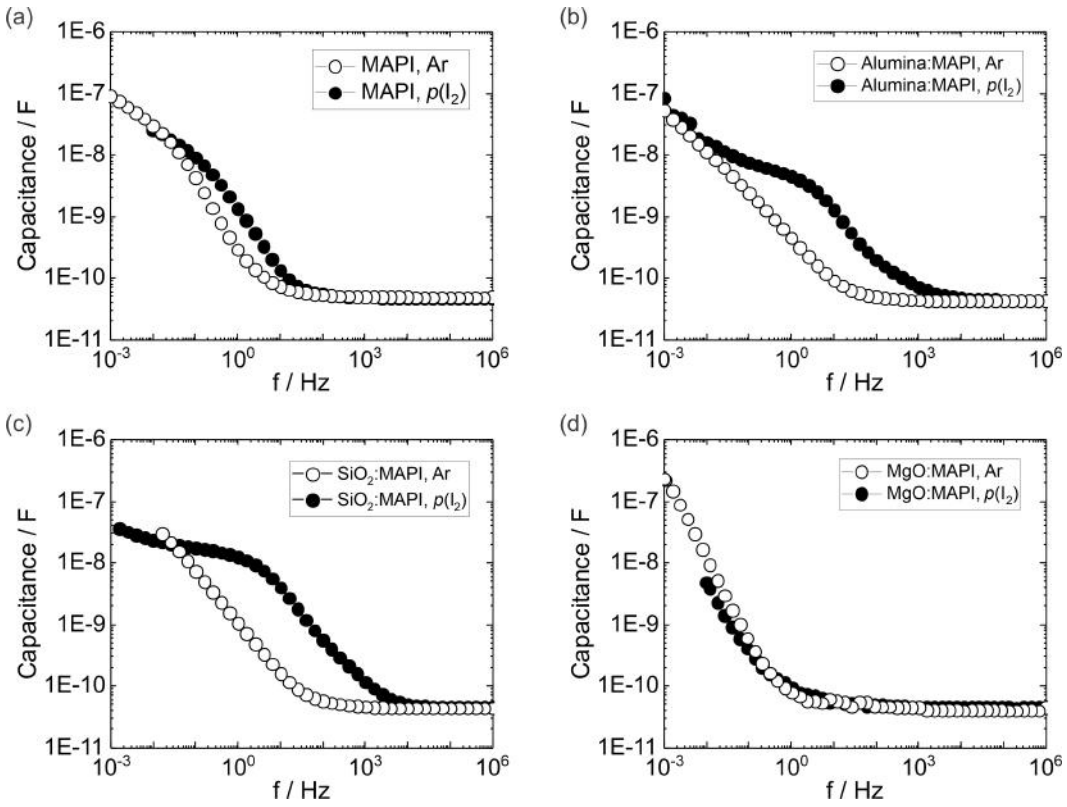

Figure 3.50: Capacitance results obtained from impedance measurement of (a) MAPI, (b) Al_2O_3:MAPI, (c) SiO_2:MAPI and (d) MgO:MAPI films. The capacitance of each films is obtained in Ar and $p(I_2)$ = 3.5 μbar condition. When the films are under $p(I_2)$ condition, the mid-frequency capacitance is changed. This value could be considered as grain boundaries of MAPI or double layer formation between MAPI and Au electrode layer.

combined effect, whereby electron conduction in the inversion layer decreases and the hole conduction in the bulk increases when increasing the $p(I_2)$.

The electronic conductivity trend recorded for the SiO_2:MAPI film shows similar results compared with the alumina composite film, with an enhancement of a factor of 5 between the argon and the fixed $p(I_2)$ condition. The absolute value of such conductivity is however significantly lower than for the alumina composite, suggesting that the morphology of the film may be less favorable for transport. This result already confirms that the ionically-generated space charge effects demonstrated for the MAPI:alumina system is not unique to the properties of alumina, but they are a rather general aspect which needs to be considered wherever ionic interactions are

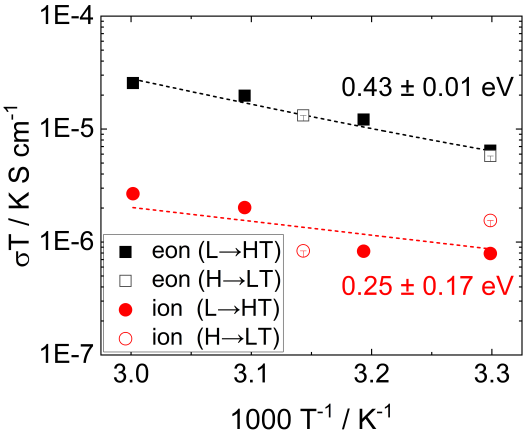

Figure 3.51: The activation energy for electronic and ionic conductivity of an MgO:MAPI film. The measurement is performed under iodine partial pressure condition ($p(I_2) = 3.5$ μbar).

expected.

The estimate of the ionic conductivity of the SiO_2:MAPI composite film under argon leads to a similar value as the one extracted for MAPI. When considering the high-frequency semicircle of the impedance spectrum to evaluate the total conductivity of the film also in the fixed $p(I_2)$ situation, the extracted ionic conductivity is larger by 2 orders of magnitude compared with the argon case. This result is not very likely, in that such change in ionic defect concentration would occur only if the sample are in the P or N region. If that is the case, the electronic conductivity would be expected to be much larger than the measured value, given the difference in charge carrier mobility between the ionic and the electronic defects. The observed change in impedance may be explained considering that electronic conduction may dominate the whole response of this composite films (Figure 3.47 and 3.48), whereby the high-frequency and low frequency features may be associated with conduction within the grains and the contribution of grain boundaries, respectively. For an accurate ionic conductivity extraction, further measurements under lower iodine partial pressure or examination of different oxide particle concentrations would be required.

The measured electronic conductivity of MgO:MAPI composite is 10^{-10} S/cm un-

der argon, significantly lower than for the MAPI case and for the other composite films. The ionic conductivity of this film is also lower compared with MAPI films, by a similar factor. This result may be explained based on two non-exclusive hypotheses: (i) blocking effect of insulating MgO particles could decrease both partial conductivities by a similar amount; (ii) the presence of an ionically-generated space charge at the MAPI/MgO interface, of lower magnitude compared with alumina, would not result in an inversion layer but rather only to depletion of holes and iodide vacancies. When the MgO:MAPI film is measured under fixed $p(I_2)$ condition, the electronic conductivity increased by a similar factor as for the MAPI film, while the ionic conductivity is not changed compared to the argon condition. These observations are consistent with both (i) and (ii) above. In order to ascertain which effect is dominant, the activation energies of the electronic and ionic conductivity are measured for this sample (Figure 3.51). The E_a of electronic and ionic conductivity showed values of 0.43 eV and 0.25 eV, respectively. The electronic activation energy showed a value similar to MAPI (see Chapter 3.1 and 3.2). However, the E_a for ionic conductivity showed a smaller value compare with the expected value of a MAPI film. Because the extraction of the electronic conductivity in these systems is more reliable (it is a direct measurement), we focus on the fact that $E_{a,eon}$ is unvaried in the composite film compared to MAPI. This finding points towards hypothesis (i), whereby blocking effects simply hinder the transport of charge carriers, with no evident contribution from space charge effects. It is important to note that, if ionic and electronic charge carriers are able to percolate through the film, without having to travel close to the particles, the presence of a depletion layer in proximity of MgO, which is however less pronounced than for the alumina or silica case, cannot be fully ruled out.

3.4.3 Ionic vs Electronic contributions to space charge formation - NiO:MAPI composite films

3.4.3.1 Film morphology and crystallinity

Films of MAPI and NiO:MAPI composites are fabricated on Au patterned sapphire substrates following the procedure described in Chapter 2. The SEM images depict the MAPI film and the NiO:MAPI composite film with a NiO concentration of 0.30 vol% (Figure 3.52). The NiO:MAPI film exhibits relatively smaller crystal sizes compared to the MAPI film. However, the surface morphology and film thickness appear to be similar in both films.

The crystallinity of the films is examined using XRD (Figure 3.53). The XRD analysis confirmed that the MAPI film exhibited a tetragonal phase without any clear PbI_2 peak. Similarly, the NiO:MAPI film showed the tetragonal MAPI phase. However, the NiO peak is not visibly detected in this film, which is attributed to the low concentration of small particle NiO (approximately 18 nm), which may be below the detection limit of the XRD technique.

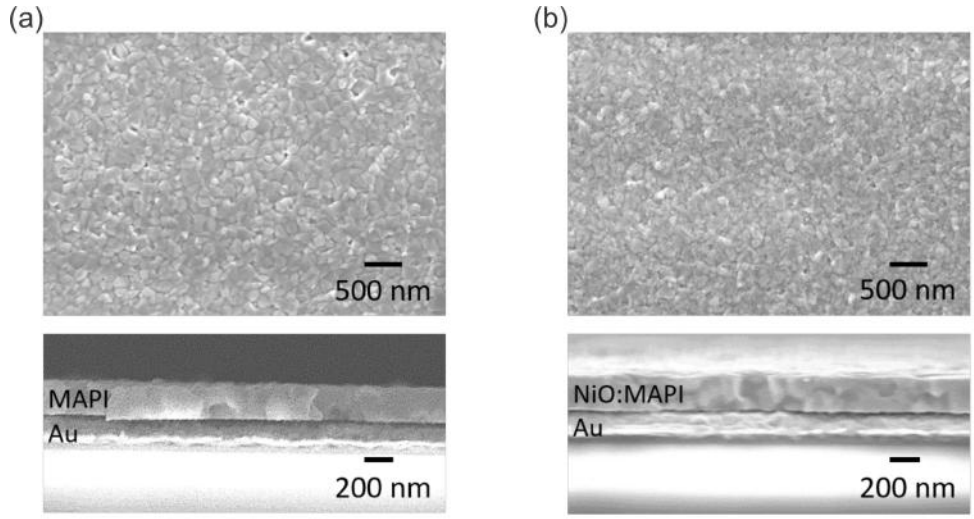

Figure 3.52: Surface (above) and cross-section (bottom) SEM images of (a) MAPI film, (b) NiO:MAPI with 0.30 vol% nominal concentration composite film.

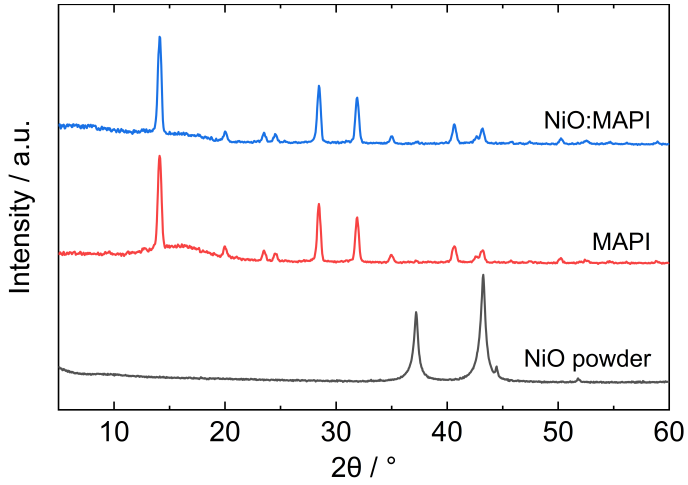

Figure 3.53: XRD of NiO nanoparticle powder, MAPI and NiO:MAPI composite films.

3.4.3.2 Results and interpretation of electronic and ionic conductivity measurements.

First, the electronic and the ionic conductivity under argon for different (nominal) volume fraction of NiO in MAPI composite films are measured (Figure 3.54). The NiO volume fraction was varied in the range between 0.02 to 3 vol%. The electronic conductivity results show an increase of about one order of magnitude (from 2×10^{-9} to 2×10^{-8} S/cm) in this volume fraction range. Interestingly, such increase is visible already in the low NiO concentration range (0.02 vol%), and it is approximately linear up to the maximum concentration explored here (3 vol%). Because NiO has a large conductivity, these data cannot simply be interpreted in terms of interfacial effects on the MAPI side, as it has been done for the insulating oxide and also the mTiO_2 case in the previous chapters. Understanding whether its origin is related with space charge effects at the interface between MAPI and NiO, rather than simply being due to the contribution of highly conductive path of NiO in the film, requires a careful analysis of the data.

In Figure 3.55 five possible scenarios are illustrated: (a) shows a situation where electronic equilibration dominates the charge carrier distribution between NiO and MAPI. This equilibrium will induce an accumulation space charge large at this

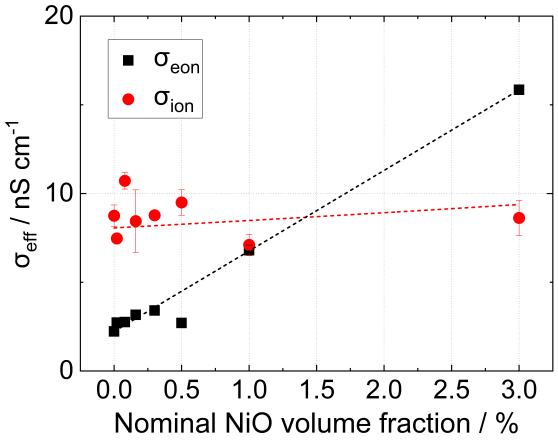

Figure 3.54: Ionic and electronic conductivities measured for NiO:MAPI composite films under argon at 40 °C as a function of the NiO particles nominal volume fraction.

interfaces, resulting in an enhanced conduction of holes and iodide vacancies through this space charge zone (hole conduction through the NiO particles is also possible here); (b) is similar to (a) but the space charge regions induced by the particles do not form percolating pathways; (c) shows the case where an ionically-generated space charge forms due to cation adsorption on the surface of NiO, leading to the formation of an inversion layer (at $p(I_2)$) where electrons can percolate; (d) shows the case where no significant space charge is formed and NiO is simply contributing to the electronic conductivity of the film through percolating paths; (e) is similar to (d) but without percolation of the particles.

The linear increase in electronic conductivity with particle content shown in Figure 3.54 is potentially consistent with all five scenarios discussed above. However, one important observation is that the ionic conductivity does not change when the NiO particles are included in the film and their volume fraction is increased. This observation implies that ionic charge carriers (iodide vacancies) are transported predominantly by MAPI, rather than in NiO or at NiO/MAPI interfaces. This observation excludes scenario (a).

To test whether and what kind of a space charge forms at the interface between MAPI and NiO, the conductivities of a MAPI film and a NiO:MAPI film are mea-

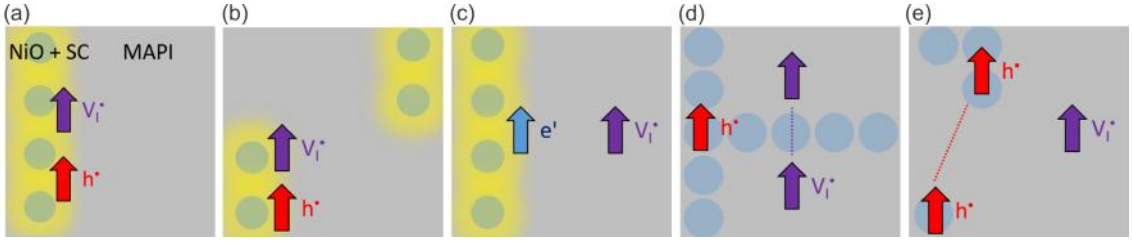

Figure 3.55: Hypothesis about charge carrier conduction in NiO:MAPI composite films. (a) The accumulation space charge is formed at the interface between NiO/MAPI. (b) Same as (a) but without percolation of NiO in MAPI. (c) Inversion space charge formation between NiO and MAPI. (d) Only percolating of NiO for electronic transfer. (e) Same as (d) but without percolation.

sured under different iodine partial pressure conditions. Under Ar conditions (very low iodine partial pressure), NiO:MAPI exhibited a factor of 8 higher electronic conductivity compared to MAPI, while both films showed similar ionic conductivity.

At high iodine partial pressure ($p(I_2) = 4.6$ μbar), both films exhibited similar ionic conductivities compared to the Ar conditions (approximately 10^{-8} S/cm), while both electronic conductivities increased by approximately a factor of $\times 100$. This result indicates that both films are operating in the p-type conducting regime, suggesting that no inversion is present in proximity of the oxide's surface, hence excluding scenario (c). Although the NiO:MAPI film still showed slightly higher electronic conductivity, the difference between the two values decreased (approximately a factor of 2). Based on this analysis, such larger conductivity could be due to a direct contribution of the oxide particles to the conduction of holes in the films (Figure 3.55 (d) or (e)), or to a non-percolating accumulation space charge largeat the MAPI:NiO interface (Figure 3.55 (b)) .

Upon increasing the iodine partial pressure to $p(I_2) = 17$ μbar, a slight decrease in ionic conductivity and an increase in electronic conductivity are observed for MAPI compared to the measurement at lower iodine partial pressures. Note that there is a large error in the estimate of the ionic conductivity under such conditions, where electronic conduction dominates the electrical response of the sample.

Interestingly, the NiO:MAPI case exhibited slightly higher ionic conductivities com-

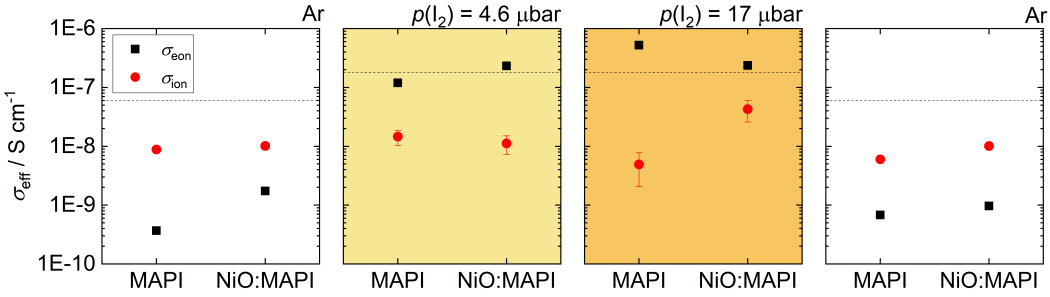

Figure 3.56: Ionic and electronic conductivities measured for MAPI and NiO:MAPI thin films in argon and at different iodine partial pressures.

pared to MAPI, while its electronic conductivity is lower than for MAPI under these conditions. The results seem to suggest that, the factor allowing for the NiO:MAPI film to possess a larger electronic conductivity than MAPI at low $p(I_2)$ is no longer active when the films are measured at high values of $p(I_2)$. Below, I discuss this result further, based on measurements of pure NiO. Upon returning to an Ar atmosphere, both films demonstrated reversibility in their conductivity behavior, confirming that the films are measured within their reversibility window.

The E_a of both films is measured at a fixed $p(I_2)$. It is found that NiO:MAPI film exhibited a lower E_a for electronic conductivity than MAPI, while the ionic conductivity showed the opposite trend. If these changes were solely caused by space charge effects (as per scenario (a)), a similar change would be expected for both ionic and electronic conductivity upon inclusion of the NiO particles, because holes and iodide vacancies would be similarly affected by an interfacial space charge. However, based on these results, it is clear that NiO facilitates the transport of electronic charge carriers within the composite and no percolating accumulation space charge is present for the ionic charge carriers.

In terms of ionic conductivity at low temperatures, both MAPI and NiO:MAPI films showed similar values (4×10^{-6} S/cm). However, at high temperatures (*e.g.*, 60 °C), NiO:MAPI exhibited a higher ionic conductivity compared to MAPI by a factor of 2. When measuring the sample at the lowest temperature again, irreversible behavior is observed, indicating possible irreversible reaction with iodine at high

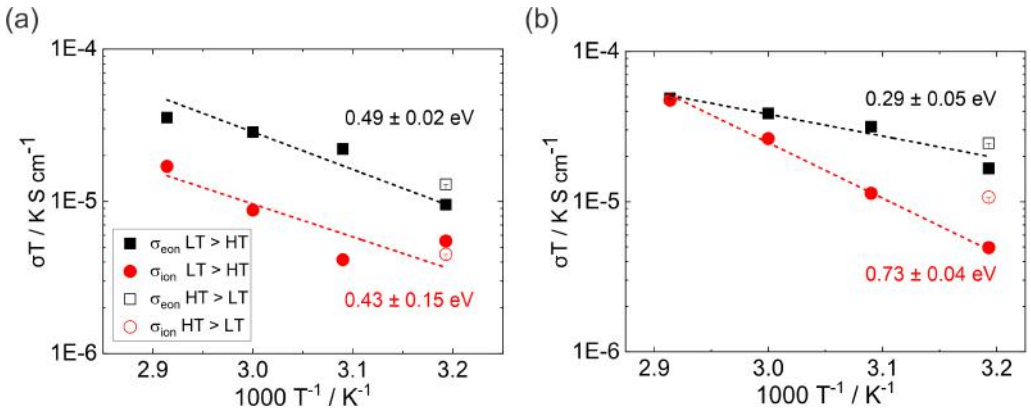

Figure 3.57: Activation energy measurement result of (a) MAPI and (b) NiO:MAPI at $p(I_2) = 0.7$ μbar

temperatures. This reaction increases the hole concentration in the NiO under high temperature exposure to iodine containing gas. While there is no clear explanation for the ionic conductivity increase in the sample, this observation may be the result of the formation of a hole and iodide vacancy accumulation layer at the NiO:MAPI interface on increase of the NiO work function (based on electronic equilibration at the interface). Such increase in work function should however occur in MAPI too, making this hypothesis not definitive. Note that when considering this irreversible behavior, the activation energy associated with the electronic conductivity is reduced further, while the one related with the ionic conductivity becomes similar (within error) to the value extracted for MAPI.

To clarify the conductivity changes of NiO under higher iodine pressure and temperature, a NiO pellet is pressed and its conductivity is measured under varying iodine partial pressure and temperature conditions, following the same protocol as the one described above. The conductivity of NiO remained relatively unchanged up to a certain iodine partial pressure of $p(I_2) = 0.3$ μbar. However, when the iodine partial pressure is increased to $p(I_2) = 5$ μbar, the conductivity increased by a factor of 4. Upon returning the sample to an argon condition, no reversible behavior is observed. Furthermore, significant conductivity changes were observed when the sample is subjected to multiple temperature scans while maintaining the same iodine

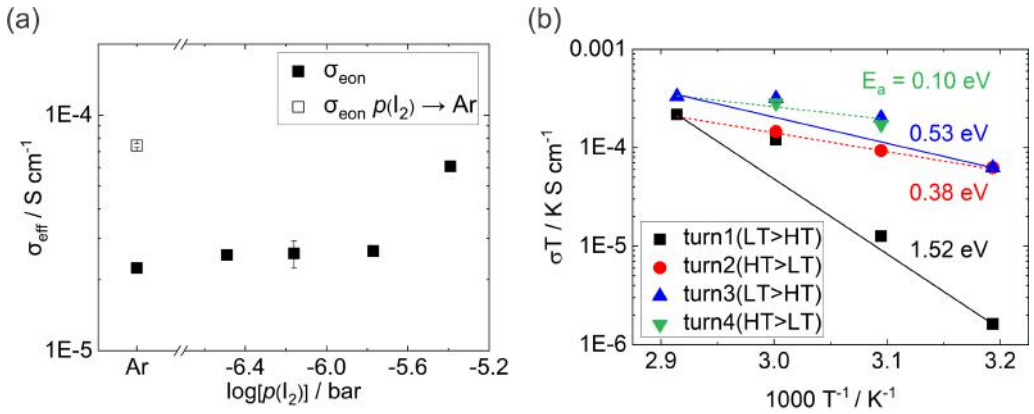

Figure 3.58: (a) NiO pellet conductivity measurement in different iodine partial pressure. (b) E_a measurement of NiO pellet at $p(I_2) = 0.7$ μbar

partial pressure. The conductivity exhibited an activation energy of 1.74 eV during the first transition from low to high temperature. Interestingly, when the sample is returned to a low temperature, the increased conductivity is maintained, but with a decreased activation energy ranging from 0.10 to 0.38 eV. This result confirms that iodine gas can p-dope NiO at high iodine partial pressure and temperature, resulting in increased conductivity, a process that is largely irreversible when returning to low $p(I_2)$ values.

Finally, the product of the conductivity measured for the NiO pellet (approximately 10^{-7} S/cm) and the volume fraction of NiO particles used to collect the data in Figure 3.58 supports the hypothesis that the NiO particles are largely responsible for the conductivity observed in the composite films investigated here, while MAPI may still assist in connecting the individual particles within the composite. Because of the unchanged ionic conductivity up to 3 vol% of NiO in MAPI, scenario (d) or (e) is the most likely. Furthermore, Figure 3.58 shows that when the composite films electronic conductivity reaches the same order of magnitude as measured for pure NiO at high $p(I_2)$, its value does not change as much. This indicates that the particles may have a significant blocking effect once their conductivity is lower than the MAPI host phase, pointing towards (d), as the most likely scenario (also consistent with E_a measurements). Under this condition, a space charge potential

on the NiO side is still possible to compensate for the difference in the materials' work functions. Notably, the small size of the NiO particles could mean that these are fully depleted from holes, assuming not too high background acceptor dopant concentration.

3.4.4 Conclusions

In this chapter, space charge effects are investigated at selected MAPI:oxide interfaces, including insulating oxides (SiO_2 and MgO) and p-type semiconducting NiO. The electrical response of composite films was measured, in order to gain a generalized understanding of ionically-induced space charge formation in MAPI based systems.

In the first part of the chapter, ionically-generated space charges are demonstrated for SiO_2:MAPI and MgO:MAPI composite films showing that such phenomenon is not exclusive to alumina, but it is rather a general effect. SiO_2:MAPI films shows rougher morphology compared with MAPI, similar to alumina:MAPI composite films. MgO:MAPI films show a smooth surface and smaller crystal size compared with MAPI. The electronic and ionic conductivity measurements on alumina:MAPI composite films reproduce the results presented in Chapter 3.1. The electronic conductivity trend in the SiO_2:MAPI film case follows similar behavior as the alumina:MAPI, suggesting a similar cation adsorption process inducing an ionically-generated space charge at this interface. The analysis of ionic conductivity is more challenging due to the presence of multiple features in impedance spectra. While when considering the high frequency feature for the total conductivity at high $p(I_2)$ leads to an increased ionic conductivity in the SiO_2:MAPI film with respect to the argon case, it is possible that electronic conduction may dominate the whole response, whereby the high-frequency and low frequency features may be associated with conduction within the grains and the contribution of grain boundaries, respectively. For an accurate ionic conductivity extraction, further measurements under lower iodine partial pressure or examination of different oxide particle concentrations

would be required.

In the MgO:MAPI film case, both electronic and ionic conductivity under argon are decreased compared with MAPI. The electronic conductivity is increased by iodine partial pressure increase in the system by a similar factor as for the MAPI case. This suggests that, in this composite film, conduction occurs in the bulk of MAPI, and some blocking effect by the insulating particles (MgO) partially hinders electronic and ionic transport. No evidence for significant space charges at the MgO:MAPI interface is recorded.

These results are more consistent with the zeta potential investigation carried out in some of the electrolytes with similar compositions as the MAPI precursor solution, while they show a very different trend compared with the literature point of zero charge. This emphasizes the importance of specific interactions between surface and ionic species at play when predicting anion or cation adsorption trends.

In the second part of this chapter, I examined the NiO:MAPI interface, as an example where electronic and ionic equilibrium of the two contacting phase would result in opposite signs of the interfacial space charge potential. Based on the work function difference between NiO and MAPI, an accumulation of holes in the MAPI side is expected when the two materials are put in contact, while based on the oxides point of zero charge and zeta potential, depletion of iodide vacancies (and therefore holes) would be expected. By increasing the NiO particle concentration in the composite film, the electronic conductivity is increased compared with pure MAPI, suggesting a major contribution of the oxide to the measured response. This contribution becomes less evident and the opposite trend is observed when high $p(I_2)$ are considered. Under such conditions, the conductivity in MAPI within the composite is expected to be larger than in NiO. These results suggest good coverage of the NiO particles around the MAPI grains. The E_a associated with the electronic conduction in the NiO:MAPI film was lower than the same quantity measured for MAPI, confirming that NiO forms percolating pathways for electronic charge carriers in the film. Since the measured ionic conductivity is relatively constant across

the investigated NiO vol% range, the absence of a significant space charge at the MAPI:NiO interface is inferred. Finally, conductivity measurements performed on a NiO pellet showed oxidation of the oxide under high temperature and high iodine partial pressure condition, which could at least partially explain the irreversible behavior observed for temperature dependent measurements of NiO:MAPI films.

These results show that no significant space charge at the NiO/MAPI interface forms on the MAPI side within the investigated composite films. This could be due to the contribution of electronic effects reducing ionic interactions (*e.g.* hole concentration in NiO may be comparable with iodide vacancy concentration in MAPI). Possible hole depletion of the NiO particles would reduce such contribution, which would suggest that no significant ionic adsorption occurs at this interface, despite the large and positive zeta potential value in $Pb(NO_3)_2$ electrolytes.

4 Conclusions

This thesis represents a systematic study of ion redistribution at the interface of MAPI with different contacting materials and its impact on space charge formation. Composite films and mesoporous structures with direct relevance to optoelectronic devices have been investigated, with special focus on the role of the contact material surface properties and on the development of strategies to modulate the interfacial interactions via surface modification using organic molecules. Testing of solar cells was carried out to correlate the results on the ionic contribution to space charge formation with device behavior and performance. The following main findings resulted from my work:

- Embedding of alumina nanoparticles within MAPI results in enhancement of electronic conductivity under low iodine partial pressures, which is interpreted in terms of ionically-generated space charge effects at the interface between the two materials, consistent with previous report from our group. The effect is attributed to Pb cation adsorption on the surface of alumina and the formation of an inversion space charge region.

- I have demonstrated that such effect can be reduced by modifying alumina with organic molecules that bind chemically on the surface of the oxide. Reduction of the space charge potential from 840 mV for bare alumina to 740 mV for MeO-2PACz modified alumina and 160 mV for BPA modified alumina. The trend between the two molecules is explained based on their relative size: the smaller BPA forms a more closely packed monolayer on the oxide, pre-

venting the adsorption of cation to a larger extent than MeO-2PACz. These findings are supported by activation energy and zeta potential measurements. The results show that controlling surface interactions with mobile ionic defects is an effective strategy to modulate space charge potentials at interfaces.

- The presence of a space charge region at the interface between TiO_2 and MAPI was demonstrated for the case of mesoporous films infiltrated with the perovskite. An inversion layer within the pores determines the electronic conductivity under low iodine partial pressures. By assuming a pore size of 25 nm in mesoporous structure and an acceptor dopant concentration of $[A'] = 10^{18}$ cm^{-3} for the MAPI samples, the results point towards nanoionics effects being important in the analysis of these mesoscopic structures.

- Measurements of activation energy of transport support this results. These results imply that accounting for nanoionics effects is essential in order to comprehend the space charge behavior within mesoporous structures of halide perovskite-based devices. Such space charge effects are less affected by surface modification compared with the alumina case. This can be related with a different adsorption mechanism of the molecules on the two oxides, or to a dominant electronic equilibration contribution determining the space charge equilibrium of MAPI with TiO_2.

- The use of oxide:MAPI composite active layers in solar cell, also for the case of surface modified oxides was tested. First, guidelines on the characterization of mixed conductivity in vertical device architecture are established. The use of spiro-OMeTAD as hole transporting material does not pose any limitation in the measurement of the electronic conductivity of MAPI. Interestingly, from the iodine partial pressure dependence of the conductivity of this hole transporter, it is clear that equilibration with MAPI within common devices is expected with a possible increase in the doping level even in already doped films. The study of conductivity and solar cell performance for solar cells including

composite films confirms the presence of a distributed p-n junction within the active layer. This is proven detrimental to the solar cell performance, possibly because of the already sufficiently long diffusion length for charge carriers in MAPI, making additional strategies for charge separation ineffective. Such reduction in performance is partially mitigated when surface modification is used, consistent with the conclusion above. Finally, mesoporous structure and surface modification is studied. This result shows largely unvaried behavior of the MAPI/TiO_2 interface with or without the BPA modification, consistent with the similar space charge expected for this material combination.

- The picture of ionically-generated space charge is generalized to SiO_2 insulating particles, while MgO did not show any pronounced interfacial effect. These results are in contrast with literature point of zero charge values emphasizing the importance of specific interactions and possibly other effects related to film formation and differences between solid and liquid state surface chemistry. In addition to this, to extend knowledge to ionic space charge at the interfaces between electronic conducting oxide and MAPI, hole transporting oxide NiO is used. In NiO:MAPI composite films, the electronic conductivity is increased compared with pure MAPI, while the ionic conductivity is largely unvaried. This suggests a major contribution of the oxide to the measured response and a negligible space charge forming at this interface. It was also found that high iodine partial pressure may induce the oxidation of NiO, also contributing to changes in the measured conductivity.

This thesis suggests new parameters for designing devices that utilize MAPI, possibly applicable to other hybrid perovskite compositions. Especially, when employing surface modification techniques, it is crucial to consider how surface modifiers block ions or interact with specific mobile ionic defects, which could change the space charge formation at the interface with MAPI. Understanding ionic space charge effect could ultimately contribute to the development of more efficient and stable

halide perovskite based devices.

Bibliography

[1] Johannes M Richter et al. "Enhancing photoluminescence yields in lead halide perovskites by photon recycling and light out-coupling". *Nature communications* 7.1 (2016), 13941.

[2] Stefaan De Wolf et al. "Organometallic halide perovskites: sharp optical absorption edge and its relation to photovoltaic performance". *The journal of physical chemistry letters* 5.6 (2014), 1035–1039.

[3] Hui-Seon Kim et al. "Lead iodide perovskite sensitized all-solid-state submicron thin film mesoscopic solar cell with efficiency exceeding 9%". *Scientific reports* 2.1 (2012), 591.

[4] Samuel D Stranks et al. "Electron-hole diffusion lengths exceeding 1 micrometer in an organometal trihalide perovskite absorber". *Science* 342.6156 (2013), 341–344.

[5] Christian Wehrenfennig et al. "High charge carrier mobilities and lifetimes in organolead trihalide perovskites". *Advanced materials* 26.10 (2014), 1584–1589.

[6] Jarvist Moore Frost. "Calculating polaron mobility in halide perovskites". *Physical Review B* 96.19 (2017), 195202.

[7] Youngho Kang and Seungwu Han. "Intrinsic carrier mobility of cesium lead halide perovskites". *Physical Review Applied* 10.4 (2018), 044013.

[8] Tom J Savenije et al. "Thermally activated exciton dissociation and recom-

bination control the carrier dynamics in organometal halide perovskite". *The journal of physical chemistry letters* 5.13 (2014), 2189–2194.

[9] Jongchul Lim et al. "Elucidating the long-range charge carrier mobility in metal halide perovskite thin films". *Energy & Environmental Science* 12.1 (2019), 169–176.

[10] Yaoguang Rong et al. "Challenges for commercializing perovskite solar cells". *Science* 361.6408 (2018), eaat8235.

[11] Juan-Pablo Correa-Baena et al. "Promises and challenges of perovskite solar cells". *Science* 358.6364 (2017), 739–744.

[12] Leiping Duan et al. "Stability challenges for the commercialization of perovskite–silicon tandem solar cells". *Nature Reviews Materials* (2023), 1–21.

[13] Henry J Snaith et al. "Anomalous hysteresis in perovskite solar cells". *The journal of physical chemistry letters* 5.9 (2014), 1511–1515.

[14] Stefan AL Weber et al. "How the formation of interfacial charge causes hysteresis in perovskite solar cells". *Energy & Environmental Science* 11.9 (2018), 2404–2413.

[15] Daniel J Slotcavage, Hemamala I Karunadasa, and Michael D McGehee. "Light–induced phase segretation in halide perovskite absorbers". *ACS Energy Letters* 1.6 (2016), 1199–1205.

[16] Xiaofeng Tang et al. "Local observation of phase segregation in mixed-halide perovskite". *Nano letters* 18.3 (2018), 2172–2178.

[17] Konrad Domanski et al. "Systematic investigation of the impact of operation conditions on the degradation behaviour of perovskite solar cells". *Nature Energy* 3.1 (2018), 61–67.

[18] Arthur Julien, Jean-Baptiste Puel, and Jean-Francois Guillemoles. "Distinction of mechanisms causing experimental degradation of perovskite solar

cells by simulating associated pathways". *Energy and Environmental Science* (2023).

[19] Moritz H Futscher et al. "Quantification of ion migration in CH 3 NH 3 PbI 3 perovskite solar cells by transient capacitance measurements". *Materials Horizons* 6.7 (2019), 1497–1503.

[20] Wolfgang Tress. "Metal Halide Perovskites as Mixed Electronic–Ionic Conductors: Challenges and Opportunities From Hysteresis to Memristivity". *The journal of physical chemistry letters* 8.13 (2017), 3106–3114.

[21] Sapir Bitton and Nir Tessler. "Electron/hole blocking layers as ionic blocking layers in perovskite solar cells". *Journal of Materials Chemistry C* 9.6 (2021), 1888–1894.

[22] Nam Joong Jeon et al. "Compositional engineering of perovskite materials for high-performance solar cells". *Nature* 517.7535 (2015), 476–480.

[23] Michael Saliba et al. "Incorporation of rubidium cations into perovskite solar cells improves photovoltaic performance". *Science* 354.6309 (2016), 206–209.

[24] Silver-Hamill Turren-Cruz, Anders Hagfeldt, and Michael Saliba. "Methylammonium-free, high-performance, and stable perovskite solar cells on a planar architecture". *Science* 362.6413 (2018), 449–453.

[25] Seog Joon Yoon, Kevin G Stamplecoskie, and Prashant V Kamat. "How lead halide complex chemistry dictates the composition of mixed halide perovskites". *The journal of physical chemistry letters* 7.7 (2016), 1368–1373.

[26] Giles E Eperon et al. "The role of dimethylammonium in bandgap modulation for stable halide perovskites". *ACS Energy Letters* 5.6 (2020), 1856–1864.

[27] Dieter Weber. "CH3NH3PbX3, ein Pb(II)- mit kubischer Perowskitstruktur / CH3NH3PbX3, a Pb(II)-System with Cubic Perovskite Structure". *Zeitschrift für Naturforschung B* 33.12 (1978), 1443–1445.

[28] Akihiro Kojima et al. "Organometal Halide Perovskites as Visible-Light Sensitizers for Photovoltaic Cells". *Journal of the American Chemical Society* 131.17 (2009), 6050–6051.

[29] Alessandro Senocrate and Joachim Maier. "Solid-state ionics of hybrid halide perovskites". *Journal of the American Chemical Society* 141.21 (2019), 8382–8396.

[30] Yongbo Yuan and Jinsong Huang. "Ion migration in organometal trihalide perovskite and its impact on photovoltaic efficiency and stability". *Accounts of chemical research* 49.2 (2016), 286–293.

[31] Davide Moia and Joachim Maier. "Ion transport, defect chemistry, and the device physics of hybrid perovskite solar cells". *ACS Energy Letters* 6.4 (2021), 1566–1576.

[32] Tae-Youl Yang et al. "The significance of ion conduction in a hybrid organic–inorganic lead-iodide-based perovskite photosensitizer". *Angewandte Chemie* 127.27 (2015), 8016–8021.

[33] Alessandro Senocrate et al. "The nature of ion conduction in methylammonium lead iodide: a multimethod approach". *Angewandte Chemie* 129.27 (2017), 7863–7867.

[34] Davide Moia and Joachim Maier. "Ionic and electronic energy diagrams for hybrid perovskite solar cells". *Materials Horizons* (2023).

[35] Junichiro Mizusaki, Kimiyasu Arai, and Kazuo Fueki. "Ionic conduction of the perovskite-type halides". *Solid State Ionics* 11.3 (1983), 203–211.

[36] Cheng Li et al. "Unravelling the role of vacancies in lead halide perovskite through electrical switching of photoluminescence". *Nature communications* 9.1 (2018), 5113.

[37] Masoud Ghasemi et al. "A multiscale ion diffusion framework sheds light on the diffusion–stability–hysteresis nexus in metal halide perovskites". *Nature*

Materials (2023), 1–9.

[38] Jun Haruyama et al. “First-principles study of ion diffusion in perovskite solar cell sensitizers”. *Journal of the American Chemical Society* 137.32 (2015), 10048–10051.

[39] Christopher Eames et al. “Ionic transport in hybrid lead iodide perovskite solar cells”. *Nature communications* 6.1 (2015), 7497.

[40] Jongseob Kim et al. “The role of intrinsic defects in methylammonium lead iodide perovskite”. *The journal of physical chemistry letters* 5.8 (2014), 1312–1317.

[41] Aron Walsh et al. “Self-regulation mechanism for charged point defects in hybrid halide perovskites”. *Angewandte Chemie* 127.6 (2015), 1811–1814.

[42] Alessandro Senocrate et al. “Charge carrier chemistry in methylammonium lead iodide”. *Solid State Ionics* 321 (2018), 69–74.

[43] Joachim Maier. “Defect chemistry: composition, transport, and reactions in the solid state; part I: thermodynamics”. *Angewandte Chemie International Edition in English* 32.3 (1993), 313–335.

[44] Joachim Maier. *Physical chemistry of ionic materials: ions and electrons in solids*. John Wiley & Sons, 2023.

[45] Simon M Sze, Yiming Li, and Kwok K Ng. *Physics of semiconductor devices*. John wiley & sons, 2021.

[46] Xiangxin Guo and Joachim Maier. “Comprehensive modeling of ion conduction of nanosized CaF2/BaF2 multilayer heterostructures”. *Advanced Functional Materials* 19.1 (2009), 96–101.

[47] Dirk Zahn et al. “Molecular Dynamics Modeling of Nanoscale CaF2/BaF2 Heterolayer Structures”. *The Journal of Physical Chemistry C* 113.4 (2009), 1315–1319.

[48] Joachim Maier. “Ionic transport in nano-sized systems”. *Solid State Ionics* 175.1-4 (2004), 7–12.

[49] Sangtae Kim, Jürgen Fleig, and Joachim Maier. “Space charge conduction: Simple analytical solutions for ionic and mixed conductors and application to nanocrystalline ceria”. *Physical Chemistry Chemical Physics* 5.11 (2003), 2268–2273.

[50] Joachim Maier. “Space charge effects in confined ceramic systems”. *International journal of materials research* 99.1 (2008), 24–25.

[51] Xiangxin Guo et al. “Defect chemical modeling of mesoscopic ion conduction in nanosized Ca F 2/ Ba F 2 multilayer heterostructures”. *Physical Review B* 76.12 (2007), 125429.

[52] Chuanlian Xiao, Chia-Chin Chen, and Joachim Maier. “Discrete modeling of ionic space charge zones in solids”. *Physical Chemistry Chemical Physics* 24.19 (2022), 11945–11957.

[53] Robert Usiskin and Joachim Maier. “Interfacial effects in lithium and sodium batteries”. *Advanced Energy Materials* 11.2 (2021), 2001455.

[54] Hanul Min et al. “Perovskite solar cells with atomically coherent interlayers on SnO2 electrodes”. *Nature* 598.7881 (2021), 444–450.

[55] Tomas Leijtens et al. “Stability of metal halide perovskite solar cells”. *Advanced Energy Materials* 5.20 (2015), 1500963.

[56] Teddy Salim et al. “Perovskite-based solar cells: impact of morphology and device architecture on device performance”. *Journal of Materials Chemistry A* 3.17 (2015), 8943–8969.

[57] Junsang Cho et al. “Suppressed halide ion migration in 2D lead halide perovskites”. *ACS Materials Letters* 2.6 (2020), 565–570.

[58] Jean-Christophe Blancon et al. “Semiconductor physics of organic–inorganic 2D halide perovskites”. *Nature nanotechnology* 15.12 (2020), 969–985.

[59] Carmen Ortiz-Cervantes, Paulina Carmona-Monroy, and Diego Solis-Ibarra. "Two-dimensional halide perovskites in solar cells: 2D or not 2D?". *ChemSusChem* 12.8 (2019), 1560–1575.

[60] Rongrong Cheacharoen et al. "Design and understanding of encapsulated perovskite solar cells to withstand temperature cycling". *Energy & Environmental Science* 11.1 (2018), 144–150.

[61] Francesca Corsini and Gianmarco Griffini. "Recent progress in encapsulation strategies to enhance the stability of organometal halide perovskite solar cells". *Journal of Physics: Energy* 2.3 (2020), 031002.

[62] Julie Euvrard, Yanfa Yan, and David B Mitzi. "Electrical doping in halide perovskites". *Nature Reviews Materials* 6.6 (2021), 531–549.

[63] Davide Regaldo et al. "On the equilibrium electrostatic potential and light-induced charge redistribution in halide perovskite structures". *Progress in Photovoltaics: Research and Applications* 30.8 (2022), 994–1002.

[64] Severin N Habisreutinger, Nakita K Noel, and Henry J Snaith. "Hysteresis index: A figure without merit for quantifying hysteresis in perovskite solar cells". *ACS Energy Letters* 3.10 (2018), 2472–2476.

[65] Stephan van Reenen, Martijn Kemerink, and Henry J Snaith. "Modeling anomalous hysteresis in perovskite solar cells". *The journal of physical chemistry letters* 6.19 (2015), 3808–3814.

[66] Wolfgang Tress et al. "Understanding the rate-dependent J–V hysteresis, slow time component, and aging in CH 3 NH 3 PbI 3 perovskite solar cells: the role of a compensated electric field". *Energy & Environmental Science* 8.3 (2015), 995–1004.

[67] Eva Lisa Unger et al. "Hysteresis and transient behavior in current–voltage measurements of hybrid-perovskite absorber solar cells". *Energy & Environmental Science* 7.11 (2014), 3690–3698.

[68] Isaac Zarazua, Juan Bisquert, and Germà Garcia-Belmonte. "Light-induced space-charge accumulation zone as photovoltaic mechanism in perovskite solar cells". *The journal of physical chemistry letters* 7.3 (2016), 525–528.

[69] Jiangang Hu et al. "Photovoltage behavior in perovskite solar cells under light-soaking showing photoinduced interfacial changes". *ACS Energy Letters* 2.5 (2017), 950–956.

[70] Daniele Meggiolaro, Edoardo Mosconi, and Filippo De Angelis. "Formation of surface defects dominates ion migration in lead-halide perovskites". *ACS Energy Letters* 4.3 (2019), 779–785.

[71] Andrés-Felipe Castro-Méndez, Juanita Hidalgo, and Juan-Pablo Correa-Baena. "The role of grain boundaries in perovskite solar cells". *Advanced Energy Materials* 9.38 (2019), 1901489.

[72] Jae S Yun et al. "Critical role of grain boundaries for ion migration in formamidinium and methylammonium lead halide perovskite solar cells". *Advanced Energy Materials* 6.13 (2016), 1600330.

[73] Adam Pockett et al. "Microseconds, milliseconds and seconds: deconvoluting the dynamic behaviour of planar perovskite solar cells". *Physical Chemistry Chemical Physics* 19.8 (2017), 5959–5970.

[74] Davide Moia et al. "Ionic-to-electronic current amplification in hybrid perovskite solar cells: ionically gated transistor-interface circuit model explains hysteresis and impedance of mixed conducting devices". *Energy & Environmental Science* 12.4 (2019), 1296–1308.

[75] Daniel A Jacobs et al. "The two faces of capacitance: New interpretations for electrical impedance measurements of perovskite solar cells and their relation to hysteresis". *Journal of Applied Physics* 124.22 (2018), 225702.

[76] Firouzeh Ebadi et al. "Origin of apparent light-enhanced and negative capacitance in perovskite solar cells". *Nature communications* 10.1 (2019), 1574.

[77] Young Chan Kim et al. “Beneficial effects of PbI2 incorporated in organo-lead halide perovskite solar cells”. *Advanced Energy Materials* 6.4 (2016), 1502104.

[78] Mojtaba Abdi-Jalebi et al. “Maximizing and stabilizing luminescence from halide perovskites with potassium passivation”. *Nature* 555.7697 (2018), 497–501.

[79] Dae-Yong Son et al. “Universal approach toward hysteresis-free perovskite solar cell via defect engineering”. *Journal of the American Chemical Society* 140.4 (2018), 1358–1364.

[80] Hsin-Wei Chen et al. “Emergence of hysteresis and transient ferroelectric response in organo-lead halide perovskite solar cells”. *The journal of physical chemistry letters* 6.1 (2015), 164–169.

[81] Jarvist M Frost, Keith T Butler, and Aron Walsh. “Molecular ferroelectric contributions to anomalous hysteresis in hybrid perovskite solar cells”. *Apl Materials* 2.8 (2014), 081506.

[82] Gee Yeong Kim et al. “Ionically Generated Built-In Equilibrium Space Charge Zonesa Paradigm Change for Lead Halide Perovskite Interfaces”. *Advanced Functional Materials* 30.31 (2020), 2002426.

[83] Nico Leupold et al. “Electrical conductivity of halide perovskites follows expectations from classical defect chemistry”. *European Journal of Inorganic Chemistry* 2021.28 (2021), 2882–2889.

[84] Louis J Gillespie and Lewis HD Fraser. “The normal vapor pressure of crystalline iodine1”. *Journal of the American Chemical Society* 58.11 (1936), 2260–2263.

[85] Davide Moia et al. “Ionic and electronic polarization effects in horizontal hybrid perovskite device structures close to equilibrium”. *Physical Chemistry Chemical Physics* 25.19 (2023), 13335–13350.

[86] Ganbaatar Tumen-Ulzii et al. “Hysteresis-less and stable perovskite solar cells with a self-assembled monolayer”. *Communications Materials* 1.1 (2020), 31.

[87] Xiang Deng et al. “Co-assembled Monolayers as Hole-Selective Contact for High-Performance Inverted Perovskite Solar Cells with Optimized Recombination Loss and Long-Term Stability”. *Angewandte Chemie International Edition* 61.30 (2022), e202203088.

[88] Konrad Wojciechowski et al. “Heterojunction modification for highly efficient organic–inorganic perovskite solar cells”. *ACS nano* 8.12 (2014), 12701–12709.

[89] Kyoungwon Choi et al. “A short review on interface engineering of perovskite solar cells: a self-assembled monolayer and its roles”. *Solar RRL* 4.2 (2020), 1900251.

[90] Ahmed Farag et al. “Evaporated Self-Assembled Monolayer Hole Transport Layers: Lossless Interfaces in p-i-n Perovskite Solar Cells”. *Advanced Energy Materials* 13.8 (2023), 2203982.

[91] Nga Phung et al. “Enhanced Self-Assembled Monolayer Surface Coverage by ALD NiO in pin Perovskite Solar Cells”. *ACS Applied Materials & Interfaces* 14.1 (2021), 2166–2176.

[92] Juanjuan Sun et al. “NiOx-seeded self-assembled monolayers as highly hole-selective passivating contacts for efficient inverted perovskite solar cells”. *Solar RRL* 5.11 (2021), 2100663.

[93] Amran Al-Ashouri et al. “Conformal monolayer contacts with lossless interfaces for perovskite single junction and monolithic tandem solar cells”. *Energy & Environmental Science* 12.11 (2019), 3356–3369.

[94] Donghoon Song et al. “Interfacial engineering with a hole-selective self-assembled monolayer for tin perovskite solar cells via a two-step fabrication”. *ACS Energy Letters* 6.12 (2021), 4179–4186.

[95] Jimmy Mangalam et al. “Modification of NiOx hole transport layers with 4-bromobenzylphosphonic acid and its influence on the performance of lead halide perovskite solar cells”. *Journal of Materials Science: Materials in Electronics* 30.10 (2019), 9602–9611.

[96] Lukas Zeininger et al. “Quantitative determination and comparison of the surface binding of phosphonic acid, carboxylic acid, and catechol ligands on TiO2 nanoparticles”. *Chemistry–A European Journal* 22.38 (2016), 13506–13512.

[97] Peter Thissen, Markus Valtiner, and Guido Grundmeier. “Stability of phosphonic acid self-assembled monolayers on amorphous and single-crystalline aluminum oxide surfaces in aqueous solution”. *Langmuir* 26.1 (2010), 156–164.

[98] Ibram Ganesh et al. “Chemisorption of phosphoric acid and surface characterization of as passivated AlN powder against hydrolysis”. *Langmuir* 24.10 (2008), 5359–5365.

[99] Rebecca BM Hill et al. “Phosphonic acid modification of the electron selective contact: interfacial effects in perovskite solar cells”. *ACS Applied Energy Materials* 2.4 (2019), 2402–2408.

[100] Robert Withnall and Lester Andrews. “FTIR spectra of the photolysis products of the phosphine-ozone complex in solid argon”. *Journal of Physical Chemistry* 91.4 (1987), 784–797.

[101] Joachim Maier. “Enhancement of the Ionic Conductivity in Solid-Solid-Dispersions by Surface Induced Defects”. *Berichte der Bunsengesellschaft für physikalische Chemie* 88.11 (1984), 1057–1062.

[102] Tae-Hee Han et al. “Perovskite-polymer composite cross-linker approach for highly-stable and efficient perovskite solar cells”. *Nature communications* 10.1 (2019), 520.

[103] Giulia Longo et al. "Highly luminescent perovskite–aluminum oxide composites". *Journal of Materials Chemistry C* 3.43 (2015), 11286–11289.

[104] Brian O'regan and Michael Grätzel. "A low-cost, high-efficiency solar cell based on dye-sensitized colloidal TiO2 films". *nature* 353.6346 (1991), 737–740.

[105] Fabrizio Giordano et al. "Enhanced electronic properties in mesoporous TiO2 via lithium doping for high-efficiency perovskite solar cells". *Nature communications* 7.1 (2016), 10379.

[106] Hui-Seon Kim and Nam-Gyu Park. "Parameters affecting I–V hysteresis of CH3NH3PbI3 perovskite solar cells: effects of perovskite crystal size and mesoporous TiO2 layer". *The journal of physical chemistry letters* 5.17 (2014), 2927–2934.

[107] Tomas Leijtens et al. "The importance of perovskite pore filling in organometal mixed halide sensitized TiO2-based solar cells". *The journal of physical chemistry letters* 5.7 (2014), 1096–1102.

[108] Diana Nanova et al. "Unraveling the nanoscale morphologies of mesoporous perovskite solar cells and their correlation to device performance". *Nano letters* 14.5 (2014), 2735–2740.

[109] Byung-wook Park et al. "Enhanced crystallinity in organic–inorganic lead halide perovskites on mesoporous TiO2 via disorder–order phase transition". *Chemistry of Materials* 26.15 (2014), 4466–4471.

[110] Carlito S Ponseca Jr et al. "Organometal halide perovskite solar cell materials rationalized: ultrafast charge generation, high and microsecond-long balanced mobilities, and slow recombination". *Journal of the American Chemical Society* 136.14 (2014), 5189–5192.

[111] J Maier. *Nano-ionics: Trivial and non-trivial size effects on ion conduction in solids*. 2003.

[112] J Maier. “Nanoionics: ion transport and electrochemical storage in confined systems”. *Nature materials* 4.11 (2005), 805–815.

[113] Chi Huey Ng et al. “Tunable open circuit voltage by engineering inorganic cesium lead bromide/iodide perovskite solar cells”. *Scientific reports* 8.1 (2018), 1–9.

[114] Yoshitaka Sanehira et al. “Low-temperature synthesized Nb-doped TiO2 electron transport layer enabling high-efficiency perovskite solar cells by band alignment tuning”. *ACS applied materials & interfaces* 12.13 (2020), 15175–15182.

[115] Davide Moia et al. “Dye Monolayers Used as the Hole Transporting Medium in Dye-Sensitized Solar Cells”. *Advanced Materials* 27.39 (2015), 5889–5894.

[116] Ross A Kerner et al. “Organic hole transport material ionization potential dictates diffusion kinetics of iodine species in halide perovskite devices”. *ACS Energy Letters* 6.2 (2021), 501–508.

[117] Jordi Carrillo et al. “Ionic reactivity at contacts and aging of methylammonium lead triiodide perovskite solar cells”. *Advanced Energy Materials* 6.9 (2016), 1502246.

[118] Ross A Kerner et al. “Organic hole transport material ionization potential dictates diffusion kinetics of iodine species in halide perovskite devices”. *ACS Energy Letters* 6.2 (2021), 501–508.

[119] Zhaojian Xu et al. “Origins of Photoluminescence Instabilities at Halide Perovskite/Organic Hole Transport Layer Interfaces”. *Journal of the American Chemical Society* (2023).

[120] Severin N Habisreutinger et al. “Investigating the Role of 4-Tert Butylpyridine in Perovskite Solar Cells”. *Advanced Energy Materials* 7.1 (2017), 1601079.

[121] Emilio J Juarez-Perez et al. “Role of the dopants on the morphological and transport properties of spiro-MeOTAD hole transport layer”. *Chemistry of*

Materials 28.16 (2016), 5702–5709.

[122] Tracy H Schloemer et al. "Doping strategies for small molecule organic hole-transport materials: impacts on perovskite solar cell performance and stability". *Chemical science* 10.7 (2019), 1904–1935.

[123] Gee Yeong Kim et al. "Large tunable photoeffect on ion conduction in halide perovskites and implications for photodecomposition". *Nature materials* 17.5 (2018), 445–449.

[124] Alessandro Senocrate et al. "Interaction of oxygen with halide perovskites". *Journal of Materials Chemistry A* 6.23 (2018), 10847–10855.

[125] Hirotoshi Yamada, Aninda J Bhattacharyya, and Joachim Maier. "Extremely high silver ionic conductivity in composites of silver halide (AgBr, AgI) and mesoporous alumina". *Advanced Functional Materials* 16.4 (2006), 525–530.

[126] J-S Lee, St Adams, and J Maier. "A mesoscopic heterostructure as the origin of the extreme ionic conductivity in AgI: Al2O3". *Solid State Ionics* 136 (2000), 1261–1266.

[127] George A Parks. "The isoelectric points of solid oxides, solid hydroxides, and aqueous hydroxo complex systems". *Chemical Reviews* 65.2 (1965), 177–198.

[128] Marek Kosmulski. "The pH dependent surface charging and points of zero charge. VIII. Update". *Advances in Colloid and Interface Science* 275 (2020), 102064.

[129] Wei Peng et al. "Reducing nonradiative recombination in perovskite solar cells with a porous insulator contact". *Science* 379.6633 (2023), 683–690.

[130] Gill Sang Han et al. "Retarding charge recombination in perovskite solar cells using ultrathin MgO-coated TiO 2 nanoparticulate films". *Journal of Materials Chemistry A* 3.17 (2015), 9160–9164.

[131] Joseph S Manser et al. “Making and breaking of lead halide perovskites”. *Accounts of chemical research* 49.2 (2016), 330–338.

Acknowledgments

I would like to express my sincere gratitude to Prof. Dr. Joachim Maier for providing me with the opportunity to study in this wonderful department. His guidance and support have been invaluable throughout my Ph.D. journey. I am truly grateful for his constant feedback and encouragement.

I would also like to extend my sincere appreciation to my committee members, Prof. Dr. Oliver Clemens and Prof. Dr. Rainer Niewa, for their valuable insights and contributions to my thesis. I believe their expertise and constructive feedback helps a lot in refining my work.

My appreciation goes to my daily supervisor, Dr. Davide Moia. I am grateful for his patient and passionate guidance throughout my Ph.D. journey. His support with everyday scientific discussion, technical expertise, and dedication to my growth as a researcher have been invaluable.

I express my gratitude to Madeleine Burkhardt for continuous support in handling administrative tasks throughout my Ph.D. journey, from beginning to the end. I am thankful to Birgit King for assisting me with the Ausländerbehörde. With their support, I could successfully navigate through the complicated administrative process in Germany.

I am grateful to Achim Güth, Ulrike Waizmann, and Bernhard Fenk in Nanostructuring Lab for preparation of patterned electrode and FIB-SEM measurements. Many thanks to Dr. Kathrin Küster for the XPS measurements, Samir Hammoud for the ICP-OES measurements.

I am indebted to all the members of our department for their generous assistance,

both in the lab and in everyday life. Their willingness to share their knowledge, collaborate, and provide a helping hand has greatly enriched my research experience. I would like to express my gratitude to Florian Kaiser for the design and creation of the measurement cells, as well as providing comprehensive technical support in the lab. I am thankful to Udo Klock for providing assistance with the chiller machine during my first and second years of Ph.D. Also my thanks go to Annette Fuchs for support with SEM and EDX measurements, Dr. Helga Hoier and Armin Sorg for their contributions to XRD measurements, Uwe Traub for assistance with IT matters. Also, many thanks to Dr. Rotraut Merkle for providing valuable scientific support. Many thanks to Dr. Jelena Popovic-Neuber for assisting me in learning zeta potential measurements. Thanks to Dr. Klaus-Dieter Kreuer for having in many interesting discussions on various topics.

I would like to express gratitude to Ya-ru Wang, a member of the halide perovskite team, for her invaluable contributions to scientific discussions and her support. Additionally, I extend my thanks to Chuanlian Xiao for the valuable discussion we had while writing my thesis, to Dr. Giulia Raimondi for the teaching me in response to my naive questions, and to Dr. Kyungmi Lim for engaging discussions on various topics in both scientific and life aspects. Many thanks to the former members of department for their advice and useful discussions during my Ph.D.; Dr. Christian Berger, Dr. Eugene Kotomin, Dr. Yuanye Huang, Dr. Markus Joos, Dr. Gee Yeong Kim, Dr. Chuanhai Gan, Dr. Andreas Muenchinger, Dr. Torben Saatkamp, Dr. Maximilian Hoedl.

I would like to extend my appreciation to my friend Karla Vanessa Cordero Solano at the institute for her invaluable assistance with late-night feedback sessions, food support including delicious Costa Rican cakes and and offering emotional support. Additionally, I want to express my gratitude to my friend Seol Jin Baek in South Korea for the consistent emotional support throughout my PhD. journey. Her consistent support, which began when I decided to study science, is truly priceless. I am genuinely grateful for these friendships.

I want to express my profound gratitude to Tim Priessnitz for providing emotional support during my Ph.D. journey. His support has truly enriched my life in Germany. Furthermore, I appreciate his reliability as trustworthy belayer during our climbing sessions. I am looking forward to doing challenging bouldering training and going on climbing trips together.

Lastly, I would like to convey my deepest gratitude to my family, especially my parents, for their unchanging belief in me and their constant support. Their encouragement has kept my spirits high and motivated me throughout this challenging process, serving as the driving force for my achievements. I would also like to extend my thanks to my sister, brother, and their lovely families to sending me cheering and love from South Korea. I eagerly look forward to our family meetup soon.

In conclusion, I am profoundly grateful to all the individuals mentioned above and many others who have supported me in various ways throughout my Ph.D. journey. Without their guidance, assistance, and encouragement, this thesis would not have been possible.

Appendix

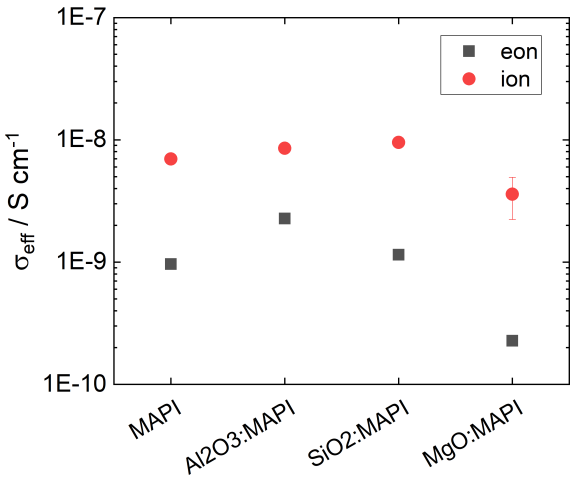

Figure 1: Results of electronic and ionic conductivity measurements of MAPI, Al_2O_3:MAPI, SiO_2:MAPI and MgO:MAPI films. The composite films here are fabricated with 0.3 vol% nominal concentration of oxides.

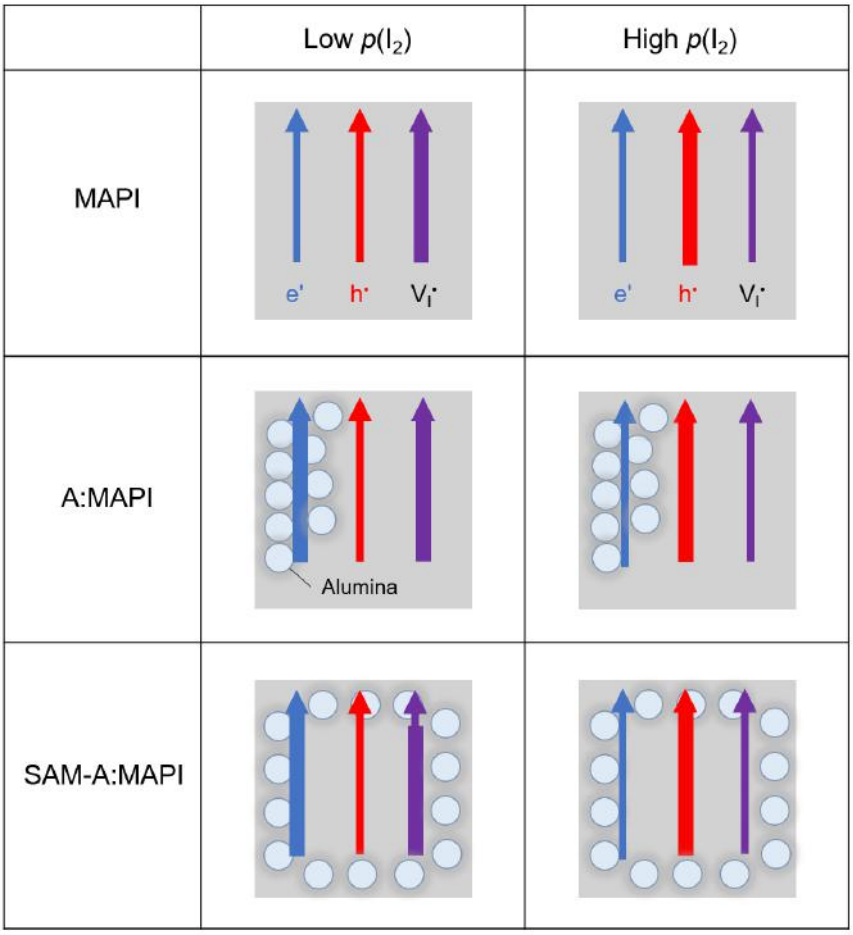

Figure 2: Proposed morphology effects on conductivity of mobile charge carriers in MAPI, A:MAPI, SAM surface modified A:MAPI.

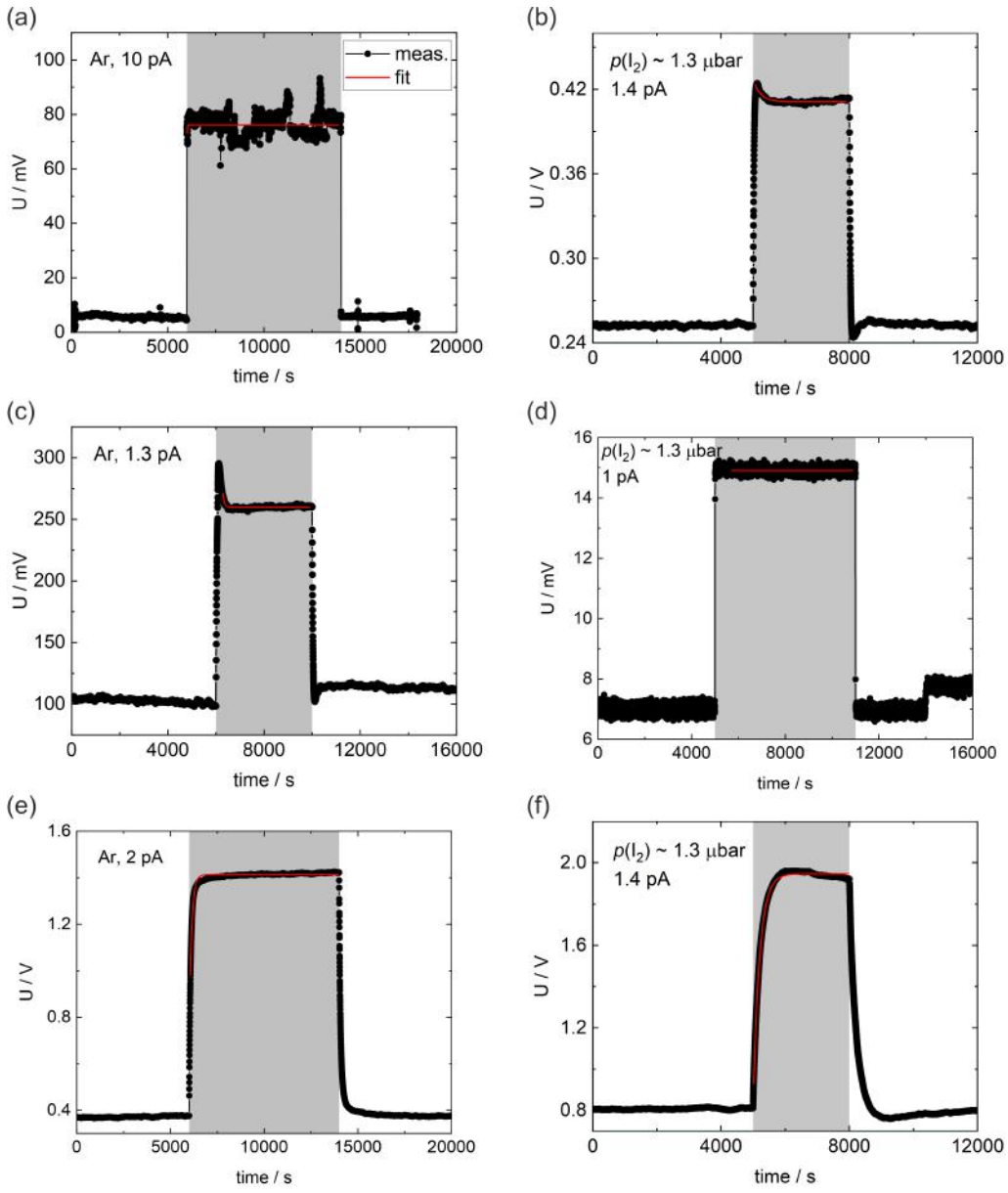

Figure 3: DC polarization measurement results of $mTiO_2$ (a,b), $mTiO_2$ with MeO-2PACz (c,d), and BPA (e,f) surface modifications under Ar and $p(I_2) = 1.3$ μbar. Measurements were taken in the dark at 40 °C, with the respective current displayed in each panel.

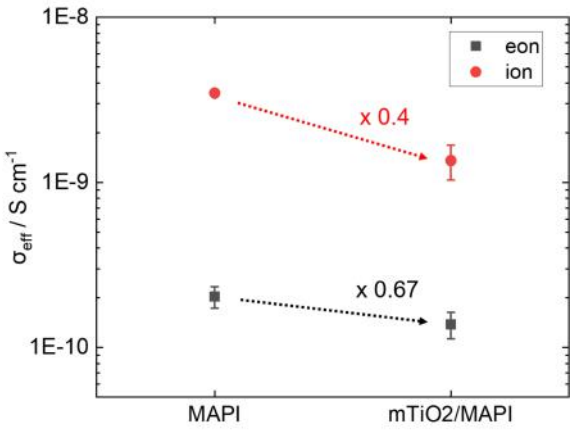

Figure 4: Electronic and ionic conductivities in MAPI and mTiO$_2$/MAPI films analyzed by DC polarization and using the high frequency response of the AC impedance measurement to evaluate the ionic conductivity. The changes in conductivities between the two samples approximately match the porosity of the mesoporous films.

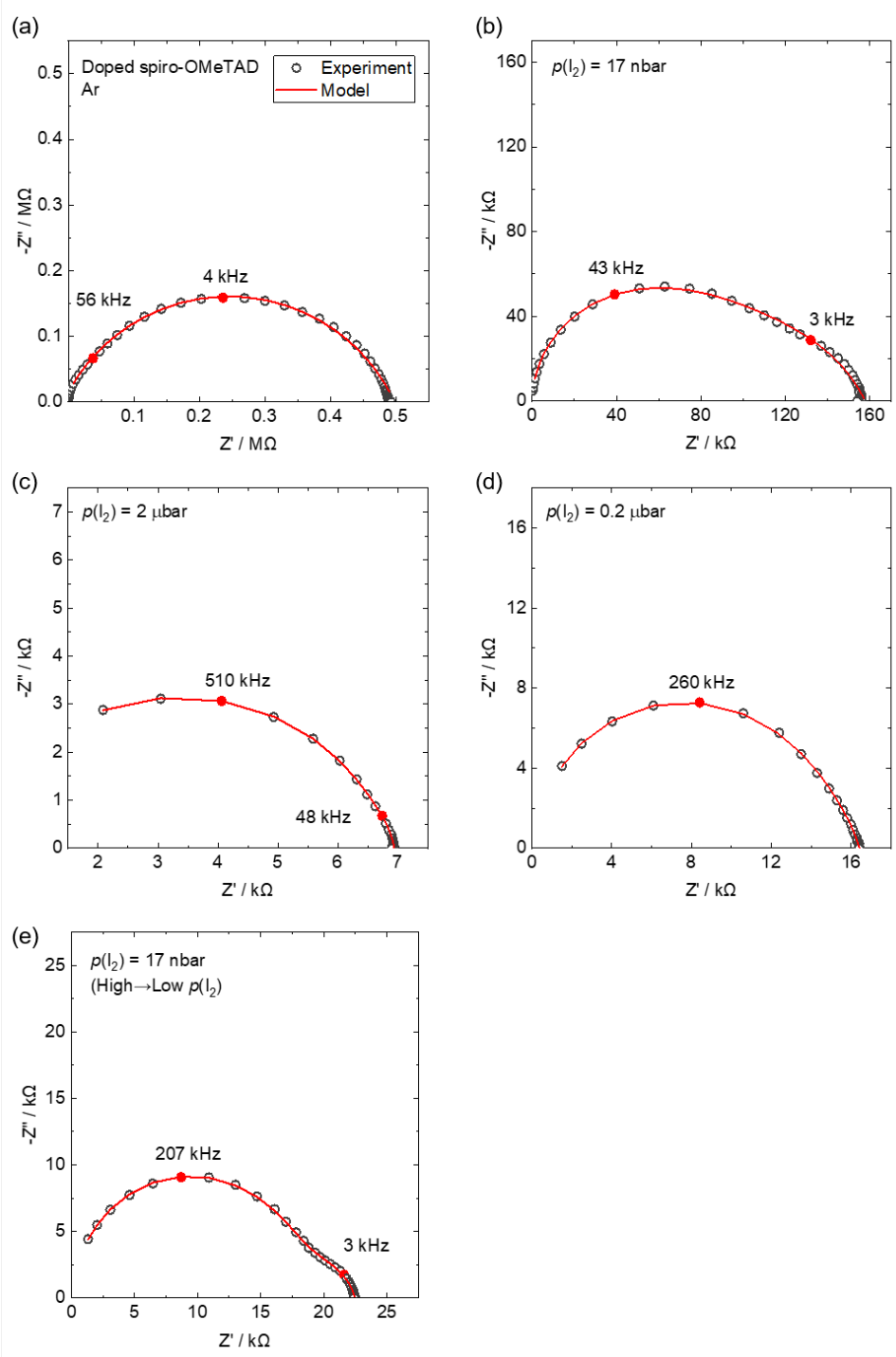

Figure 5: The AC impedance measurements of a doped spiro-OMeTAD horizontal device in different $p(\mathrm{I_2})$.

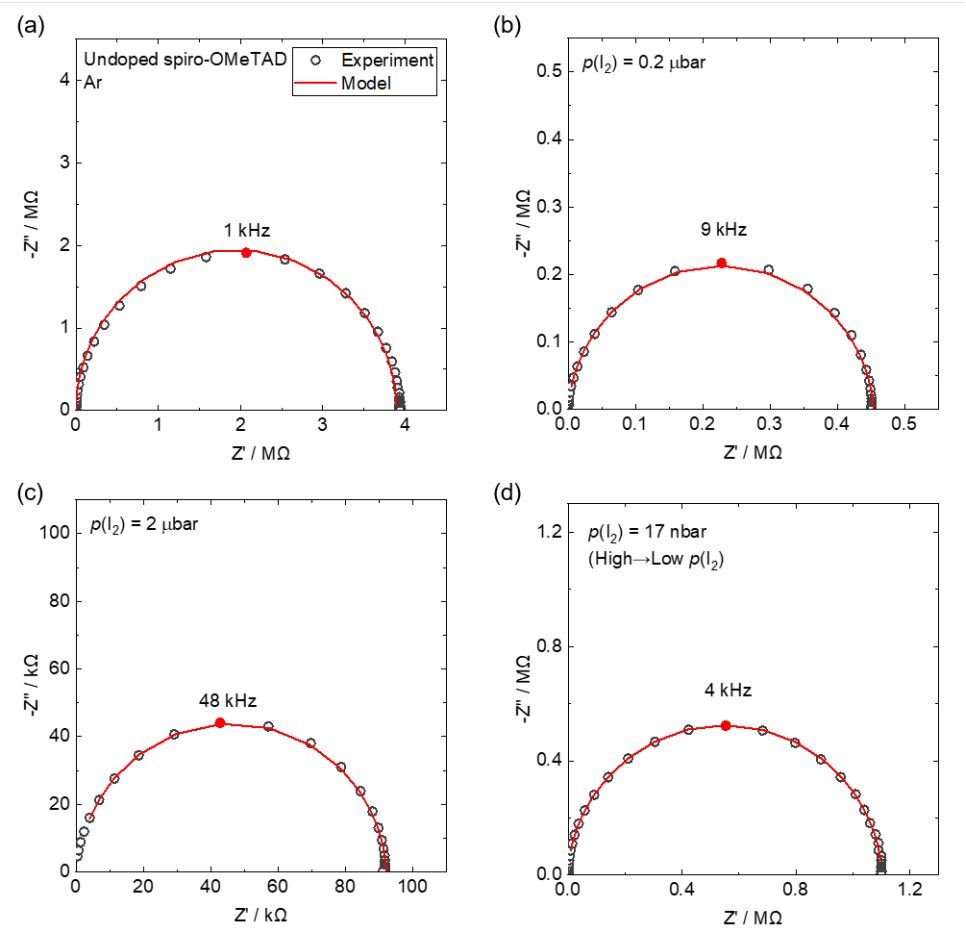

Figure 6: The AC impedance measurement of an undoped spiro-OMeTAD horizontal device in different $p(\mathrm{I_2})$.

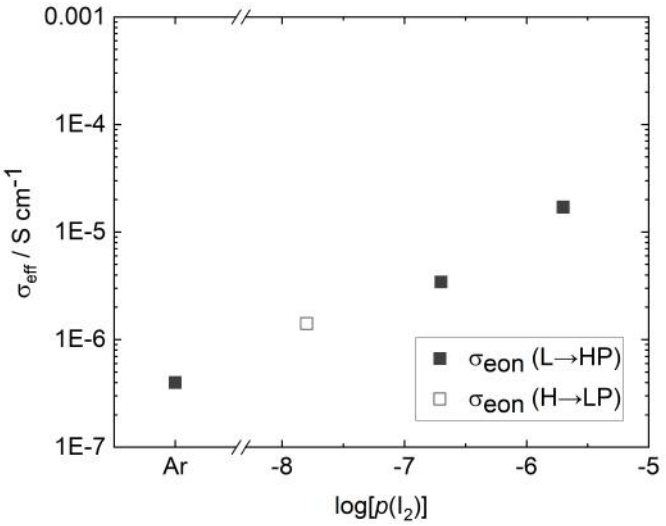

Figure 7: The electronic conductivity of undoped Spiro-OMeTAD in Ar and at different $p(I_2)$. The conductivity is increased by increasing iodine partial pressure.

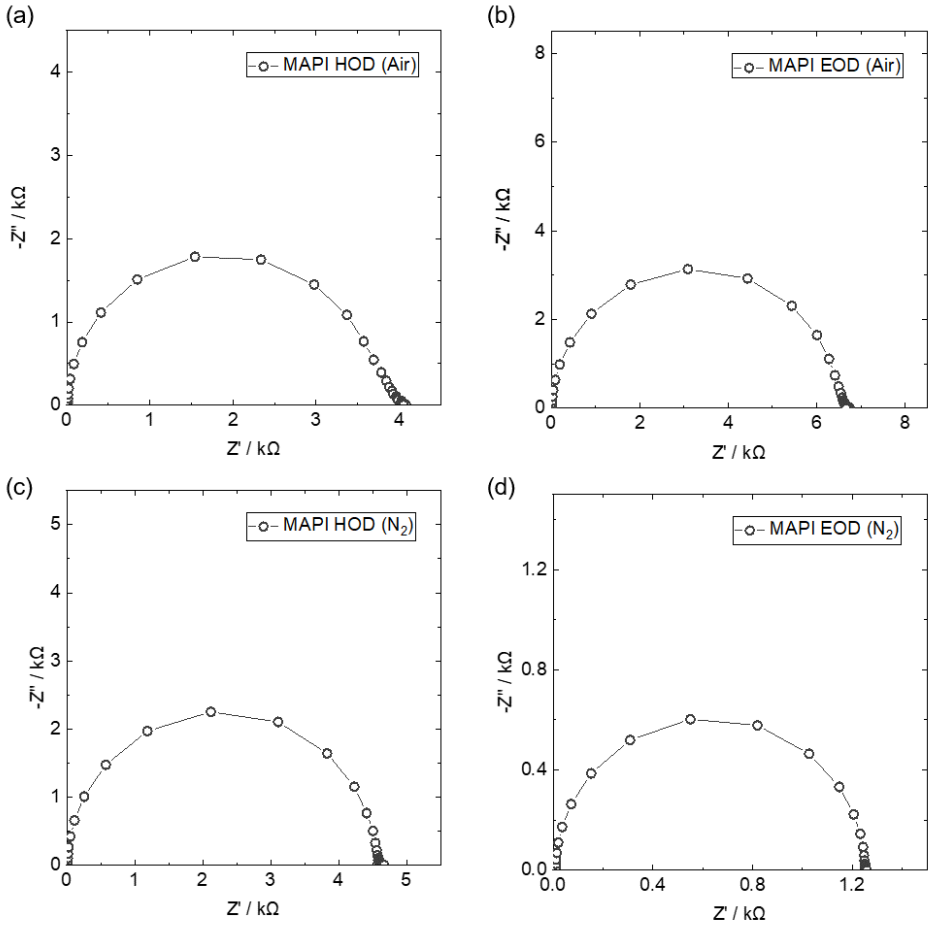

Figure 8: The AC impedance measurements of HOD and EOD fabricated in air and nitrogen.

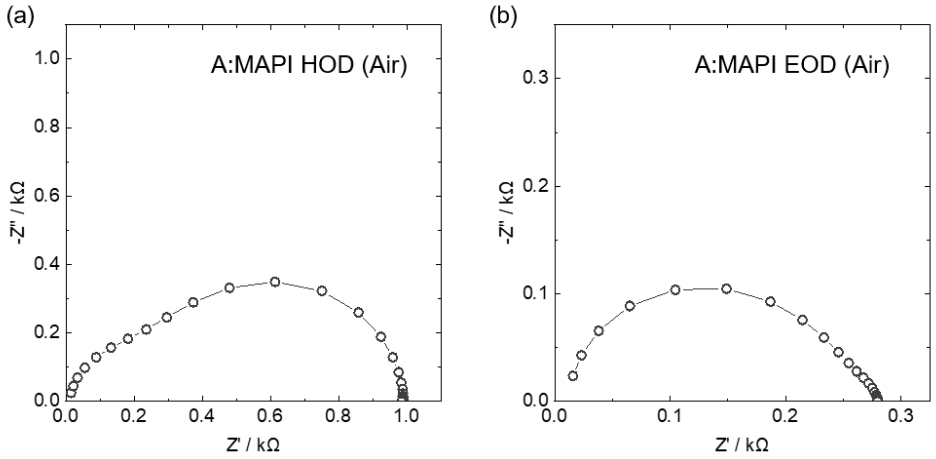

Figure 9: The AC impedance measurement of HOD and EOD consisting of A:MAPI composite active layer fabricated in air.